NASA TECHNICAL
MEMORANDUM

NASA TM X-72542

BALLISTIC INTERCEPT MISSIONS TO COMET ENCKE

FINAL REPORT OF THE
COMET ENCKE BALLISTIC MISSION ENGINEERING PANEL

March 1975
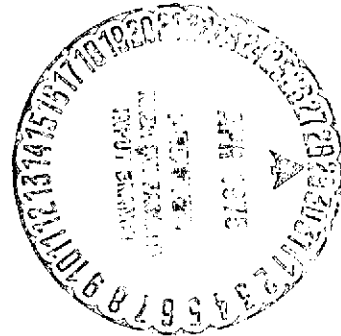
NATIONAL AERONAUTICS AND SPACE ADMINISTRATION

BALLISTIC INTERCEPT MISSIONS TO COMET ENCKE

FINAL REPORT

OF THE

COMET ENCKE BALLISTIC MISSION ENGINEERING PANEL

Members:

D. Herman, NASA/HQ - Chairman

Dr. M. Mumma, GSFC - Co-chairman

J. Beckman, NASA/HQ - Secretary

Dr. R. Farquhar, GSFC

Dr. L. Friedman, JPL

R. Jackson, ARC

J. Moore, JPL

B. Swenson, ARC

Technical Support:

D. Muhonen, GSFC

R. Newburne, JPL

T. Thorpe, JPL

D. Yeomans, Computer Sciences Corporation

Compiled and Edited by M. Mumma

CONTENTS

CONTENTS (Continued)

TABLES

BALLISTIC INTERCEPT MISSIONS TO COMET ENCKE

FINAL REPORT
OF THE
COMET ENCKE BALLISTIC MISSION ENGINEERING PANEL

1.0 INTRODUCTION

A ballistic intercept of Comet Encke presents a new and unique challenge in the exploration of the solar system. The planetary orbits (with the exception of Mercury and Pluto) are all within a few degrees of the ecliptic plane and have nearly circular orbits. Comet Encke's orbit on the other hand, is inclined approximately 12° to the ecliptic plane and has an eccentricity of 0.85. Comet activity is a function of the distance between the comet and the sun. These factors present an intriguing challenge to determine the optimum ballistic intercept of a spacecraft with the comet. If optimum intercept is defined as that mission which yields the highest degree of scientific value for the resources expended, then the following factors must be considered in the synthesis of a mission.

Energy requirements to effect an intercept are minimal if the intercept occurs approximately 30 days prior to perihelion. However, encounter velocity is highest for this trajectory. Launch energy requirements increase rapidly as the intercept occurs closer to perihelion. This increase in energy dictates that the launch propulsion requirements increase, or the spacecraft weight and hence the science payload decrease. However, an intercept near perihelion results in the minimum relative velocity between spacecraft and the comet. As the intercept point is varied in heliocentric distance, the spacecraft targeting error also varies. The combination of encounter conditions, targeting error, and comet activity dictate how close the aim point should be to the cometary nucleus. Distance to the nucleus at closest approach, encounter velocity, and cometary activity at intercept are major constraints on the science value of the mission. The relative aspect angle of the spacecraft trajectory varies with heliocentric distance. At perihelion the spacecraft will encounter the comet at approximately 90° phase angle. The phase angle decreases for earlier encounters and approaches 0° for an intercept 17 days prior to perihelion. Spacecraft engineering requirements and restraints are also a function of the intercept point. An intercept near perihelion presents the most severe thermal control requirements to the spacecraft design. Also communications range at intercept is a function of where the intercept occurs. These factors necessarily influence the spacecraft complexity, and hence, cost.

The problem of defining the optimum intercept condition is therefore a difficult one in that all of the parameters must be assessed from the standpoint of maximizing the science value per dollar. This report documents the analysis

conducted by the Encke Ballistic Mission Engineering Panel to arrive at a logical basis for determining the most profitable ballistic mission to Comet Encke.

2.0 BALLISTIC MISSIONS TO ENCKE: MISSION ANALYSIS

Three different intercept missions of Comet Encke are described in this section. Case 1 is for nominal encounter at perihelion which occurs about a day after the descending node at a flyby speed of about 8 km/s, case 2 is for encounter at 16 days before perihelion (P-16) at a flyby speed of 18 km/s, and case 3 is for encounter at P-30 days at a flyby speed of 27 km/s. One advantage of case 3 over cases 1 and 2 is that the launch energy requirement is significantly less. On the other hand, the flyby speed is smallest for the perihelion intercept and the comet is most active there. Finally, the targeting errors are different for each mission. Launch and trajectory characteristics are discussed in Appendix I.

2.1 Mission Descriptions

The short period Comet Encke during its 1980 apparition offers the fortuitous possibility of a short flight time mission with a relatively small flyby speed. This happens because the Earth crosses the ascending node of the orbit of Encke at such a time that near 180°, a Hohmann type transfer trajectory will yield a flyby near the perihelion. The time interval between Earth's crossing the node on about August 28, 1980 and the perihelion of Encke at 0.34 AU on December 7, 1980 is 101 days.

Figure 1 is an ecliptic plane projection of the orbit of Encke with the position of the Earth indicated at the times of the perihelia in August 1977, December 1980 and March 1984. A bipolar plot is also shown to illustrate the relative positions of the Earth and the comet (Fig. 2). (A bipolar plot is one in which the sun-earth line remains fixed at a given apparition and thus the motion of the comet with respect to the earth is easily seen.) The relative positions of Sun, Earth and Comet can be displayed for any apparition by locating the Earth at the moment of perihelion with respect to the vernal equinox. Positions of the Earth at the perihelia of 1977, 1980, and 1984 are shown. (The vernal equinox direction indicated is valid only at the time of perihelion.) Table I contains the orbital elements for the comet in 1980 (Marsden and Sekanina, (Astron, J. March 1974)).

Figure 3 shows the relative motion of the spacecraft with respect to the comet near encounter on each of the three mission trajectories. Each curve is drawn projected in the plane determined by Sun-comet line at encounter and the relative velocity vector at encounter. The spacings of tick marks at one day intervals along each curve indicate the difference in flyby speeds for the three cases. The
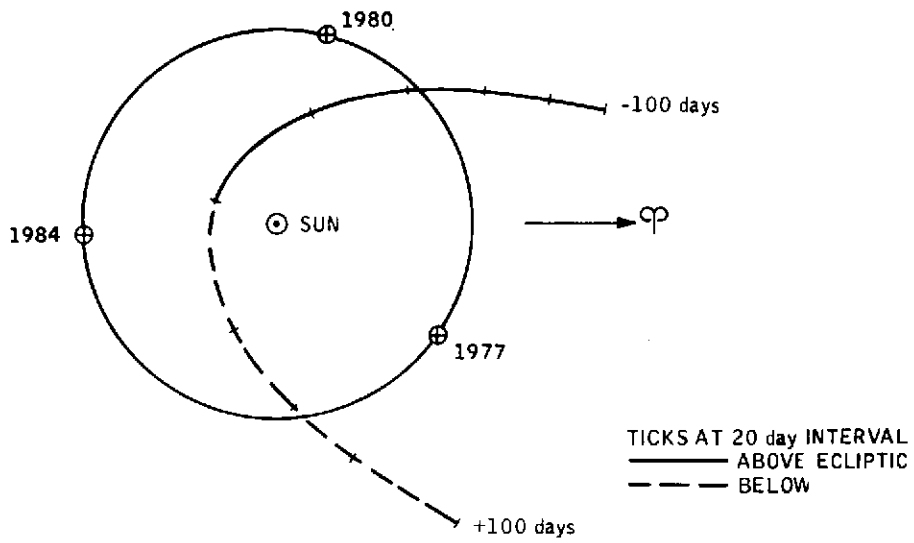
Figure 1. Comet Encke Orbit Plot (Ecliptic Plane Projection)
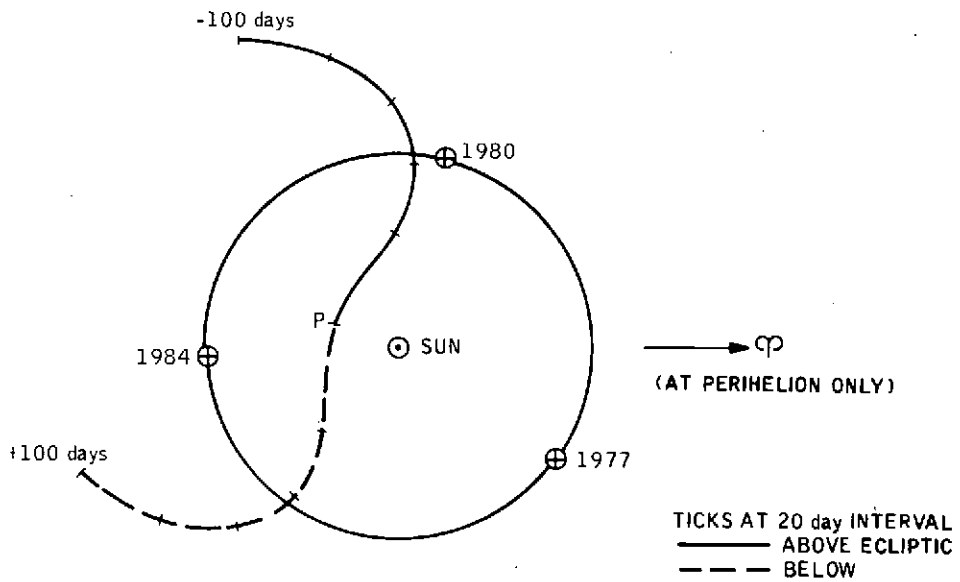
Figure 2. Comet Encke Bipolar Plot With Earth for 1977, 1980 and 1984 Apparitions (Ecliptic Plane Projection)

3
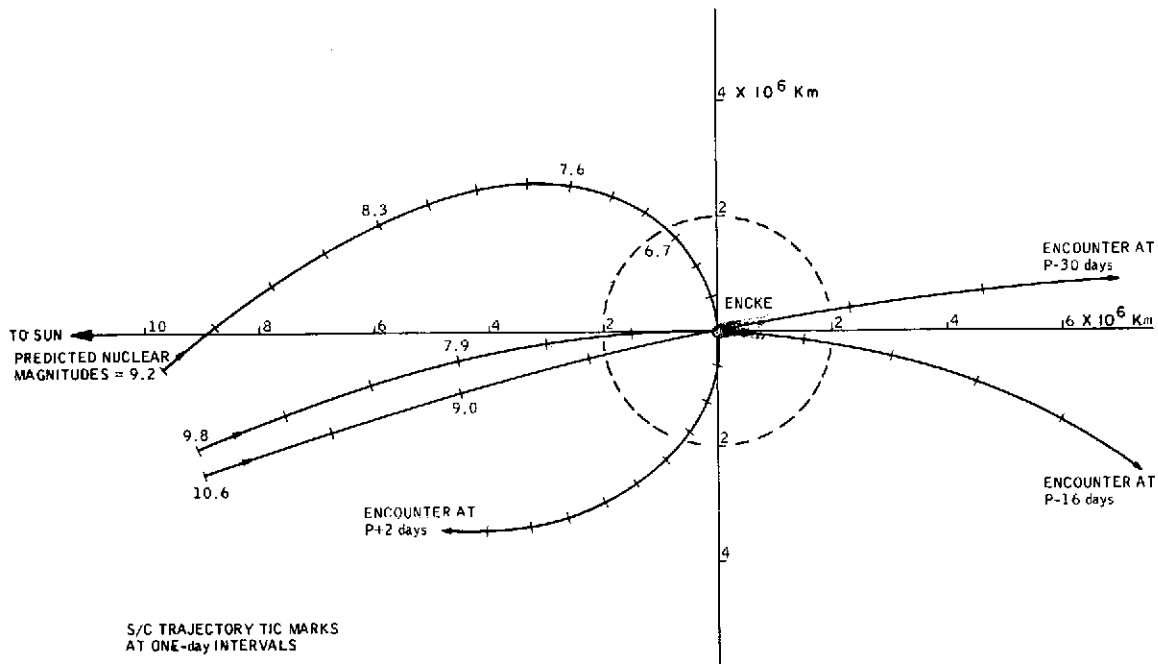
Figure 3. Comet Encke Encounter Geometry (1980)

Table I

Orbital Elements for P/Encke

q = 0.339941 AU	T_p = Dec. 6.5470 1980
e = 0.846470	Period = 3.295 yr. = 1203.4 days
i = 11.9460	Aphelion Distance = 4.0884 AU
Ω = 334.1978	Speed at q = 69.416 km/s
ω = 185.9792	a = 2.214167 AU

estimated nuclear magnitude is indicated at several points. It is based on the standard inverse square law (for objects shining by reflected light), an absolute magnitude of 16.0 and a phase increase of 0.03 mag/deg. (See Section 3.1.)

Finally Table II contains mission and trajectory data for each mission including the range of values corresponding to a 10 day launch period and a 4 or 5 day arrival period (except for case 1 where a single arrival date is chosen in order to achieve the lowest possible flyby speed, see Appendix I).

4

Table II

Encke 1980 Mission Data

Case 1: Perihelion Encounter
Launch Vehicle Titan-3E/Centaur/TE 364-3

	Range	Nominal
Launch Date	August 20-29	August 25
Arrival Date	December 8	December 8 (P+2)
Launch C_3 (km^2/s^2)	90-104	94
Payload System Weight (kg)	1059-823	977
Sun-Comet Distance (at Encounter, AU)	0.34	0.34
Earth-Comet Distance (at Encounter, AU)	1.08	1.08
Phase Angle (Degrees)	83-90	87
Thermal Load (at Encounter, Solar Constants)	8.7	8.7
Flyby Speed (km/sec)	7.1-8.2	7.3

Case 2: 0.53 AU Encounter
Launch Vehicles (i) Atlas/Centaur/TE 364-4
(ii) Titan-3E/Centaur

	Range	Nominal
Launch Date	August 24-Sept. 3	August 28
Arrival Date	Nov. 29 – Nov. 24	November 22 (P-16)
Launch C_3 (km^2/s^2)	66-80	72
Payload System Weight (kg) (i)	363-282	327
(ii)	1550-1150	1400
Sun-Comet Distance (at Encounter, AU)	0.42-0.56	0.53
Earth-Comet Distance (at Encounter, AU)	0.53-0.72	0.58
Phase Angle (Degrees)	0.5-8	0.5

Table II (Continued)

Case 2: (Continued)		
	Range	Nominal
Thermal Load (Solar Constants)		
At Encounter	3.2-5.7	3.6
At Perihelion of S/C Trajectory	4.3-6.2	5.0
Flyby Speed (km/sec)	15-19	18

Case 3: 0.80 AU Encounter
Launch Vehicle Atlas/Centaur/TE 364-4

	Range	Nominal
Launch Date	July 31-Aug. 10	August 8
Arrival Date	Nov. 4-Nov. 8	November 6 (P-30)
Launch C_3 (km^2/s^2)	41-46	43
Payload System Weight (kg)	580-534	569
Sun-Comet Distance (at Encounter, AU)	0.76-0.82	0.80
Earth-Comet Distance (at Encounter, AU)	0.30-0.37	0.34
Phase Angle (Degrees)	12-14	12
Thermal Loads (Solar Constants) At Encounter	1.4-1.8	1.6
At Perihelion of S/C Trajectory	1.4-2.4	1.9
Flyby Speed (km/sec)	25-27	27

2.2 Navigation

2.2.1 A-Priori Position Errors for the 1980 Apparition of Comet Encke

The position errors derived in this section are those which result from uncertainties in the position of Comet Encke using groundbased observations only. For the present covariance error analysis, the 5 returns to perihelion (1967-1980) are represented by forty actual observations from August 2, 1967 through October 24, 1973 and by 28 additional, postulated observations from October 24,

1973 through November 16, 1980. One observation was processed at each of the 1978 and 1979 opposition dates and the 1980 recovery of the comet was assumed to occur on July 9. The postulated observation schedule was determined after considering the relative-sun-earth-comet geometries, the available hours of dark observing time as well as the apparent nuclear and total magnitudes for various dates.

The present error analysis of comet Encke assumes a 1-σ measurement error of 3 arc seconds for both the right ascension and declination. This value is primarily due to the deviations of the comet's center of mass from the observed center of light. The 3 arc second value is consistent with the mean residuals obtained for various orbit determinations for past apparitions of comet Encke. This value is somewhat higher than for most other short period comets due to comet Encke's relatively high nuclear activity.

The error analysis was initialized in 1967 by a state vector and appropriate values for the nongravitational parameters. The initial 8 x 8 covariance matrix was essentially infinite. Each set of observations was batch processed and the updated covariance was propagated forward in time via the state transition matrix. All planetary perturbations were taken into account. The time history of the comet's error ellipsoid is presented in Table III. The first two columns of this table represent the calendar date and the number of days to perihelion. The next twelve columns represent the 1σ position errors (km) for the radial Sun-comet direction ($\hat{r}$), the direction normal to the comet's orbital plane ($\hat{n}$), and the transverse direction defined by the cross product of the first two unit vectors ($\hat{T} = \hat{n} \times \hat{r}$). The columns headed by Δ, R and θ represent the Earth-comet distance in AU, the Sun-comet distance in AU and the Sun-Earth-Comet angle in degrees. The a-priori errors represent the forward propagation of the covariance matrix obtained by processing all observations from 1967-1979. The three columns listed under cases 1, 2 and 3 reflect the effect of each 1980 observation on the comet's error ellipsoid. Horizontal lines are drawn under the last ground based observation in each of the three cases. For example, for case 1, the final ground based observation on November 16 reduces the σ_r, σ_n and σ_T components to 416, 249 and 359 km. In the absence of further observations, σ_T grows to 897 km and σ_r shrinks to 143 km at the December 8th intercept. This behavior is due primarily to the dynamic evolution of the error ellipsoid in the absence of observations. From the table, it is apparent that, for case 1, the cometary position errors (σ_r, σ_n, σ_T) at intercept are 143, 249 and 897 km. For case 2 the respective values are 422, 240 and 450 km, and for case 3, the final position errors at intercept are 422, 295 and 282 km.

2.2.2 On-Board Optical Navigation

The use of on-board optical measurements of Encke's nucleus is being considered to reduce the a-priori ephemeris errors (Sec. 2.2.1), and consequently

Table III

A-Priori Position Errors for Comet Encke (1980)

Date 1980	T_p	A-Priori*			1980 Observations Processed**									(AU)		(DEG)
					Case 1 Intercept Dec. 8			Case 2 Intercept Nov. 21			Case 3 Intercept Nov. 6					
		σ_r	σ_n	σ_T	σ_r	σ_n	σ_T	σ_r	σ_n	σ_T	σ_r	σ_n	σ_T	Δ	R	θ
July 9	-150	4168	2130	3239	3352	1926	2471	3352	1926	2471	3352	1926	2471	2.43	2.33	72
19	-140	4338	2084	3275	2917	1739	2012	2917	1737	2012	2917	1737	2012	2.21	2.23	78
29	-130	4521	2036	3327	2572	1567	1683	2572	1567	1683	2572	1567	1683	1.98	2.13	84
Aug. 8	-120	4718	1985	3399	2271	1406	1426	2271	1406	1426	2271	1406	1426	1.76	2.03	90
18	-110	4933	1936	3494	1992	1249	1213	1992	1249	1213	1992	1249	1213	1.53	1.92	96
28	-100	5169	1894	3617	1644	1146	1026	1644	1146	1026	1644	1146	1026	1.31	1.81	101
Sept. 7	-90	5429	1876	3769	1469	945	836	1469	945	836	1469	945	836	1.10	1.69	107
17	-80	5717	1921	2952	1217	799	710	1217	799	710	1217	799	710	0.89	1.56	111
27	-70	6040	2117	4146	968	658	564	968	658	564	968	658	564	0.69	1.43	114
Oct. 7	-60	6403	2604	4301	724	524	427	724	524	427	724	524	427	0.51	1.28	112
17	-50	6811	3480	4347	504	400	313	504	400	313	504	400	313	0.36	1.13	103
27	-40	7258	4612	4407	387	308	264	387	308	264	387	308	264	0.28	0.97	77
Nov. 6	-30	7699	5595	5229	391	269	273	391	269	273	422	295	282	0.32	0.80	45
16	-20	7893	5683	8023	416	249	359	416	249	359				0.47	0.62	29

∞

Table III (Continued)

Date 1980	T_p	A-Priori*			1980 Observations Processed**									(AU)		(DEG)
					Case 1 Intercept Dec. 8			Case 2 Intercept Nov. 21			Case 3 Intercept Nov. 6					
		σ_r	σ_n	σ_T	σ_r	σ_n	σ_T	σ_r	σ_n	σ_T	σ_r	σ_n	σ_T	Δ	R	θ
Nov. 21	-15	7617	5181	10263	422	240	450	422	240	450				0.58	0.52	25
26	-10	6628	4481	12910	401	234	579							0.70	0.44	23
Dec. 6	0	399	3477	16833	171	243	874							1.00	0.23	20
8	+2	1871	3411	16611	143	249	897							1.06	0.34	19

*A priori, one-sigma errors (Km) in the radial, normal and transverse directions. Last observation processes was during 1979 opposition.

**Evolution of one-sigma errors (Km) if one ground based observation is processed at 10 day intervals beginning July 9. Measurement noise = 3 arc seconds.

For cases 1, 2 and 3, the tabular entries just above the horizontal line represent the position errors after the last ground based observation.

to enable improved targeting accuracy. The key to such measurements is locating the nucleus relative to an inertial frame, i.e., a star background. The requirements which an on-board system must satisfy are:

  a. detection of the nucleus,

  b. detection of sufficient comparison stars,

  c. determination of their positions with sufficient cross track accuracy to improve the ephemerides.

On-board navigation (OBN) should not be confused with the imaging experiment, which also features optical detection of the nucleus. OBN requires an attitude stabilized camera whereas the imaging experiment could be accomplished with either spin-scan or attitude-stabilized cameras. A de-spun platform (such as on OSO) would be required for OBN on a spin-stabilized spacecraft. In either case, spacecraft pointing errors could impose special limitations on the maximum exposure time. Since all OBN must be done from an attitude stabilized platform, we have used the parameters of vidicon cameras already flown on Mariner spacecraft to assess the possibility of OBN. Other optical sensors may be possible (Sec.6.0).

The threshold magnitude at which Encke's nucleus can be detected by state-of-the-art imaging systems has been a somewhat controversial question since it requires a detailed appraisal of the technical level of performance of flight-proven cameras. A detailed study has been conducted at JPL and shows that a 10th magnitude detection threshold may be feasible using Mariner-type vidicons. The actual thresholds were arrived at in the following way:

The Mariner telescope (500 mm f.1.) was assumed to have enhanced UV transmission due to a change in coatings and filters. The MVM electronic noise characteristics were used. The comet nucleus was assumed to be detected when the signal to RMS noise was 10. The maximum exposure times used were 6 seconds for the 500 mm telescope (Mariner 9) and 18 seconds for the 1500 mm focal length telescope (Mariner 10). Exposure time as a function of magnitude is shown in Figure 4. This requires a drift rate of 5μ rad/sec. for 1 pixel smear. Results for two albedos were considered (20% and 5%) and a 4 Km nucleus was assumed in Table IV. These values generally reflect 10th magnitude detection with 500 mm telescope at $pr^2 = 0.8$ and about 9th magnitude with $pr^2 = 0.2$. Use of the 1500 mm telescope causes detection to be delayed by 1-2 magnitudes. First detection times for a 2 Km nucleus are given in Appendix IV. The time of detection before intercept is strongly dependent on the assumed threshold magnitude for first detection.
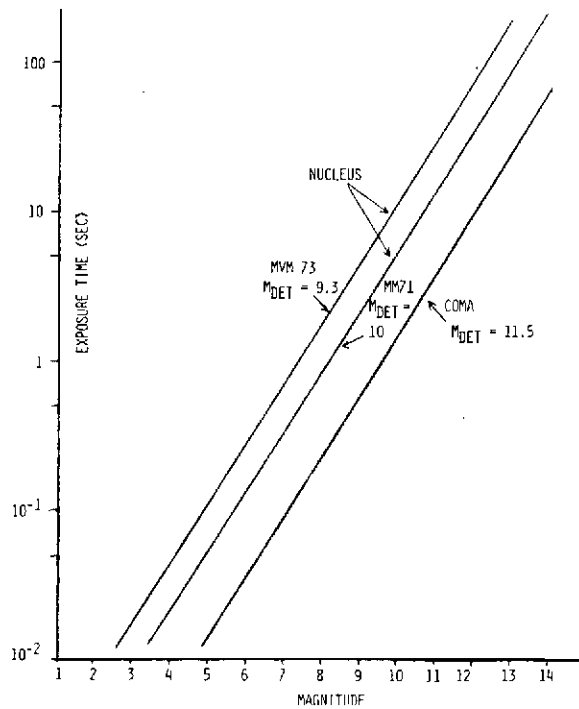
Figure 4. Exposure Time vs. Magnitude

Table IV

Time of Detection of Encke's Nucleus in Days Before Encounter

	pr^2	500 mm Telescope	1500 mm Telescope
		(a) (b)	(a) (b)
Mission 1	0.8	25 ±5	12 ±2
Perihelion Encounter	0.2	17 ±4	7 ±2
Mission 2	0.8	12 ±2	6.5 ±2
≈0.54 AU Encounter	0.2	8.5 ±1.5	4 ±1
Mission 3	0.8	7.5 ±1.5	4 ±1
≈0.8 AU Encounter	0.2	4.5 ±1.5	2 ±1

(a) 10th magnitude detection threshold.
(b)   9th magnitude detection threshold.

For the purpose of determining the improvement in a-priori ephemeris errors a 9th magnitude detection of the nucleus was assumed (Sec. 2.2.3). These results are all based on analysis and modelling since demonstration of such detection has not been possible. Thus, we can say the probability of detecting Encke's nucleus as a function of nuclear magnitude is less than unity. Such probability must be factored into the prediction of error estimates for the mission's navigation. When this is done it is found that it alters significantly the notion of one to three sigma error ellipses, tending to lower the probability of successful targeting to very small circles around the nucleus. This will be considered below in the discussion of targeting errors.

Star background plots for the three missions being considered are shown in Figures 5 through 7. Mission 2 has an abundance of adequate stars; mission 1 appears to have an adequate number of stars and mission 3 appears to have insufficient stars. The geometry will change slightly during the approach. Stars up through 9th magnitude were considered.

Accuracy turns out not to be an important parameter (over a limited range) in that the key requirement is detection. As long as several on-board measurements can be obtained, improvement in position determination will result. We have assumed 30 μ rad as the one-sigma measurement accuracy consistent with Mariner 9 and Mariner 10 experience. If it is twice as bad, then acceptable performance – as reported in the next section – will still result.
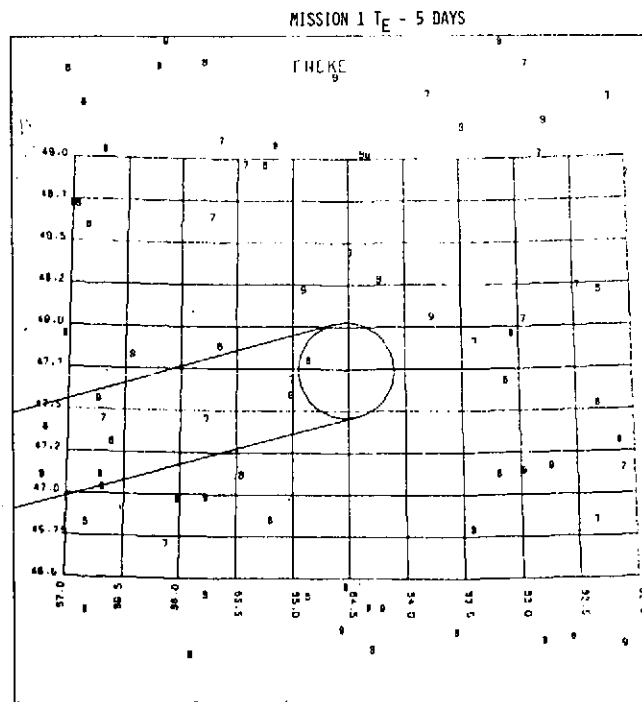
Figure 5.   Background Stars at Perihelion

12
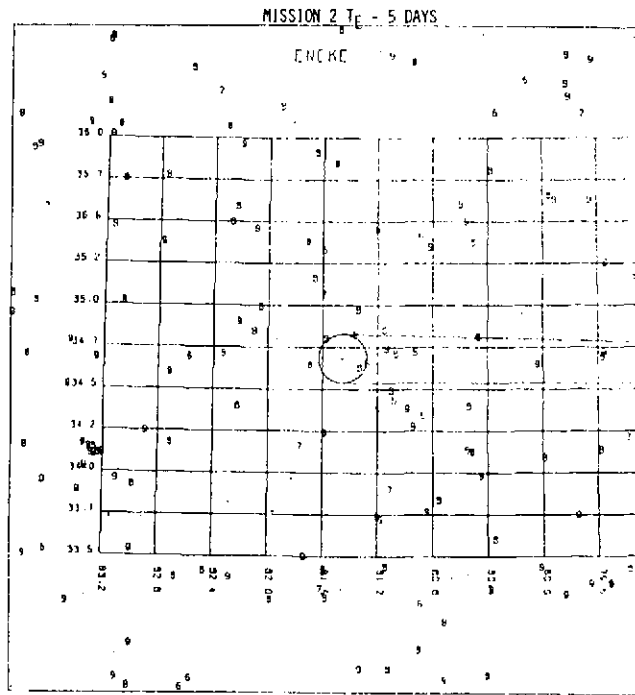
Figure 6. Background Stars at P-16
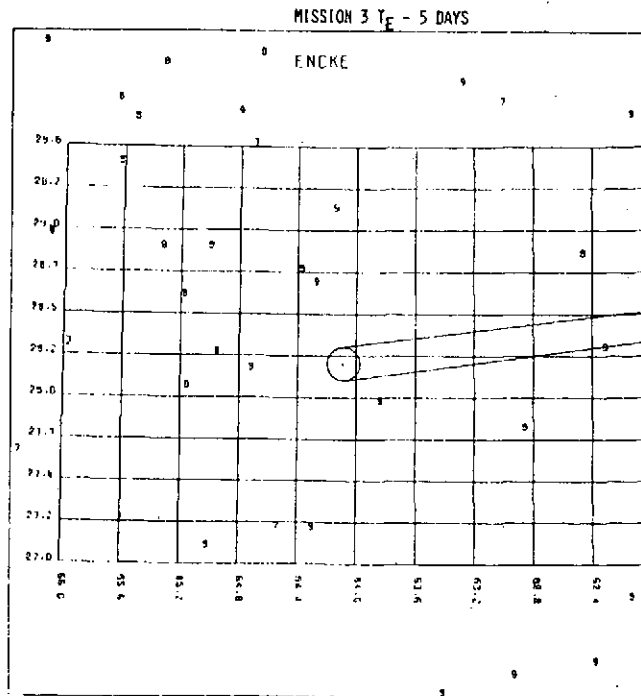
Figure 7. Background Stars at P-30

13

2.2.3 Targeting Errors

The targeting errors described in this section are derived from the a-priori cometary position errors (Sec. 2.2.1) and the reduction in these errors which results from on-board navigation (Sec. 2.2.2) and earth-based video tracking of the spacecraft. The approach geometries relative to the sun-comet line for each of the three model intercepts are shown in Figure 3. The number of position measurements obtained with the on-board imaging system is determined by taking measurements at 6 hour intervals, starting when the nucleus reaches 9th magnitude as seen by the spacecraft, and stopping when the distance to the nucleus reaches 2×10^6 km or at one day prior to encounter, whichever occurs sooner. The 9th magnitude limit was discussed in the previous section and it is assumed that continuous undisturbed measurements are desirable within 2×10^6 Km of the nucleus to ensure detection of a bow shock, and that system engineering response times require completion of navigation activities at least one day prior to intercept.

Targeting errors are represented by 3σ ellipses in the "impact plane," which is normal to the spacecraft velocity vector relative to the comet at encounter. (The closest approach relative position vector always lies in this plane.) Figure 8 shows the "$\hat{T}$-$\hat{R}$" coordinate system used. "$\hat{T}$" is defined by the intersection of the impact plane with the ecliptic parallel which passes through the comet at encounter. $\hat{R}$ and the relative velocity vector, $\hat{V}$, complete a right-hand system. The expected 3σ error ellipses for the three encounter dates under consideration are illustrated in Figure 9 with the numerical statistics given in Table V. Both comet and spacecraft errors are reflected in these ellipses, so the comet position can be considered a random variable about the center with the spacecraft a fixed point chosen anywhere in the plane. To minimize miss distance while avoiding passing through an exclusion zone about the nucleus an "aim point" should be selected co-linear with the minor axis of the ellipse.

Although a significant improvement of targeting errors would be possible should on-board navigation be employed, it should be remembered that the feasibility of on-board navigation for comet-intercept missions has not yet been demonstrated. For a conservative appraisal of the potential scientific return from the 1980 Encke flyby, the targeting errors without on-board navigation should be used (see Sec. 4.0).

2.3 Targeting Strategy

The targeting strategy has been developed assuming: (1) that the spacecraft must pass on the sunward side of the nucleus in order to ensure favorable conditions for the imaging experiment; (2) that there may be some exclusion zone (of radius R_{EZ}) within which the particle impact hazard to the spacecraft is unacceptably

$\hat{V}$ = SPACECRAFT VELOCITY RELATIVE TO COMET

$\hat{Z}$ = NORTH ECLIPTIC POLE

$\hat{T}$ = $\hat{V}$ x $\hat{Z}$ = REFERENCE VECTOR IN IMPACT PLANE

$\hat{R}$ = $\hat{V}$ x $\hat{T}$ IN IMPACT PLANE

ϕ = ORIENTATION OF MAJOR AXIS OF ERROR ELLIPSE IN IMPACT PLANE
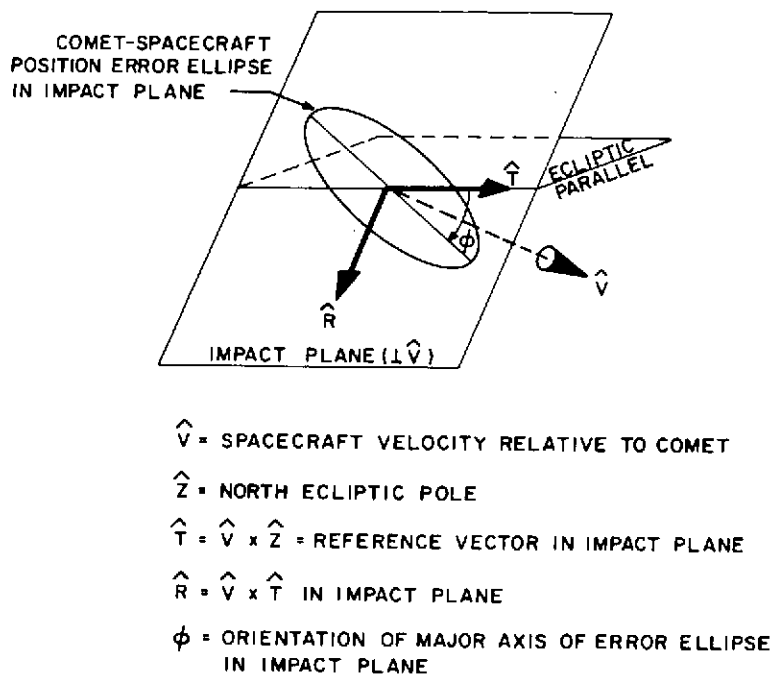
Figure 8.   Impact Plane Coordinate System

WITHOUT ON-BOARD NAVIGATION

WITH ON-BOARD NAVIGATION
(NOTE SCALE CHANGE)
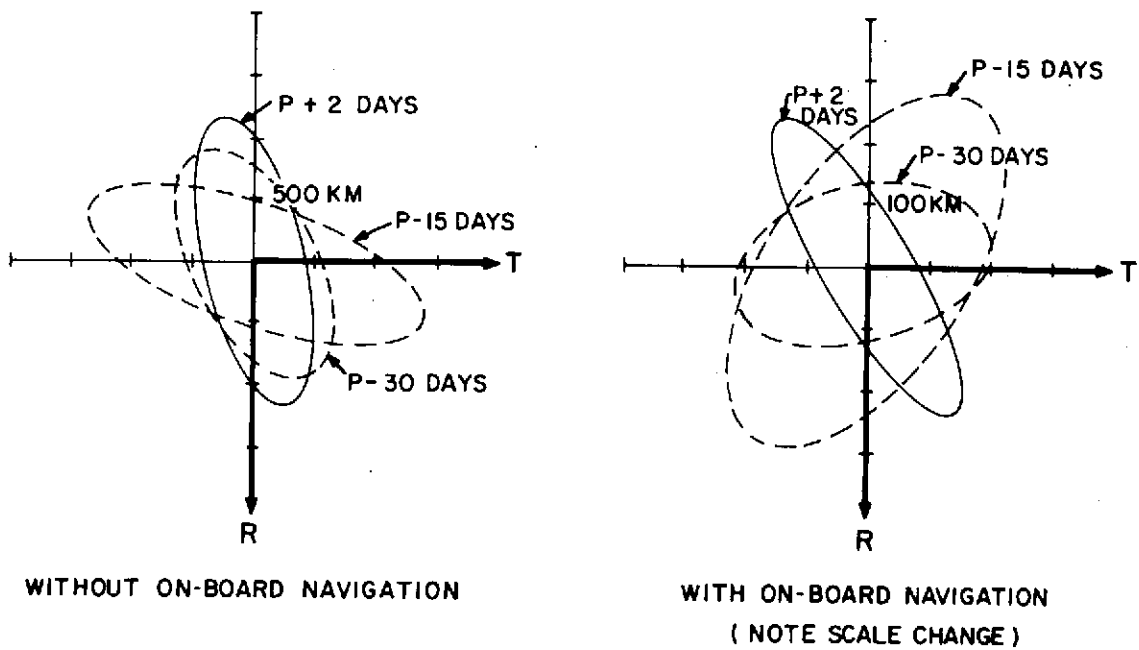
Figure 9.   Targeting Error Ellipses (3σ) in the Impact Plane Showing
Three Encounter Dates

15

Table V

Targeting Errors

Encounter	P + 2 Days		P - 16 Days		P - 30 Days	
On-Board Navigation Error Ellipse (3σ)	Without	With	Without	With	Without	With
Semi-Major Axis (Km)	1141	279	1414	334	1003	208
Semi-Minor Axis (Km)	389	63	509	155	537	112
Orientation-ϕ (Degrees)	73	60	18	123	63	159

On-Board Navigation Assumptions

Measurement Accuracy (1-σ)	6 arc sec
Measurement Schedule	One every 6 hours
First Measurement	Point where Encke's Nucleus $\sim$ 9th Mag.
Last Measurement	S/C-Comet Distance $\sim 2 \times 10^6$ Km

high; and (3) that the median miss distance for each heliocentric intercept point will depend on whether or not on-board navigation can be used to reduce the ephemeris errors.

The first assumption is satisfied a-priori at the P-30 and P-15 intercepts since the spacecraft approaches the comet essentially along the sun-comet line (Fig. 3). It is satisfied at perihelion (where the spacecraft approaches at 60-90° to the sun-comet line) if the spacecraft is targeted 3σ off the nucleus in the sunward direction. The second assumption requires that the spacecraft be targeted at $R_{EZ} = 3\sigma$ in all three intercepts if $R_{EZ} \neq 0$. R_{EZ} can only be determined by a detailed hazard analysis which is beyond the scope of this study; for comparison purposes we have taken ad hoc values: $R_{EZ} = 400$ Km and $R_{EZ} = 0$. The third condition together with the expected scientific return in each case (see Section 4.0) allows an evaluation of the need for on-board navigation.

The three targeting geometries are shown in Figure 10. The probability of flying by the nucleus at a distance between R and R + dR is given by P(R)dR and has been calculated for each of the twelve cases using Monte-Carlo techniques (Section 2.2.3). The median miss distance is listed in Table VI for each case.

CASE A: TARGETING STRATEGY ASSUMING AN EXCLUSION ZONE OF RADIUS R_{EZ}. R_θ 0.34; 0.53; 0.8 AU
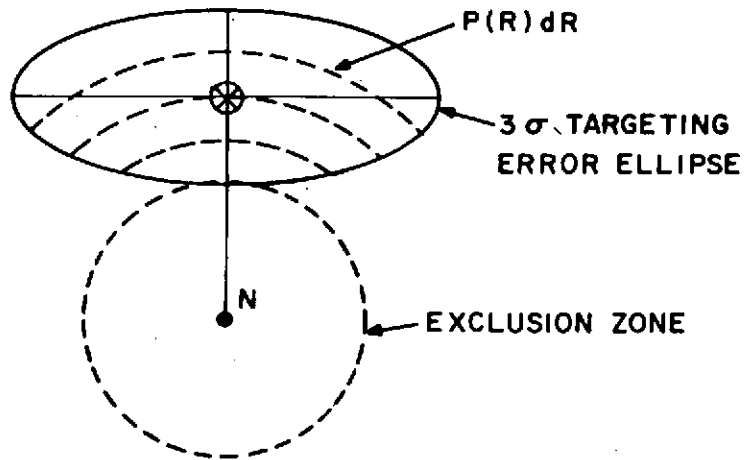
CASE B: TARGETING STRATEGY WHEN APPROACHING FROM SUN ALONG THE SUN-COMET LINE. $R_{EZ} = 0$
$R_\theta = 0.8$; 0.53 AU
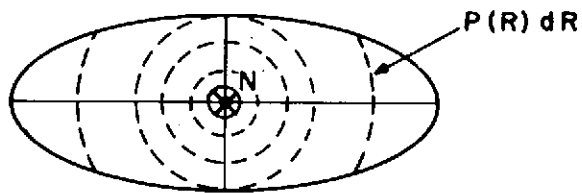
CASE C: TARGETING STRATEGY WHEN APPROACHING AT RIGHT ANGLES TO THE SUN-COMET LINE. $R_{EZ} = 0$
$R_\theta = 0.34$ AU

Figure 10

17
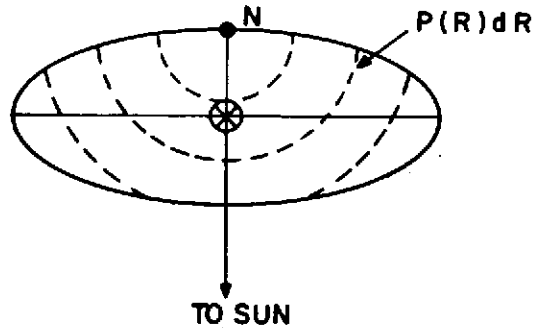
Table VI

Median Miss Distance vs. Intercept Conditions

R(A.U.)	On-Board Navigation	Median Miss Distance (Km)	
		$R_{EZ}=0$	$R_{EZ}=400$ Km
0.34	Yes	95 ⎫ Case A*	471 ⎫
	No	510 ⎭	865
0.53	Yes	98 ⎫	566
	No	403 ⎪	1017 ⎬ Case C
0.80	Yes	62 ⎬ Case B	515 ⎪
	No	302 ⎭	996 ⎭

*Targeting strategy, see Figure 10.

3.0 COMET ACTIVITY MODEL

A model of the physical characteristics and activity of Comet Encke is essential
to enable an estimate of the scientific return for each of the proposed intercept
missions. Fortunately, Comet Encke has been studied fairly intensively over
the past 150 years, consequently a relatively larger body of data exists for it
than for many other short-period comets. Some of these data, such as the trans-
verse nongravitational acceleration - A_2, are relatively straightforward and
error free while others may be influenced by substantial experimental errors,
as is the case with brightness measurements at low elevations and at small ang-
ular distances from the sun. We have tried to incorporate the latest knowledge
of Comet Encke in formulating a baseline model which includes the basic ele-
ments necessary to estimate the science return for the different missions.

The major scientific questions to be investigated on a flyby mission deal with the
nature of the nucleus and the nuclear region (icy halo ?), the identity and abun-
dances of the parent molecules, the nature and size (and spatial) distribution of
the dust, the nature of the solar wind interaction with the comet, and the mech-
anisms leading to destruction and ionization of the cometary gas. The current
state of our technology determines the kinds of on-board instruments that may

be used to study a particular problem. Thus the nucleus may be studied by remote optical scanning (e.g., by a TV-system); the gaseous components by direct sampling (ion and neutral mass spectrometers) and indirect sampling (flourescence radiation in characteristic band systems or atomic lines). The dust component may be studied directly using impact ionization detectors and micrometeoroid impact counters and indirectly by observations of Miescattered sunlight. Magnetic and electric field detectors may be used to determine the ambient fields directly, and electron energy analyzers will yield data on the abundance and energy distribution of free electrons. These data will be necessary for a definitive understanding of the physics of Comet Encke.

The following discussion of the physical activity of Comet Encke is organized so as to correspond to the proposed studies of nucleus, gas, and dust.

3.1 Nucleus

It is generally agreed that the observed non-gravitational effect on the motion of comets is persuasive evidence for the existence of a solid icy nucleus. The non-gravitational effect (N.G.E.) is expressed as a vector acceleration (A) with components resolved along the sun-comet line (A_1), perpendicular to the sun-comet line in the orbit plane (A_2) and mutually perpendicular to the first two directions A_3) (see Fig. 11). The N.G.E. arises when gas evolves asymmetrically from the nucleus. If the nucleus is not spinning only A_1 is non-zero; a spinning nucleus can lead to non-zero instantaneous values for A_1, A_2, A_3 and non-zero time averaged values for $\overline{A}_1$ and $\overline{A}_2$. $\overline{A}_2$ is more easily and accurately determined than $\overline{A}_1$ since it is observed as a change in the time of perihelion on successive returns.

The values of $\overline{A}_2$ for Comet Encke have been derived from orbital data of the past 150 years by Marsden and Sekanina and are shown in Figure 12. $\overline{A}_2$ increased from 1800 to 1825 then decreased by more than a factor of ten to a very small value by 1971. ($\overline{A}_1$ has also been reduced from the orbital data (Yeomans, private communication) but the resulting accuracy is so poor that the formal values are positive as often as negative, which is physically unrealistic.) Sekanina has suggested that the decrease in $\overline{A}_2$ can be explained by a decrease in the gas production rate and that this is consistent with the derived secular decrease on the brightness of the comet over this time. However, $\overline{A}_2$ may decrease in magnitude because of secular decreases in the gas production rate, or precession of the nuclear spin axis toward the orbit plane. $\overline{A}_2$ is now known to have changed sign for two short period comets indicating that their spin axes passed through their respective orbital planes (Fig. 12).

The photometric brightness of Comet Encke does appear to show some secular decrease, although the amount of this decrease is a topic of some dispute (Kresak,
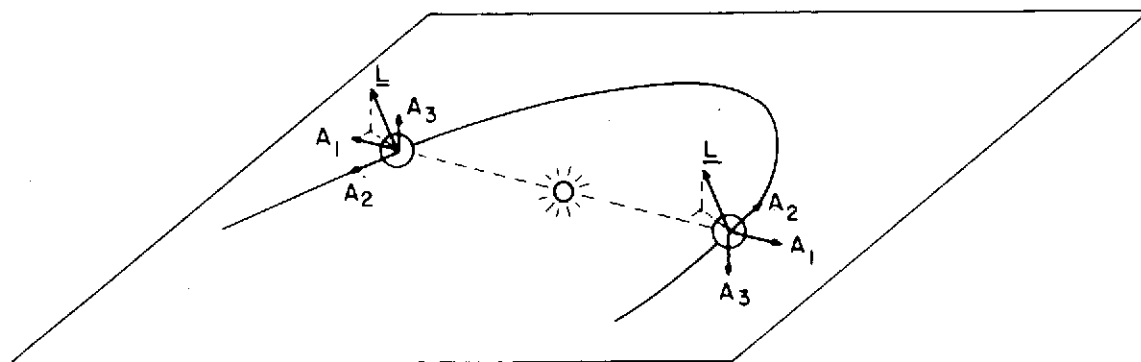
A$_1$ ALMOST ALWAYS POSITIVE (ENCKE SLIGHTLY NEGATIVE)

A$_2$ POSITIVE OR NEGATIVE, MAY SHOW SECULAR DECREASE,
        MAY CHANGE SIGN (ENCKE'S A$_2$ DECREASING)

A$_1$/A$_2$ TYPICALLY ~10   BUT ≪10 FOR ENCKE

Figure 11.   Nuclear Rotation and Non-Gravitational Acceleration
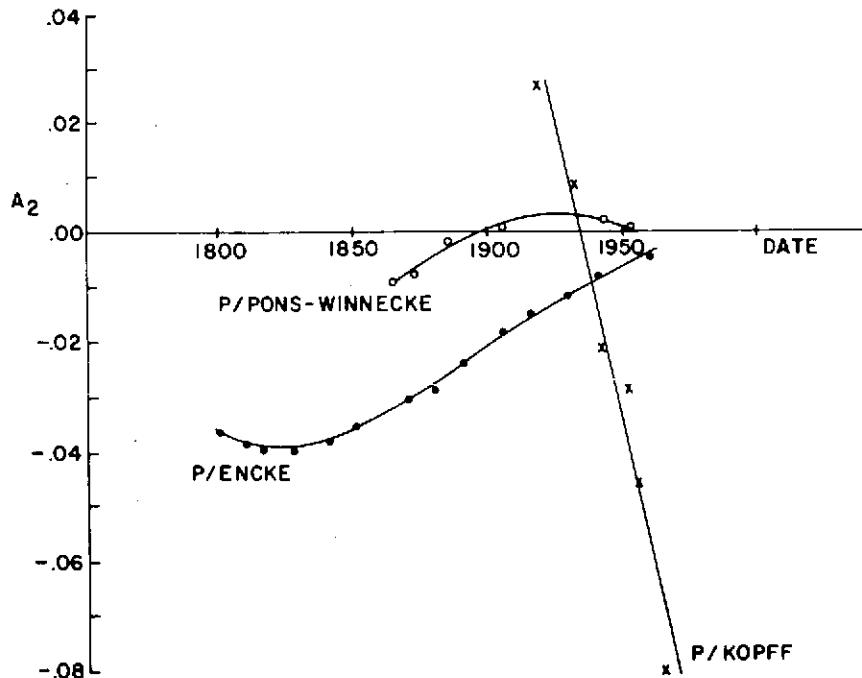
Figure 12.   Secular Changes in Transverse Non-Gravitational
Acceleration of Several Short Period Comets

20

Vanysek, Meisel, Sekanina, Bortle). A quantitative determination of the decrease in brightness is made difficult because of greater dust loads in the air in modern times, extensive background sky brightness at low elevations, dependence of magnitude estimates on telescope aperture, the great variability in viewing geometry for successive apparitions, increasing light pollution, and so forth. Beyer, in this century, and Holetschek, in the last, are responsible for the two sets of observations which are most internally consistent and which span several apparitions. Beyer's magnitude estimates for successive apparitions have been reduced to a common magnitude law by Sekanina by introducing residual magnitudes (m_i). Sekanina derived a secular decrease of 0.1 magnitudes per revolution from Beyer's data. We have performed a similar renormalization and find somewhat smaller values for the residual magnitudes and thus for the secular decrease (<0.05 magnitudes per revolution). Beyer's data (renormalized by Mumma) and data taken during the 1974 apparition are shown in Figure 13. Bortle (private communication), using the same data but a slightly different analysis, concludes that Encke shows no secular decrease. It should be noted that our residual magnitudes are essentially constant for 1937 and 1947, and again nearly constant for 1951 through 1974. Thus, except for a step function between 1947 and 1951 the brightness would seem to be nearly constant. (Mumma believes this step function is the result of increased sky brightness over Hamburg after World War II, tending to lower the apparent cometary brightness.) However, for the purposes of this report, we adopt Sekanina's value for the secular decrease (0.1 magnitudes per revolution) since this establishes a lower limit to the expected total brightness in 1980.

The brightness clearly tends toward an inverse square dependence (n = 2) on heliocentric distance (R) at small R, which is consistent with the assumption that the available solar radiation limits the gas production rate. This is made reasonable by the following argument. The intensity of light radiated by a particular molecular species is given by

$$I_i \sim g_i N_i \qquad (1)$$

where I_i is the total number of photons radiated per second into 4π steradians by the species in question, g_i is the solar g-factor for the molecular band system or atomic line in question, and N_i is the total number of the species in the coma in the lower electronic state. Also,

$$N_i \sim Q_i \tau_i \qquad (2)$$

where Q_i is the production rate and τ_i is the mean lifetime, or

$$I_i \sim g_i Q_i \tau_i \sim (g_1 \tau_1)_i R^{-2} Q_i R^2 \qquad (3)$$

21
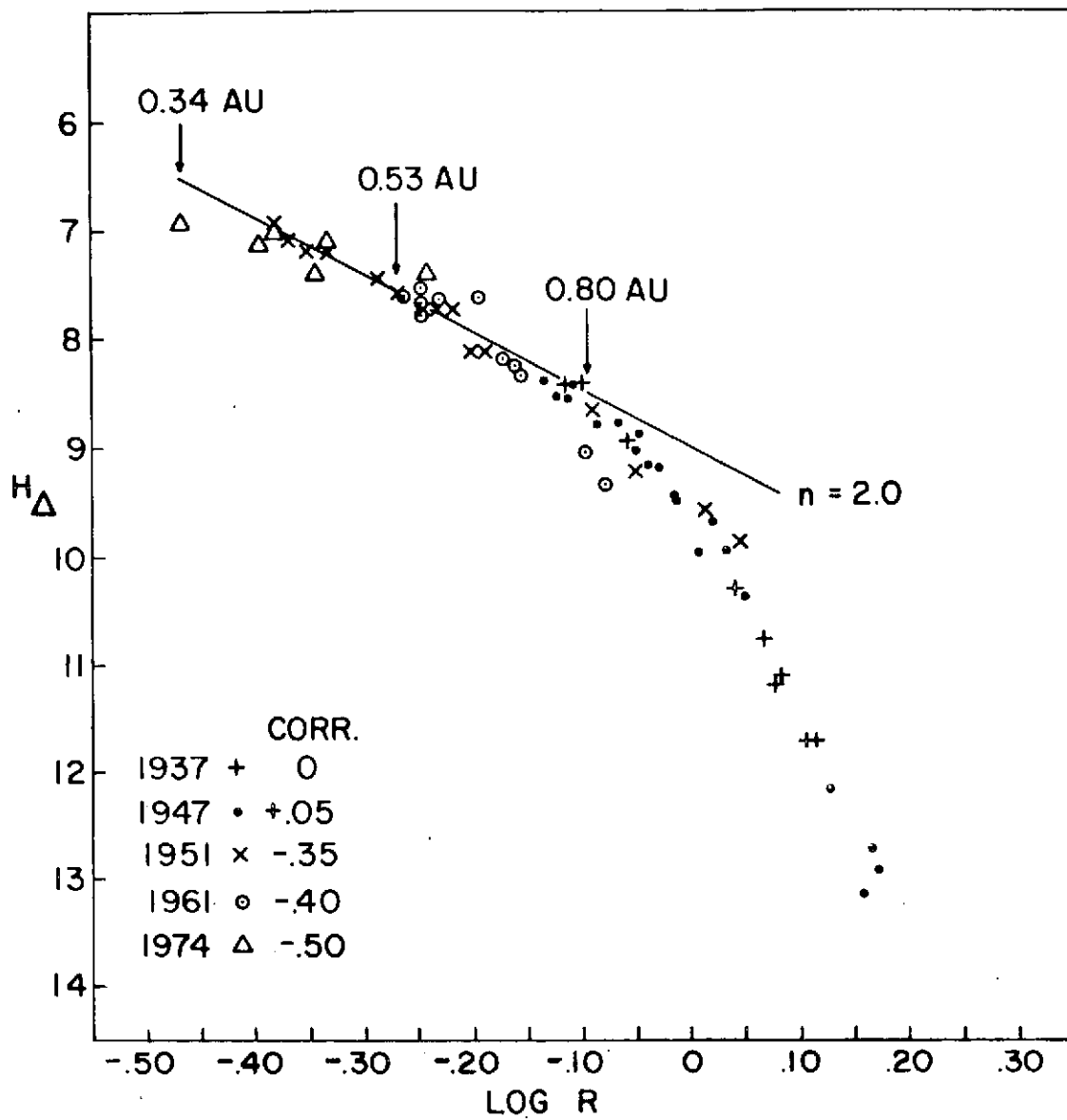
Figure 13.   Total Brightness vs. Heliocentric Distance

or

$$I_i \sim (g_1 \tau_1)_i \, Q_i \tag{4}$$

If Q_i is limited by the available solar radiation then

$$I_i \sim (g_1 \tau_1 Q_1)_i \, R^{-2} \tag{5}$$

22

i.e., the limiting brightness law is as the inverse square of R. For the past 12 returns to perihelion, Encke's brightness has regularly approached an inverse square law (R<0.8 AU), in agreement with Equation (5).

The total magnitude (T_{mag}) is given by

$$T_{mag} = 8.9 + 5 \log \Delta + 5 \log R \qquad (6)$$

from $R \simeq 0.8$ AU to $R \simeq 0.34$ AU (perihelion). Equation (6) is the relation obtained if all subsequent observations are reduced to the 1937 apparition. The corresponding brightness for the 1980 return will be smaller by the secular decrease between 1937 and 1980 or by about 1.4 magnitudes if Sekanina's estimate of 0.1 magnitudes per revolution is accepted, i.e.,

$$T_{mag} = 10.3 + 5 \log \Delta + 5 \log R \quad 0.34 \text{ AU} \lesssim R \lesssim 0.8 \text{ AU} \qquad (7)$$

We also adopt the following law for the nuclear magnitude (N_{mag}) based on Roemer's data (see Appendix II),

$$N_{mag} = 16.0 + 5 \log \Delta + 5 \log R + 0.03\beta \qquad (8)$$

where β is the phase angle, Δ the comet-observer distance in AU, and R is the sun-comet distance in AU. The nuclear magnitude is assumed to remain invariant through 1980. In contrast to Encke's regular behavior prior to perihelion, the comet sometimes shows flaring and irregular behavior several weeks after perihelion (Dossin, Roemer). Furthermore, the brightness after perihelion is generally about a factor of three (or one astronomical magnitude) weaker than at corresponding distances before perihelion (Sekanina). This behavior was observed to hold in 1974 (Bennett) when Encke's brightness at P+30 days was found to be about one magnitude smaller than that at P-30 (Fig. 13). Thus, while Encke appears to fade somewhat well after perihelion, the pre-perihelion data show that Encke's brightness is developing as expected at least to within one day of perihelion.

Delsemme has shown that reasonable estimates of the nuclear radius and Bond albedo can be obtained for comets Tago-Sato-Kosaka (1969 IX) and Bennett (1970 II) by comparing the gas production rate at small heliocentric distances and the brightness at large heliocentric distances where reflected sunlight dominates the brightness. Unfortunately, this procedure does not work well for Comet Encke and Delsemme interprets this to mean that the nucleus of Encke is only partially ice-covered or that the vaporization of water ice does not control the production rate of hydrogen. However, a lower limit to the radius (r_{min}) may be established

by assuming that all of the solar radiation at 0.7 AU is effective in vaporizing water ice, i.e.,

$$F_\odot R^{-2} \; \pi \, r_{min}^2 \; = \; Q_{H_2O} \; L \qquad (9)$$

where $F_\odot$ = solar flux at 1 AU (0.03 cal cm^{-2} sec^{-1}), R = heliocentric distance (AU), Q_{H_2O} = production rate of H_2O molecules/sec, and L is the heat of sublimation of water ice near 200 K (11,500 cal/mole or 1.9×10^{-20} cal/molecule). Then,

$$r_{min} \; = \; 0.17 \, Km \qquad (10)$$

Other limits on the size of the nucleus can be established from the measured brightness at distances large enough that sun light reflected from the nucleus is the dominant source of brightness. In this case,

$$\log \, [pD^2 \phi(\beta)] \; = \; 0.4(M_\odot - M_c) + 2 \log R\Delta \qquad (11a)$$

where p is the geometric albedo, D is the nuclear radius, $\phi(\beta)$ is the phase law, β is the phase angle, $M_\odot$ = solar magnitude, and M_c the cometary magnitude. This can be written

$$N_{mag} \equiv M_c \; = \; M_o + 5 \log r\Delta + a_1 \beta \qquad (11b)$$

where $a_1 = 2.5 \, \beta^{-1} \, \log \, [\phi(\beta)]$. Roemer's data give $pD^2 \simeq 0.7$ (taken at aphelion in 1972) and $pD^2 \simeq 0.13$ (at r = 2.9 AU in 1973) (Appendix II). Observations in 1963 give $pD^2 \simeq 0.22$ and $a_1 = 0.013$. A geometric albedo of ~0.1 would indicate a radius of ~2.7 Km using the 1972 data, although a wide range of effective radii can be derived depending on the assumed albedo. An upper limit of ~6 Km is set by assuming a geometric albedo of 0.02 which is less than the lowest known asteroidal albedo (0.027).

The import size parameters for the purpose of this study are the minimum radius (0.17 Km) and the nominal design radius (chosen to be 1 Km) which together allow us to model the science return of the imaging experiment (Sec. 4.1.2).

3.2   Gas

As discussed earlier, insolation appears to limit the production of gas for heliocentric distances less than about 0.8 AU. We therefore take as our baseline model for parent molecule production a rate which increases as R^{-2}. We normalize the H_2O production rate at 0.71 AU to one-half the hydrogen atom production rate observed by Bertaux et al., in 1971 (the adopted secular decrease would

further reduce this by about 25% in 1980). Thus,

$$\frac{Q_{H_2O}}{4\pi}(0.7\,AU) = 2.5 \times 10^{26} \text{ steradian}^{-1}\text{ sec}^{-1} \tag{12a}$$

and

$$\frac{Q_{H_2O}}{4\pi}(R) = 1.2 \times 10^{26}\,R^{-2}\text{ steradian}^{-1}\text{ sec}^{-1}, R \text{ in AU} \tag{12b}$$

We also assume uniform gas production per cm^2 of area from a spherical nucleus (point source model). This leads to lower gas densities in the sunward direction than if we had assumed emission only from the sunward hemisphere, but higher densities than would be present within an icy halo. A simple flow model then leads to gas densities in the coma given by

$$n(D, R) = \frac{n_0(1\text{ km}, 1\,AU)}{R^2}\frac{v_0}{v_T D^2}\exp\left(-\frac{(D-1)}{v_T \tau_1 R^2}\right) \tag{13}$$

where V_T is the terminal flow velocity and τ_1 is the lifetime of the parent molecule against photodissociation at $R = 1\,AU$ (Fig. 14). It did not seem worthwhile to use the frictional flow model of Mendis, Holzer, and Axford because the gas densities and corresponding collision frequencies are low and because a spherical model is only an approximation anyhow. The initial thermal velocity (v_0) at the surface of the nucleus changes slowly with heliocentric distance. The relative production rates of all other parent molecules are taken to be constant relative to water, such as would be the case for a clathrate icy nucleus. For convenience trace molecules are each assumed to be 1% as abundant as H_2O.

The photodissociation lifetime of H_2O at $1\,AU$ is taken to be ~7 x 10^4 sec and is assumed to vary as R^2. All other species are assumed to have the lifetimes given by Potter and del Ducca, which are subject to some uncertainty but are the only ones available at the present time.

3.3 Dust

The dust distribution has been modelled after Finson and Probstein's results for Arend-Roland, and the brightness of Mie-scattered sunlight from dust particles in the field-of-view of the imaging experiment has been determined (Appendix III). The dustscattered background light (watts/cm^2 srμm) is 10^2 to 10^3 times smaller than the light reflected from the nucleus showing that the imaging experiment should have no trouble 'seeing' the nucleus through the intervening dust. The large difference between the nuclear brightness and dust brightness allows for a sizeable error in the dust abundance. Even a 10-fold increase in dust would not prejudice imaging of the nucleus.
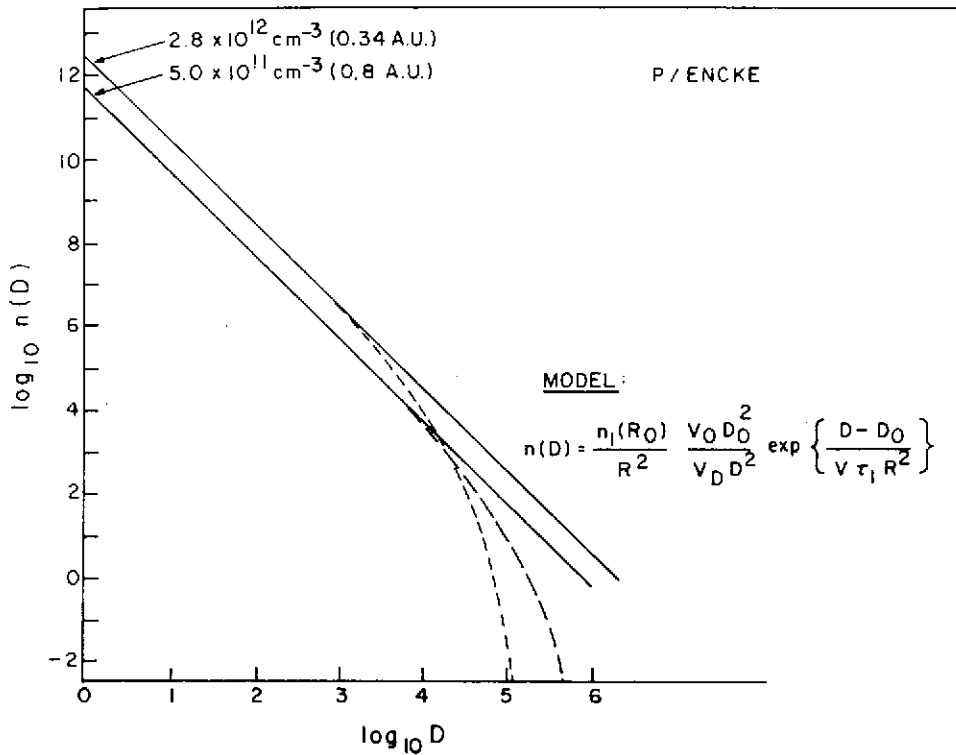
Figure 14. H_2O Density vs. Distance from the Nucleus

A detailed dust-impact hazard analysis is beyond the scope of this study.

4.0 EXPECTED SCIENCE RETURN

4.1 Experiments Which Are Strongly Dependent on the Mission Mode

4.1.1 Neutral Mass Spectrometer

The instantaneous counting rate of a molecular species seen by a neutral mass spectrometer at encounter is given by

$$\frac{dN}{dt} = EG \, n(D, R) \tag{14}$$

Where E is the detection efficiency (taken to be 1 count/sec per 1000 molecules/cm^3), G is the duty cycle, and n is the local number density at a distance D from the nucleus (Eq. 13). The number of counts detected for a particular ion per

unit kilometer of flight path is given by

$$\frac{dN}{dL} = v^{-1} \frac{dN}{dt} \tag{15}$$

or

$$\frac{dN}{dL} \simeq \frac{GE\,Q(R)}{4\pi(L^2 + D_m^2)V_T} \exp[-(L^2 + D_m^2)^{\frac{1}{2}}/V_T\tau_1 R^2] \tag{16}$$

$$= C1(L^2 + D_M^2) \exp[-C2(L^2 + D_m^2)^{\frac{1}{2}}]$$

dN/dL has been calculated for each mission concept for 16 different sets of data, representing the combinations of the values for (Q, τ, D_M) given in Table VII. The entries labeled 1% Q_{H_2O} apply either for (G=1, 1% H_2O abundance) or for (G=0.01, H_2O abundance). The results for dN/dL are shown as the solid lines in Figures 16 through 31.

Table VII

Baseline Data for Neutral Mass Spectrometer Study

	Mission 1 0.34 AU	Mission 2 0.53 AU	Mission 3 0.80 AU
C1: (Q_{H_2O})	3.2E8	6.1E7	1.8E7
(1% Q_{H_2O})	3.2E6	6.1E5	1.8E5
C2: $(\tau_1 = 7E4 \text{ sec})$	6.9E5	2.8E-5	1.25E-5
$(\tau_1 = 3.5E3)$	1.38E-3	5.6E-4	2.5E-4
$D_m : R_{EZ} = 0,$ w-OBN	95	98	62
wo-OBN	510	403	302
$R_{EZ} = 400,$ w-OBN	471	566	515
wo-OBN	865	1017	996

27

The number of measurements of a species on a given flyby has been estimated by integrating from L_1 to L_2 along the flight path (beginning at 32,000 Km) until the error in the accumulated counts ($N^{-1/2}$) is equaled or exceeded by the error in cometocentric distance ($\Delta D/\overline{D}$) for that measurement (Fig. 15). An 'X' is then plotted at the center of the interval (L_1, L_2) and the process is begun again at L_2. The distance D at which the combined measurement error falls below 10% is marked by a vertical line on each curve. The number of measurements obtained having errors less than 10% on the flight path in to D_M is shown at the upper left of each curve, and the % error of the measurement at $D = D_M$ is also shown. In some cases, the % error of the first measurement is shown at the extreme lower right. The science return can thus be compared for various missions by inspection.
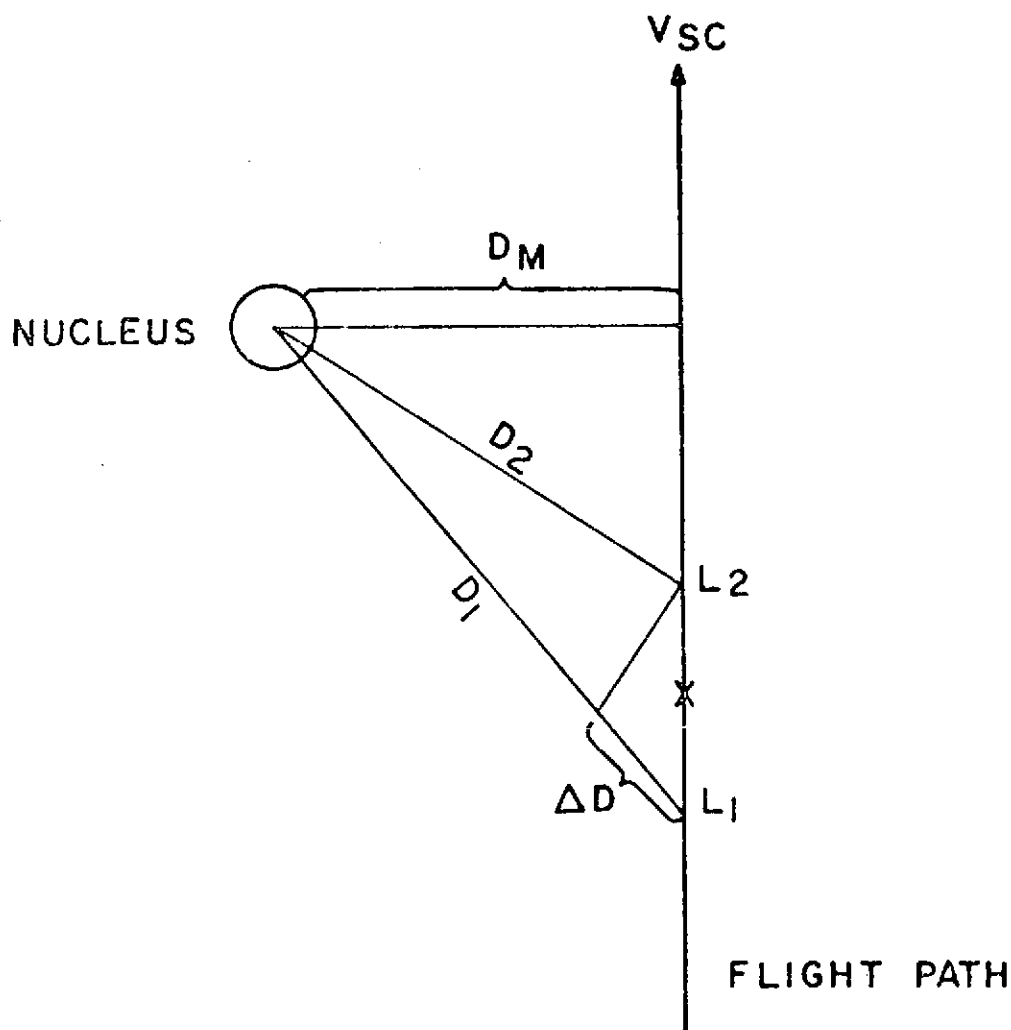
Figure 15. Flyby Geometry at Encounter

A note of caution should be introduced. If a sizeable amount of H_2O is locked in icy grains in the inner coma, the H_2O densities will begin to fall progressively further below the values given by the point source model as D decreases from the value (say D_H) corresponding to the outer limits of the icy halo ($D_H \sim 1000$ Km ?). Any departure of the gas densities from a D^{-2} distribution would only be recognized on those intercept missions for which the accuracy had already reached 10% or better at distances greater than D_H.

The first case considers measurements of H_2O with 100% duty cycle and shows that all intercept missions return adequate measurements of H_2O (Figs. 16-19). Even for the worst case considered (no on-board navigation, and a 400 Km exclusion zone), H_2O measurements reached 10% accuracy at $\sim 4,000$ Km from the nucleus at 0.8 AU and ~ 74 measurements can be expected. The minimum distance of approach is ~ 1000 Km in all three missions, but at 0.34 AU measurements begin at 20,000 Km and ~ 260 measurements are obtained. An icy halo may never be entered in these cases, however.

The case of a trace constituent with the lifetime of H_2O ($\sim 20R^2$ hours) but only 1% as abundant is shown in Figures 20-23. This can be viewed as the science return for H_2O if a 1% duty cycle mass spectrometer is used. Then the 10% error point is reached before entering the icy halo (1000 Km) only on the perihelion intercept. On-board navigation would definitely be required to return adequate data.

The next case considers a hypothetical major consituent but with a one-hour lifetime at 1 AU (Figs. 24-27). The production rate is assumed equal to the H_2O production rate. The 10% error point is reached at nearly the same distance (D ~ 2000 Km) on all three missions, in spite of the short lifetime. The science return is adequate for all cases except that for $R_{EZ} = 400$, and without on-board navigation (Fig. 27) for which the icy halo is barely penetrated; however, the number of measurements even for this case is adequate outside D = 100 Km.

The final case considers a trace molecule 1% as abundant as H_2O but with a one-hour lifetime at 1 AU (Figs. 28-31). Only a perihelion intercept with $R_{EZ} = 0$ and on-board navigation (Fig. 28) has a hope of adequate data return and then only if the radius of an icy halo is small (say ~ 100 Km) or if the fraction of trace volatiles locked an ice grains is small.

4.1.2 Imaging

A detailed study of the imaging experiment has been carried out. We have assumed a vidicon camera of the Mariner-1971 B-type on an attitude stabilized platform (either 3-axis or de-spin). The brightnesses of the coma and nucleus are as described in Section 3.1 and in Appendix IV. The miss distances of

29

Figure 16

Q_{H_2O}
$\tau = 7(+4)$
$R_{EZ} = 0$
W - OBN

$\log \frac{dN}{dL}$

LOG D

(236).6
(171).6
(129) 1

13
15
25

Figure 17

Q_{H_2O}
$\tau_1 = 7(+4)$
$R_{EZ} = 0$
WO - OBN

LOG $\frac{dN}{dL}$

LOG D

(162).8
(118) 1
(76) 2

13
15
25

Figure 18

Q_{H_2O}
$\tau_1 = 7(+4)$
$R_{EZ} = 400$
W - OBN

LOG $\frac{dN}{dL}$

LOG D

(176).6
(94) 1
(58) 2

13
15
25

Figure 19

Q_{H_2O}
$\tau_1 = 7(+4)$
$R_{EZ} = 400$
WO - OBN

LOG $\frac{dN}{dL}$

LOG D

(132).8
(69) 2
(37) 3

13
15
25
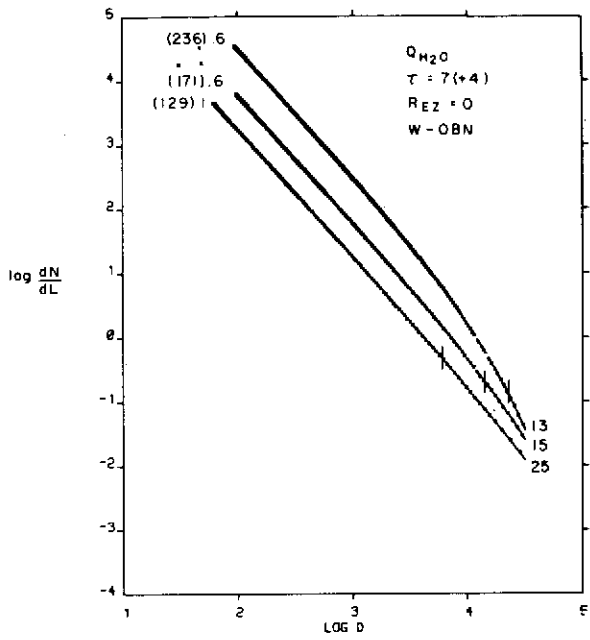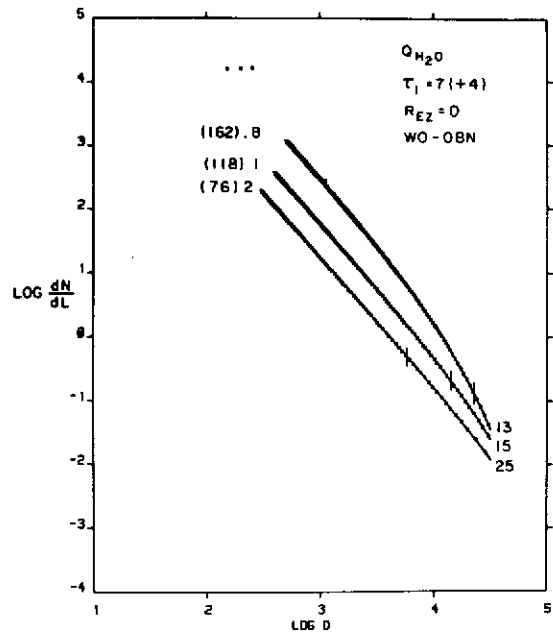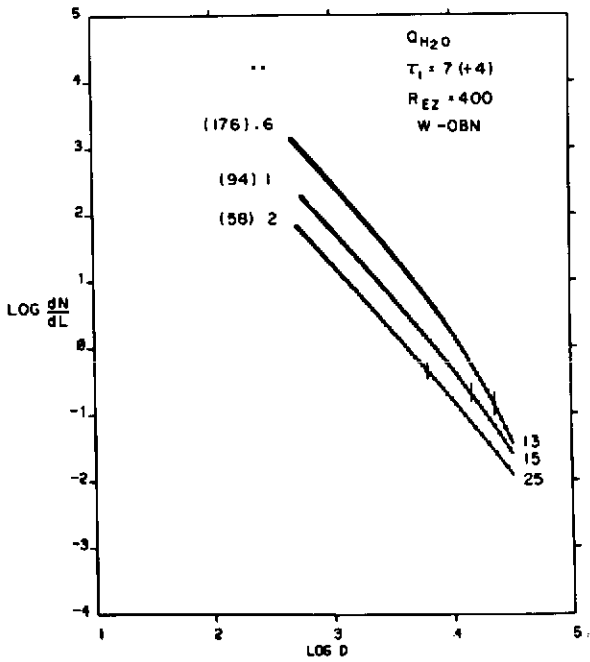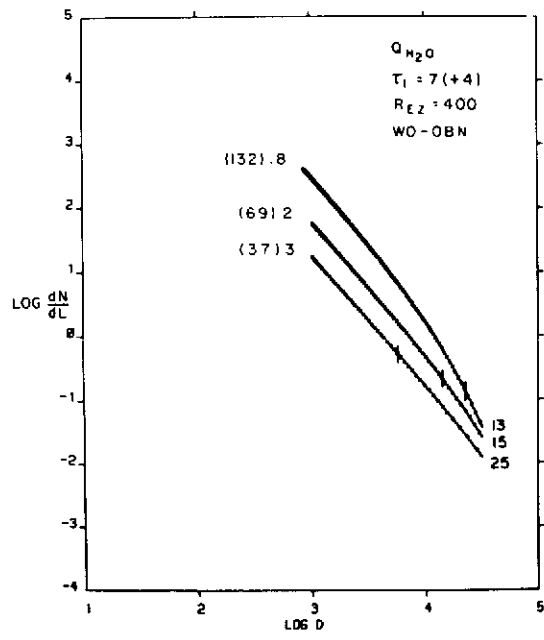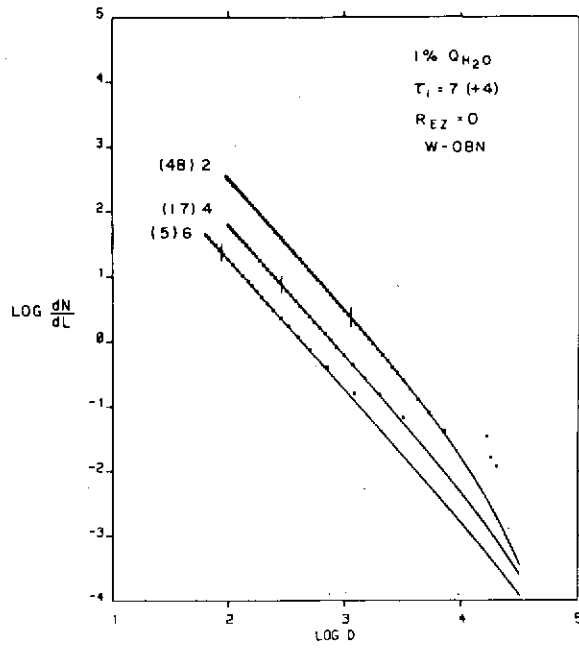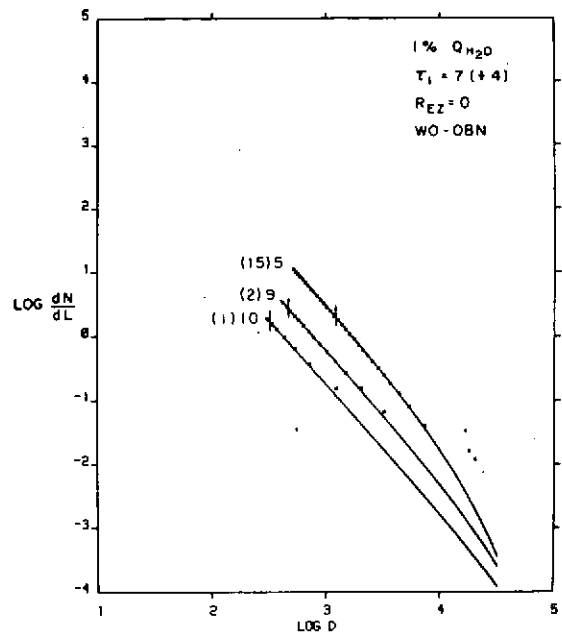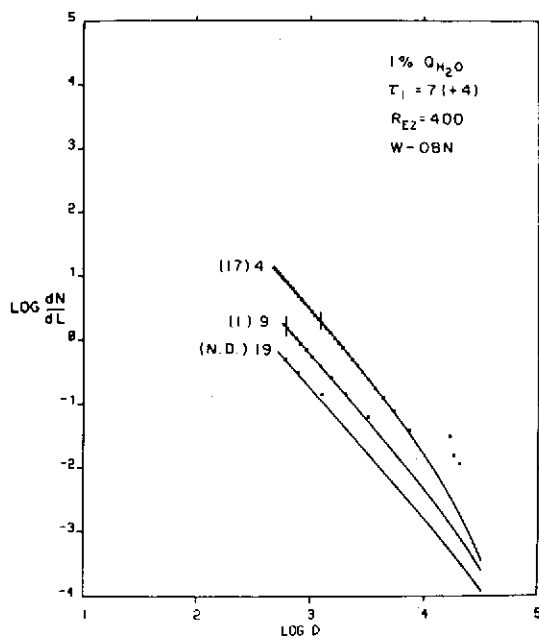
Figure 20

Figure 21

Figure 22
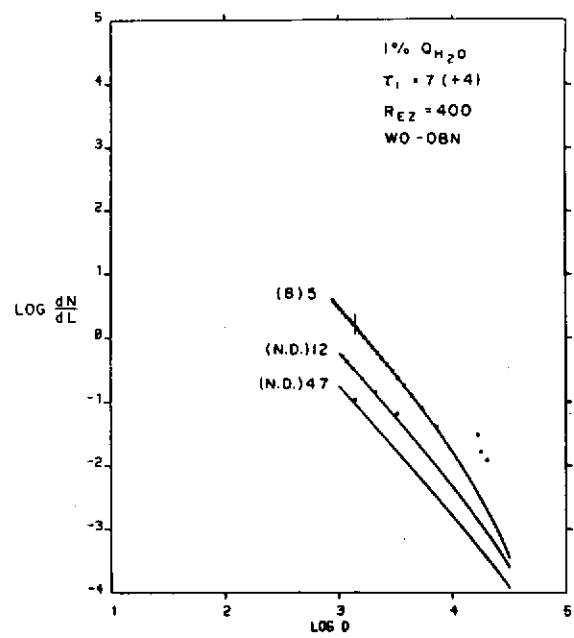
Figure 23
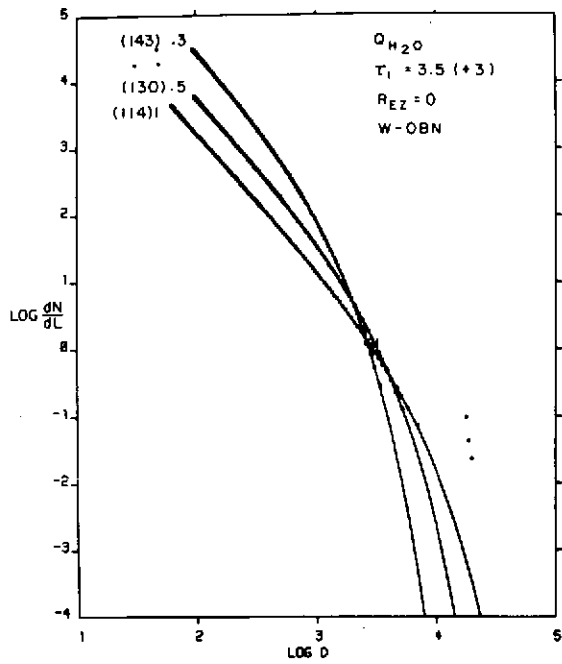
Figure 24
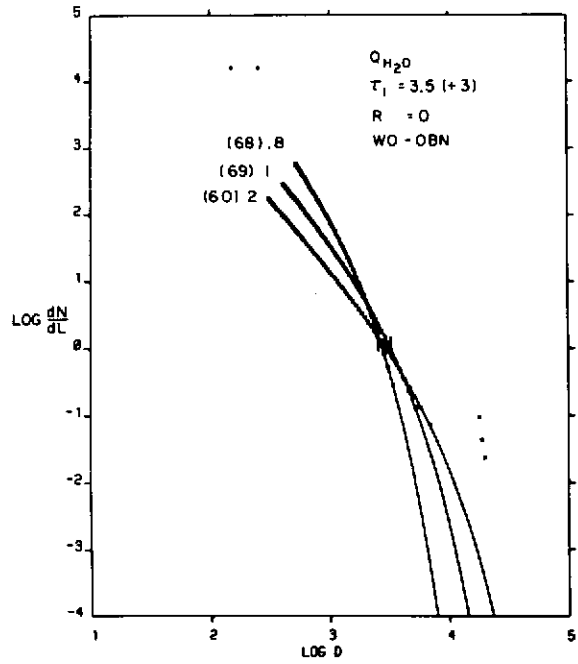
Figure 25
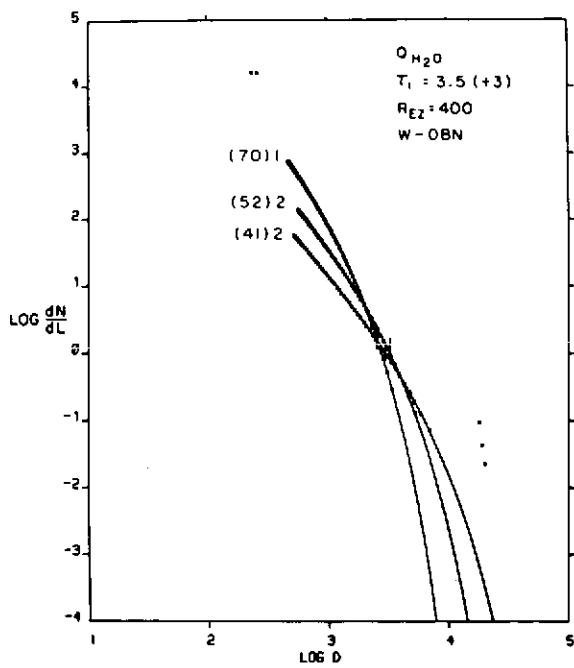
Figure 26
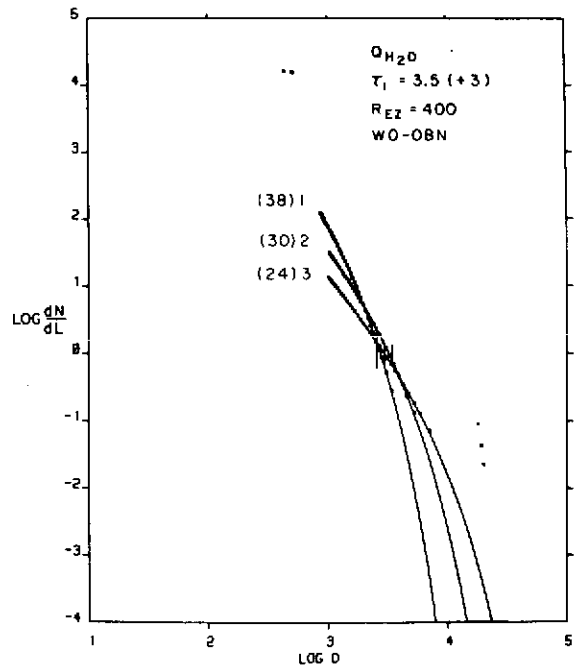
Figure 27
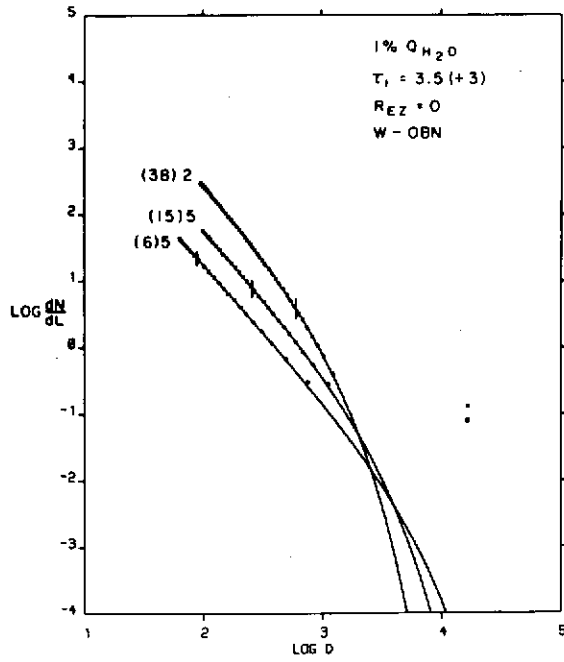
Figure 28
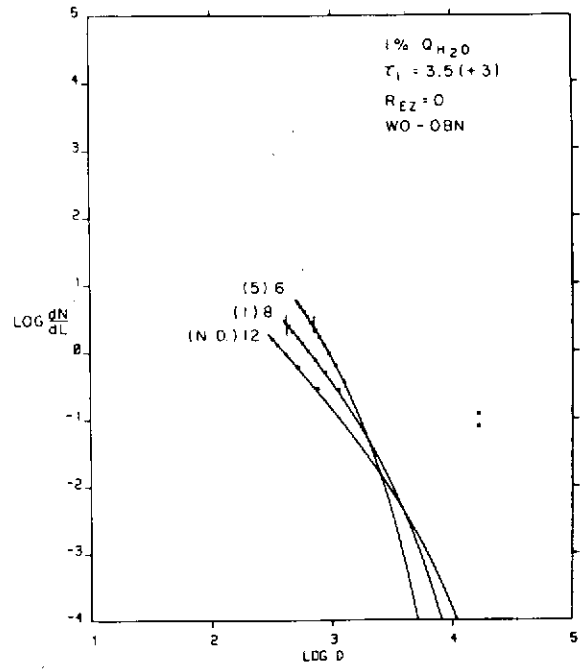
Figure 29
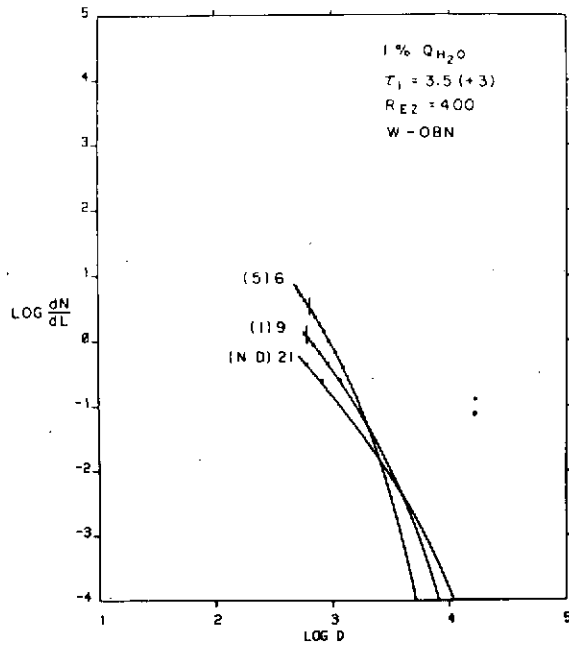
Figure 30
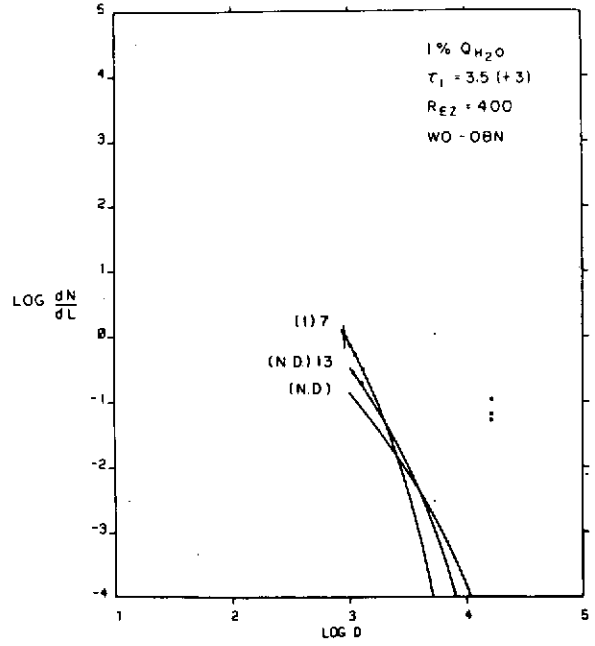
Figure 31

Section 2.3 have been used in modelling the imaging results for each of the 12 missions treated (with/without optical navigation; with/without an exclusion zone; for R = 0.34, 0.53, 0.80 AU). The results of interest are: total number of pictures returned, spatial extent per picture element (pixel) for the best frame, and the number of days before encounter for earliest nucleus detection (this impacts on the feasibility of terminal navigation).

The results are summarized in Tables VIII and IX, for further details see Appendix IV.

4.1.3 Optical Particle Detector; Impact Detector and Analyser

It is assumed that an optical particle detector can be built, patterned after Sisyphus but without the obvious problems encountered by Sisyphus. It is further assumed that with proper background rejection filtering that the instrument will have a "range to particle radius ratio" of at least 10^5 at 0.8 AU for geometric albedos of 0.1. For calculation purposes the nominal symmetric dust model of Taylor, et al., is assumed. No account is taken of any change of emission with heliocentric distance. Inside 1000 km (cometocentric distance) additional counts can be expected from icy grains. Because of the great uncertainty in size and number of these grains, they are not included in the comparison, but they obviously will increase the count on 100 and 500 km flybys (also see Appendix III).

Table VIII

Comet-Sun Encounter Range Effects on Imaging

Parameter	Case I	Case II	Case III
Encounter-Sun Distance (AU)	0.34	0.53	0.80
Flyby Velocity (km/s)	8.6	18.0	26.8
Encounter Duration (sec) 2 km > 5 pixels	3000	1480	545
Smear Rate at Encounter (pixels/sec)	287	600	895
Earliest Nucleus* Resolution (days)	E - 3	E - 1.6	E - 0.8
With 10% coma filter	E - 7	E - 2.5	E - 1.6

*Assumes: $M = 16 + 5 \log R + 5 \log \Delta + 0.03g$
Nucleus Diameter = 2 km
$p\ r^2 = 0.24$

Table IX

Comet-Sun Encounter Range Effects on Imaging

Parameter	Case I	Case II	Case III
	50 K bits/sec	120 K bits/sec	120 K bits/sec
No. of Pictures* w/o Recorder			
Large Frames (84 sec/fr)	33 (4**)	18	7
Large Frames (10 sec/fr)	33 (4**)	39	14
Small Frames (15 sec/fr)	94 (8**)	39	36
No. of Pictures* w Recorder			
Large Frames	36	18	7
Large Frames	240	148	55
Small Frames	200	148	55

*Assumes: Large frame = 4.5×10^6 bits;
Small frame = 1.6×10^6 bits;
Despun Platform
**Without despun platform;
Bit rate is 4 K bits/sec

There are only two large differences in the three mission classes. The particles
emitted are brighter nearer the Sun, the "range to radius ratio" increasing lin-
early with solar distance, and the count rate at any given distance from the comet
is obviously a function of the spacecraft velocity. The tables and graphs for this
instrument therefore indicate the total counts as a function of size and the count
rate at closest approach to the cometary nucleus.

When the spacecraft velocity is much higher than the particle velocities it can
be assumed simply that the spacecraft is flying through a static distribution of
debris. The particle concentration C and the total particle fluence during the
flythru F are given by

$$C = \frac{E}{4 \pi R^2 \nu} \text{ and } F = \frac{E}{4 R_o \nu}$$

where E = particle emission rate from nucleus (#/s)
R = distance from nucleus (m)

ν = particle velocity (m s^{-1})

R_0 = distance of closest approach to nucleus (m)

The optical particle detector looks out in a fixed direction with a half cone angle α to a range r determined by the particle size. The maximum number of particles per second N and the total number of counts T are given by

$$N = C_{R_0} V r^2 \tan \alpha$$

and

$$T \sim F r^2 \tan \alpha$$

where V = velocity of the spacecraft (m s^{-1}). The equation for T is quite inaccurate for larger particles, since they can be seen at ranges which are large relative to the distance to the nucleus, distances at which the particle concentrations are very different from those in the immediate vicinity of the spacecraft. The actual values would be more difficult to calculate and would be a function of the instrument look angles.

It is assumed that the impact detector has an area of 10^{-2} m^2. Everything scales linearly with detector area, if some other value in fact pertains. The total number of counts t will just be the fluence on that area A. The maximum count rate n is just the concentration at closest approach, times the detector area, times the spacecraft velocity.

$$t = FA \qquad n = CVA$$

The data on dust taken from Taylor, et al., is as follows:

Size Range (m)	Emission Rate (E) (s^{-1})	Velocity* ($\bar{\nu}$) (m s^{-1})	Calculation Size (r_p) (m)
3×10^{-7} – 10^{-6}	2.5×10^{11}	300	6.5×10^{-7}
10^{-6} – 10^{-5}	2.5×10^{12}	150	5×10^{-6}
10^{-5} – 10^{-4}	2.5×10^{10}	50	5×10^{-5}
10^{-4} – 10^{-3}	2.5×10^{7}	15	5×10^{-4}
10^{-3} – 10^{-2}	2.5×10^{3}	3	5×10^{-3}
10^{-2} – 10^{-1}	2.5×10^{-1}	0.1	5×10^{-2}
10^{-1} – 2.5×10^{-1}	2.5×10^{-2}	0.01	1.75×10^{-1}

*These approximate velocities of the particles were calculated for 1 AU heliocentric distance and would be somewhat larger nearer the Sun.

0.8 AU 26 Km/sec 100 km approach

Size (m)	C (m^{-3})	F (m^{-2})	N (s^{-1})	T
$3 \times 10^{-7} - 10^{-6}$	6.63×10^{-3}	2.08×10^{3}	1.3×10^{-1}	1.5×10^{0}
$10^{-6} - 10^{-5}$	1.33×10^{-1}	4.17×10^{4}	1.5×10^{2}	1.8×10^{3}
$10^{-5} - 10^{-4}$	3.98×10^{-3}	1.25×10^{3}	4.6×10^{2}	5.5×10^{3}
$10^{-4} - 10^{-3}$	1.33×10^{-5}	4.17×10^{0}	1.5×10^{2}	1.8×10^{3}
$10^{-3} - 10^{-2}$	6.63×10^{-9}	2.08×10^{-3}	7.6×10^{0}	9.2×10^{1}
$10^{-2} - 10^{-1}$	1.99×10^{-11}	6.25×10^{-6}	2.3×10^{0}	2.8×10^{1}
$10^{-1} - 2.5 \times 10^{-1}$	1.99×10^{-11}	6.25×10^{-6}	2.8×10^{1}	3.4×10^{2}

0.8 AU 26 Km/sec 500 km approach

Size (m)	C (m^{-3})	F (m^{-2})	N (s^{-1})	T
$3 \times 10^{-7} - 10^{-6}$	2.65×10^{-4}	4.17×10^{2}	5.1×10^{-3}	3.1×10^{-1}
$10^{-6} - 10^{-5}$	5.31×10^{-3}	8.33×10^{3}	6.1×10^{0}	3.7×10^{2}
$10^{-5} - 10^{-4}$	1.59×10^{-4}	2.50×10^{2}	1.8×10^{1}	1.1×10^{3}
$10^{-4} - 10^{-3}$	5.31×10^{-7}	8.33×10^{-1}	6.1×10^{0}	3.7×10^{2}
$10^{-3} - 10^{-2}$	2.65×10^{-10}	4.17×10^{-4}	3.0×10^{-1}	1.8×10^{1}
$10^{-2} - 10^{-1}$	7.96×10^{-13}	1.25×10^{-6}	9.1×10^{-2}	5.5×10^{0}
$10^{-1} - 2.5 \times 10^{-1}$	7.96×10^{-13}	1.25×10^{-6}	1.1×10^{0}	6.7×10^{1}

0.8 AU 26 Km/sec 1500 km approach

Size (m)	C (m^{-3})	F (m^{-2})	N (s^{-1})	T
$3 \times 10^{-7} - 10^{-6}$	2.95×10^{-5}	1.39×10^{2}	5.70×10^{-4}	1.03×10^{-1}
$10^{-6} - 10^{-5}$	5.89×10^{-4}	2.78×10^{3}	6.74×10^{-1}	1.22×10^{2}
$10^{-5} - 10^{-4}$	1.77×10^{-5}	8.33×10^{1}	2.02×10^{0}	3.67×10^{2}
$10^{-4} - 10^{-3}$	5.89×10^{-8}	2.78×10^{-1}	6.74×10^{-1}	1.22×10^{2}
$10^{-3} - 10^{-2}$	2.95×10^{-11}	1.39×10^{-4}	3.37×10^{-2}	6.11×10^{0}
$10^{-2} - 10^{-1}$	8.84×10^{-14}	4.17×10^{-7}	1.01×10^{-2}	1.83×10^{0}
$10^{-1} - 2.5 \times 10^{-1}$	8.84×10^{-14}	4.17×10^{-7}	1.24×10^{-1}	2.25×10^{1}

0.53 AU 18 Km/sec 100 km approach

Size (m)	C (m^{-3})	F (m^{-2})	N (s^{-1})	T
$3 \times 10^{-7} - 10^{-6}$	6.63×10^{-3}	2.08×10^{3}	2.02×10^{-1}	3.53×10^{0}
$10^{-6} - 10^{-5}$	1.33×10^{-1}	4.17×10^{4}	2.39×10^{2}	4.18×10^{3}
$10^{-5} - 10^{-4}$	3.98×10^{-3}	1.25×10^{3}	7.18×10^{2}	1.25×10^{4}
$10^{-4} - 10^{-3}$	1.33×10^{-5}	4.17×10^{2}	2.39×10^{2}	4.18×10^{3}
$10^{-3} - 10^{-2}$	6.63×10^{-9}	2.08×10^{-3}	1.20×10^{1}	2.09×10^{2}
$10^{-2} - 10^{-1}$	1.99×10^{-11}	6.25×10^{-6}	3.59×10^{0}	6.26×10^{1}
$10^{-1} - 2.5 \times 10^{-1}$	1.99×10^{-11}	6.25×10^{-6}	4.40×10^{1}	7.67×10^{2}

0.53 AU 18 Km/sec 500 km approach

Size (m)	C (m^{-3})	F (m^{-2})	N (s^{-1})	T
$3 \times 10^{-7} - 10^{-6}$	2.65×10^{-4}	4.17×10^{2}	8.09×10^{-3}	7.06×10^{-1}
$10^{-6} - 10^{-5}$	5.31×10^{-3}	8.33×10^{3}	9.57×10^{0}	8.35×10^{2}
$10^{-5} - 10^{-4}$	1.59×10^{-4}	2.50×10^{2}	2.87×10^{1}	2.51×10^{3}
$10^{-4} - 10^{-3}$	5.31×10^{-7}	8.33×10^{-1}	9.57×10^{0}	8.35×10^{2}
$10^{-3} - 10^{-2}$	2.65×10^{-10}	4.17×10^{-4}	4.79×10^{-1}	4.18×10^{1}
$10^{-2} - 10^{-1}$	7.96×10^{-13}	1.25×10^{-6}	1.44×10^{-1}	1.25×10^{1}
$10^{-1} - 2.5 \times 10^{-1}$	7.96×10^{-13}	1.25×10^{-6}	1.76×10^{0}	1.53×10^{2}

0.53 AU 18 Km/sec 1500 km approach

Size (m)	C (m^{-3})	F (m^{-2})	N (s^{-1})	T
$3 \times 10^{-7} - 10^{-6}$	2.95×10^{-5}	1.39×10^{2}	8.99×10^{-4}	2.35×10^{-1}
$10^{-6} - 10^{-5}$	5.89×10^{-4}	2.78×10^{3}	1.06×10^{0}	2.78×10^{2}
$10^{-5} - 10^{-4}$	1.77×10^{-5}	8.33×10^{1}	3.19×10^{0}	8.35×10^{2}
$10^{-4} - 10^{-3}$	5.89×10^{-8}	2.78×10^{-1}	1.06×10^{0}	2.78×10^{2}
$10^{-3} - 10^{-2}$	2.95×10^{-11}	1.39×10^{-4}	5.32×10^{-2}	1.39×10^{1}
$10^{-2} - 10^{-1}$	8.84×10^{-14}	4.17×10^{-7}	1.60×10^{-2}	4.18×10^{0}
$10^{-1} - 2.5 \times 10^{-1}$	8.84×10^{-14}	4.17×10^{-7}	1.95×10^{-1}	5.12×10^{1}

0.34 AU 8 Km/sec 100 km approach

Size (m)	C (m^{-3})	F (m^{-2})	N (s^{-1})	T
$3 \times 10^{-7} - 10^{-6}$	6.63×10^{-3}	2.08×10^{3}	2.18×10^{-1}	8.58×10^{0}
$10^{-6} - 10^{-5}$	1.33×10^{-1}	4.17×10^{4}	2.58×10^{2}	1.01×10^{4}
$10^{-5} - 10^{-4}$	3.98×10^{-3}	1.25×10^{3}	7.75×10^{2}	3.04×10^{4}
$10^{-4} - 10^{-3}$	1.33×10^{-5}	4.17×10^{0}	2.58×10^{2}	1.01×10^{4}
$10^{-3} - 10^{-2}$	6.63×10^{-9}	2.08×10^{-3}	1.29×10^{1}	5.07×10^{2}
$10^{-2} - 10^{-1}$	1.99×10^{-11}	6.25×10^{-6}	3.88×10^{2}	1.52×10^{2}
$10^{-1} - 2.5 \times 10^{-1}$	1.99×10^{-11}	6.25×10^{-6}	4.75×10^{1}	1.86×10^{3}

0.34 AU 8 Km/sec 500 km approach

Size (m)	C (m^{-3})	F (m^{-2})	N (s^{-1})	T
$3 \times 10^{-7} - 10^{-6}$	2.65×10^{-4}	4.17×10^{2}	8.74×10^{-3}	1.72×10^{0}
$10^{-6} - 10^{-5}$	5.31×10^{-3}	8.33×10^{3}	1.03×10^{1}	2.03×10^{3}
$10^{-5} - 10^{-4}$	1.59×10^{-4}	2.50×10^{2}	3.10×10^{1}	6.09×10^{3}
$10^{-4} - 10^{-3}$	5.31×10^{-7}	8.33×10^{-1}	1.03×10^{1}	2.03×10^{3}
$10^{-3} - 10^{-2}$	2.65×10^{-10}	4.17×10^{-4}	5.17×10^{-1}	1.01×10^{2}
$10^{-2} - 10^{-1}$	7.96×10^{-13}	1.25×10^{-6}	1.55×10^{-1}	3.04×10^{1}
$10^{-1} - 2.5 \times 10^{-1}$	7.96×10^{-13}	1.25×10^{-6}	1.90×10^{0}	3.73×10^{2}

0.34 AU 8 Km/sec 1500 km approach

Size (m)	C (m^{-3})	F (m^{-2})	N (s^{-1})	T
$3 \times 10^{-7} - 10^{-6}$	2.95×10^{-5}	1.39×10^{2}	9.71×10^{-4}	5.72×10^{-1}
$10^{-6} - 10^{-5}$	5.89×10^{-4}	2.78×10^{3}	1.15×10^{0}	6.77×10^{2}
$10^{-5} - 10^{-4}$	1.77×10^{-5}	8.33×10^{1}	3.45×10^{0}	2.03×10^{3}
$10^{-4} - 10^{-3}$	5.89×10^{-8}	2.78×10^{-1}	1.15×10^{0}	6.77×10^{2}
$10^{-3} - 10^{-2}$	2.95×10^{-11}	1.39×10^{-4}	5.74×10^{-2}	3.38×10^{1}
$10^{-2} - 10^{-1}$	8.84×10^{-14}	4.17×10^{-7}	1.72×10^{-2}	1.01×10^{1}
$10^{-1} - 2.5 \times 10^{-1}$	8.84×10^{-14}	4.17×10^{-7}	2.11×10^{-1}	1.24×10^{2}

100 km approach

Size (m)	26 km/s	18 km/s	8 km/s
$3 \times 10^{-7} - 10^{-6}$	1.72×10^{0}	1.19×10^{0}	5.30×10^{-1}
$10^{-6} - 10^{-5}$	3.46×10^{1}	2.39×10^{1}	1.06×10^{0}
$10^{-5} - 10^{-4}$	1.03×10^{0}	7.16×10^{-1}	3.18×10^{-1}
$10^{-4} - 10^{-3}$	3.46×10^{-3}	2.39×10^{-3}	1.06×10^{-3}
$10^{-3} - 10^{-2}$	1.72×10^{-6}	1.19×10^{-6}	5.30×10^{-7}
$10^{-2} - 10^{-1}$	5.17×10^{-9}	3.58×10^{-9}	1.59×10^{-9}
$10^{-1} - 2.5 \times 10^{-1}$	5.17×10^{-9}	3.58×10^{-9}	1.59×10^{-9}

500 km approach

Size (m)	26 km/s	18 km/s	8 km/s
$3 \times 10^{-7} - 10^{-6}$	6.89×10^{-2}	4.77×10^{-2}	2.12×10^{-2}
$10^{-6} - 10^{-5}$	1.38×10^{0}	9.56×10^{-1}	4.25×10^{-1}
$10^{-5} - 10^{-4}$	4.13×10^{-2}	2.86×10^{-2}	1.27×10^{-2}
$10^{-4} - 10^{-3}$	1.38×10^{-4}	9.56×10^{-5}	4.25×10^{-5}
$10^{-3} - 10^{-2}$	6.89×10^{-8}	4.77×10^{-8}	2.12×10^{-8}
$10^{-2} - 10^{-1}$	2.07×10^{-10}	1.43×10^{-10}	6.37×10^{-11}
$10^{-1} - 2.5 \times 10^{-1}$	2.07×10^{-10}	1.43×10^{-10}	6.37×10^{-11}

1500 km approach

Size (m)	26 km/s	18 km/s	8 km/s
$3 \times 10^{-7} - 10^{-6}$	7.67×10^{-3}	5.31×10^{-3}	2.36×10^{-3}
$10^{-6} - 10^{-5}$	1.53×10^{-1}	1.06×10^{-1}	4.71×10^{-2}
$10^{-5} - 10^{-4}$	4.60×10^{-3}	3.19×10^{-3}	1.42×10^{-3}
$10^{-4} - 10^{-3}$	1.53×10^{-5}	1.06×10^{-5}	4.71×10^{-6}
$10^{-3} - 10^{-2}$	7.67×10^{-9}	5.31×10^{-9}	2.36×10^{-9}
$10^{-2} - 10^{-1}$	2.30×10^{-11}	1.59×10^{-11}	7.07×10^{-12}
$10^{-1} - 2.5 \times 10^{-1}$	2.30×10^{-11}	1.59×10^{-11}	7.07×10^{-12}

IN EACH FAMILY OF THREE CURVES,
THE HIGHER COUNT RATES CORRESPOND
TO THE CLOSER ENCOUNTERS

—•— 0.34 AU, 8 km/sec
—-▲-— 0.53 AU, 18 km/sec
—▲— 0.8 AU, 26 km/sec
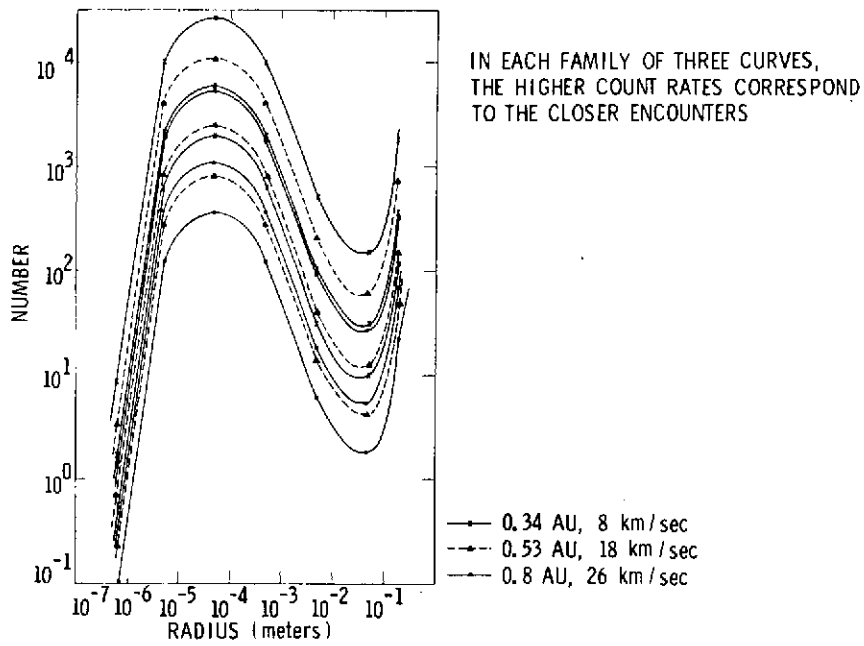
Figure 32. Optical Particle Detector (T) Total Counts
During Encounter

100 km

500 km

1500 km

—✳— 0.34 AU, 8 km/sec
—▲— 0.53 AU, 18 km/sec
—•— 0.8 AU, 26 km/sec
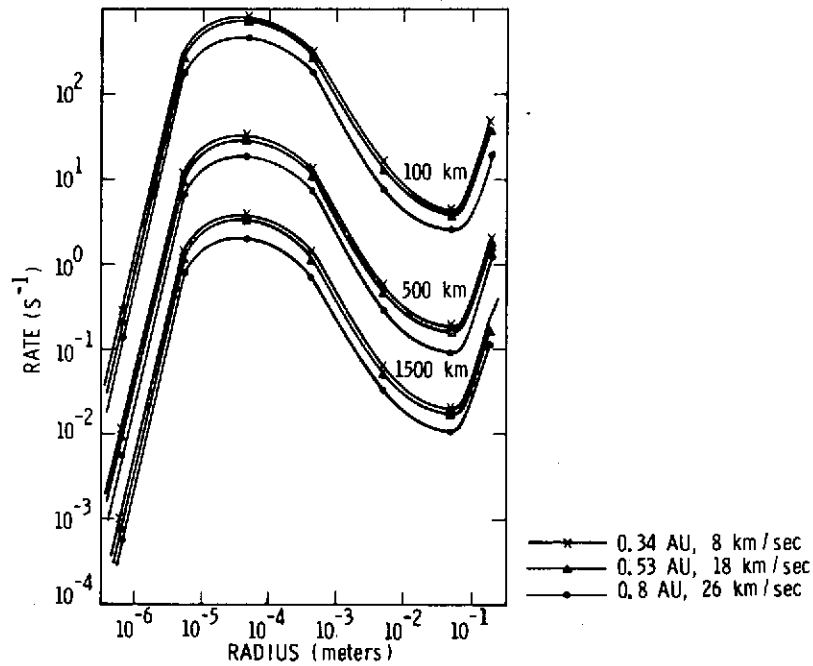
Figure 33. Optical Particle Detector (N) Maximum Count
Rate During Encounter

41
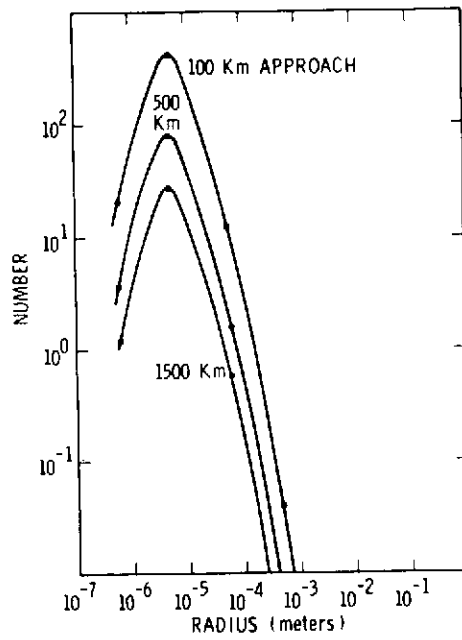
Figure 34. Impact Detector and
Analyzer (t) Total Impacts
During Encounter

26 km / sec, 0.8 AU
18 km / sec, 0.53 AU
8 km / sec, 0.34 AU
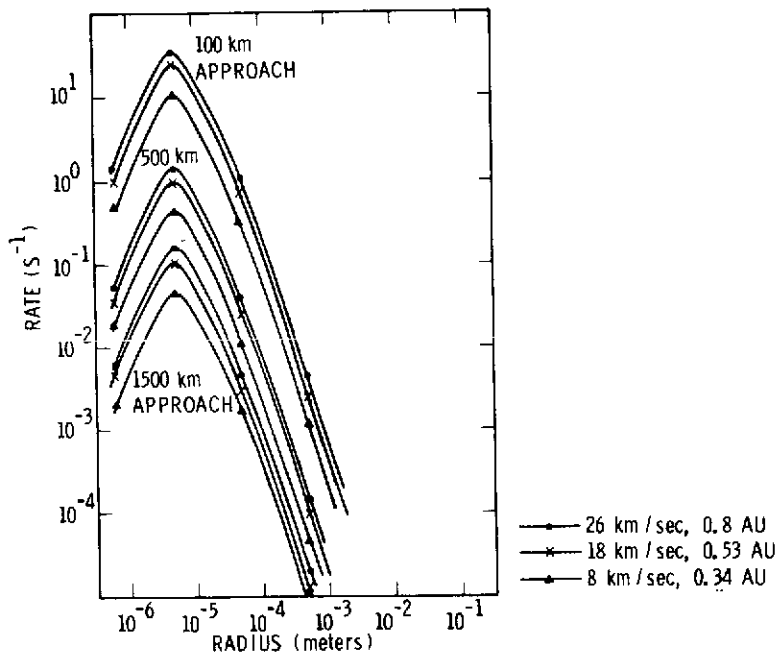
Figure 35. .Impact Detector and Analyzer (n) Maximum
Count Rate During Encounter

42

4.2 Experiments Which Are Independent of the Mission Mode

In addition to the experiments already discussed for which science return is strongly dependent on the heliocentric distance at intercept, there are some experiments which are expected to yield satisfactory results regardless of intercept point. This is not to say that the amount of data returned is independent of perihelion distance at intercept, rather that scientific return will be adequate for all cases.

The ion mass spectrometer experiment is expected to yield satisfactory results for all intercepts because of the high detection efficiency for ions (100% - as compared with 0.1% for neutral molecules in the neutral mass spectrometer experiment). However, because the energy distribution of cometary ions is expected to change drastically as the spacecraft moves from the transition zone to the inner coma, the focussing properties of the ion mass spectrometer must be carefully designed to ensure that the measurements can be correctly related to the in-situ ion densities and their velocity distributions (see also Section 6.3). If the design problems can be solved satisfactorily, the information return is expected to be adequate for each of the three intercepts discussed here.

The magnetic field experiments (A.C. and D.C.) and electric field experiments (A.C. and D.C.) are expected to return adequate data at all three intercept distances. Existing instruments have been used successfully on both three-axis-stabilized and spinning spacecraft to measure the fields in the un-shocked and shocked solar wind. Since these fields increase with decreasing heliocentric distance, the measurements should become progressively easier (e.g., requiring progressively shorter antenna length in the case of the E-field experiment) as R decreases from 0.8 to 0.34 AU.

5.0 MAJOR ISSUES AS A FUNCTION OF INTERCEPT

This study has resulted in identifying the following tradeoffs which have major impact on the cost and/or scientific return of a ballistic mission to Comet Encke in 1980.

1. A Titan-3E/Centaur launch vehicle is required for intercept missions at 0.34 and 0.53 AU whereas an intercept at 0.8 AU (for a Pioneer S/C or one of similar weight) can be accomplished with the much-cheaper Atlas/Centaur/TE364-4. A Pioneer can actually be launched to intercept at 0.53 AU using an Atlas/Centaur/TE364-4 but the S/C cannot handle the thermal loads imposed at this heliocentric distance (see (4) on the following page.

2. The S/C velocity relative to the comet is lowest (~8 Km/sec) for an 0.34 AU intercept and rapidly increases with heliocentric distance (~15 Km/sec at 0.53 and ~26 Km/sec at 0.8 AU). As we shall see, the science return is a strong function of the flyby speed, with higher science return at lower velocities.

3. The median miss distances (assuming an exclusion zone 400 Km in radius) are approximately the same for all three missions, being ~500 Km if on-board navigation is available and ~1000 Km if it is not. If no exclusion zone is assumed, then the median miss distances are in the neighborhood of ~100 Km and ~400 Km, respectively (see Table VI).

4. The solar heat load on the S/C is greatest at 0.34 AU presenting an engineering problem which will require using the thermal technology already developed for the Helios-probe. A Mariner class S/C (e.g., MVM-73) could reasonably be expected to survive and function to 0.4 AU, while a Pioneer (e.g., Pioneer-Venus, if built) could be modified to survive to ~0.7 AU.

5. The S/C approaches the comet at a small angle to the sun-comet line in the intercepts at 0.53 and 0.8 AU, but at a steep angle (60-90°) to the sun-comet line at 0.34 AU (Fig. 3). The small angle approach geometry has the advantage of traversing the coma and part of the tail with a single S/C, but imaging after closest approach is degraded since the S/C must look sunward to photograph the nucleus. In addition, separation of spatial-temporal variations will be difficult. The high angle approach geometry allows one to choose the phase angle at closest approach. Also, a 'fish-hook' trajectory is possible so that two bow-shock crossings can be made. In this event a second tail probe is desirable (launched on the same rocket as the coma probe) and will enable correlated simultaneous measurements on the coma and tail during the cometary encounter and in interplanetary space during the cruise mode.

6. The images of the nucleus (or nuclear region) will have highest resolution (~6 m, in 0° phase angle is chosen) and be most numerous (up to 240) for the 0.34 AU intercept. The best resolution will be ~55 m (phase angle = 90°) at 0.53 AU and ~150 pictures will be returned; at 0.80 AU (90° phase) the best resolution will be ~150 m and ~ 55 pictures will be returned. The number of pictures quoted here is twice the number which can be taken on the way in to encounter. It may not be possible to get all of the images after encounter in the 0.53 AU and 0.8 AU missions since the camera must slew toward the sun leading to increased scattered sunlight. However, it is the close approach imaging which is

44

of greatest value, consequently, loss of some pictures after closest approach is not too important. The expected imaging science is superior on the 0.34 AU mission.

7. An attitude stabilized (3-axis or de-spun) camera platform will be required if on-board navigation is deemed desirable. Terminal guidance is feasible on all three missions and would be needed to ensure the targeting accuracy needed to guarantee entry into the icy halo (say R_H ~1000 Km).

8. Measurements of neutral parent molecules are strongly dependent on the heliocentric distance at intercept because of varying cometary activity (as R^{-2}) and spacecraft flythrough velocity (as v^{-1}). On the other hand, the lifetime of molecules in the solar radiation field goes as R^2. A detailed model of the neutral mass spectrometer experiment shows that the science return is greatest by far at 0.34 AU and is roughly in the ratio (14/5/1) at (0.34/0.53/0.8 AU) respectively. If a mass spectrometer can be built which measures all mass peaks simultaneously or is dedicated to a single mass peak (100% duty cycle M.S.), then adequate data of major constitutents (H_2O) can be returned on all missions. However, adequate data on trace molecules (1% as abundant as H_2O) will be obtained only near perihelion and using on-board navigation. If a scanning mass spectrometer (say a duty cycle of 1%) is used, then even measurements of H_2O are only adequate with on-board navigation and at 0.34 AU. Trace molecules could not be measured with the latter instrument in any mission studied. It should be noted that the instrumental sensitivity used in this model could possibly be increased by 5-10 (A.O. Nier, private communication) with a consequent increased science return; and that the model assumes a stabilized platform for the neutral mass spectrometer experiment.

9. Various other desirable experiments have been briefly reviewed and it is thought that currently space-proven hardware would return adequate data on all missions but would be maximum at 0.34 AU.

6.0 RECOMMENDATIONS FOR FURTHER STUDY

1. Several experiment problem areas require further study and/or development work which should begin immediately to assure completion/ availability in time for the 1980 mission. They are:

    a. Charge-couple-devices and their applicability for use in spin-scan imaging systems.

b. Development of a 100% duty-cycle cometary neutral mass spectrometer.

c. A detailed study of the ion-mass spectrometer design problem for cometary flyby missions.

d. Long lead-time development of computer software and procedures for real-time iteration of the terminal navigation targeting problem.

e. Phase A studies should be carried out for the 0.34 and 0.53 AU intercept missions. The Phase A study of the 0.34 AU intercept should be carried out jointly with ESRO, if at all possible, since Helios thermal technology will be needed.

APPENDIX I

1980 ENCKE FAST-FLYBY
HELIOCENTRIC LAUNCH AND TRAJECTORY CHARACTERISTICS

APPENDIX I

1980 ENCKE FAST-FLYBY
HELIOCENTRIC LAUNCH AND TRAJECTORY CHARACTERISTICS

In this appendix, parametric information is presented on the characteristics of fast-flyby trajectories to comet Encke during the 1980 apparition. The appropriate launch period for such missions is near the time when Earth passes through the orbit plane of Encke on August 28, 1980. It is fortuitous that Encke's position in orbit at this time allows for a nearly minimum energy transfer to intercept Encke near perihelion.

Launch energy contours as a function of launch and arrival date for ballistic transfers during the 1980 apparition of Comet Encke are shown in Figure I-1. A range of launch dates near the Encke nodal crossing and a range of arrival dates both before and after Encke perihelion are shown. Launch and arrival dates are indicated in the Julian calendar for convenience, but conversion to the Gregorian calendar is easy by noting that the nodal crossing occurs on August 28, 1980 (Julian day 2444480) and Encke perihelion occurs at December 6, 1980 (Julian day 2444580). Various launch energy contours from 65 to 120 km^2/sec^2 are shown. Trajectories arriving before perihelion are generally Type I and those arriving after perihelion are Type II. Also indicated on the right-hand edge of the figure is the Encke-Sun distance in AU as a function of arrival date. The launch energy capability of a given launch vehicle depends upon the characteristics of that vehicle and the mass of the spacecraft being launched; however, it can be seen from Figure I-1 that arrival 15 days prior to perihelion requires a launch energy of about 74 km^2/sec^2 for a 10-day launch window. In general, launch energy increases as the encounter date moves nearer to perihelion.

Of additional concern is the launch declination of the Earth departure trajectories. This parameter affects range safety and Earth orbital coast time requirements. Contours of constant departure declination in the range of launch and arrival dates described above are shown in Figure I-2. Launches from KSC are generally limited by a launch azimuth of 180°. Higher azimuths are possible by expensive dog-leg maneuvers during ascent to orbit, but are generally not done. A launch azimuth of 108° implies a launch declination limit of 33° for in-plane launches. Higher declinations are possible by expensive plane-change maneuvers, but are also generally avoided. It can be seen from Figure I-2 that, except for a very small region near perihelion, the launch declinations are always below 30°; and hence, no problem exists for this mission.

An important encounter parameter is the relative velocity between the space-craft and the comet. Contours of constant arrival speed are shown in Figure I-3 for the same range of launch and arrival dates shown in Figure I-1. The relative velocities range from about 20 km/sec for arrivals 20 days prior to perihelion to about 8 km/sec for arrivals near perihelion. Pre-perihelion arrival dates have arrival velocities which are relatively constant across a 10-day launch window, while a considerable variation is noted for near-perihelion arrival dates. However, careful selection of arrival date/launch date combinations for near-perihelion arrival dates can provide a 10-day launch window with an approach velocity of about 8 km/sec.

An equally important trajectory parameter from the point of view of the science value of the mission is the direction relative to the Encke-Sun line from which the approach to Encke is made. Contours of constant approach phase angle (spacecraft-Encke-Sun angle) are shown over the launch/arrival date window as before in Figure I-4. It can be seen that arrivals at Encke about 10-20 days prior to perhelion result in an approach from nearly the direction of the Sun, that is, with low phase angle. The direction of encounter becomes more oblique for encounter dates near Encke perihelion. Encounters near perihelion are nearly at right angles to the Encke-Sun line; and hence, Encke's tail.

The combination of approach velocity and phase angle of the approach dictates the time spent by the spacecraft within the comet tail. Figure I-5 indicates this parameter of scientific interest. Contours of constant time spent within 20,000 km of the comet tail (the estimated size of the tail) are shown over the launch/arrival date window. The maximum time occurs for encounters about 16 days prior to perihelion. This maximum is about 10 hours. The time spent in the tail decreases to about 1 to 1.5 hours as the encounter date approaches Encke perihelion.
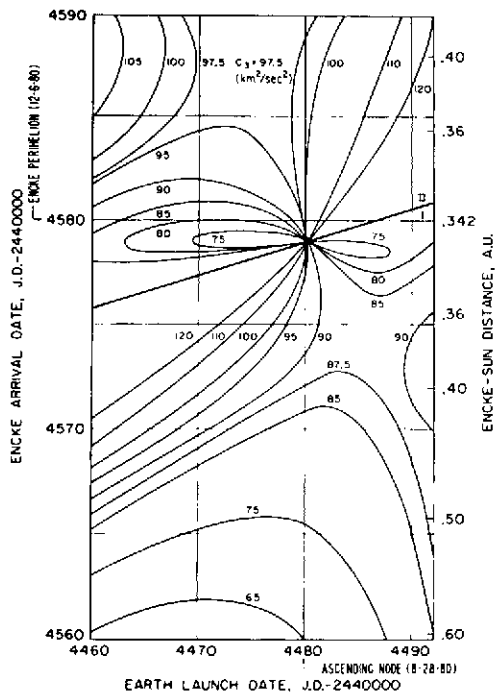
Figure I-1
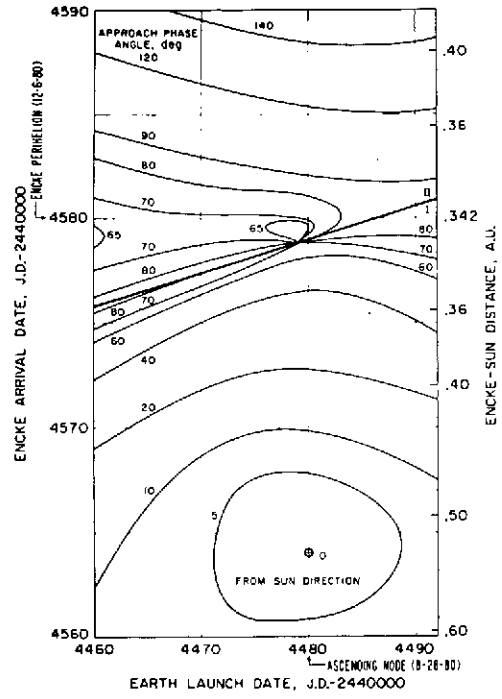
Figure I-2
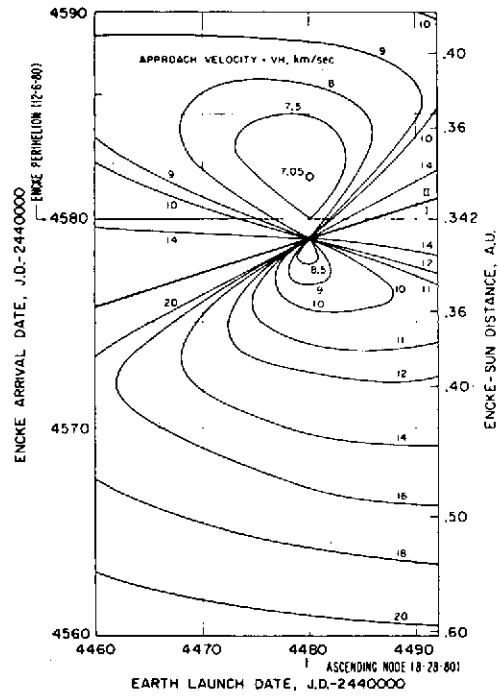
Figure I-3

I-3
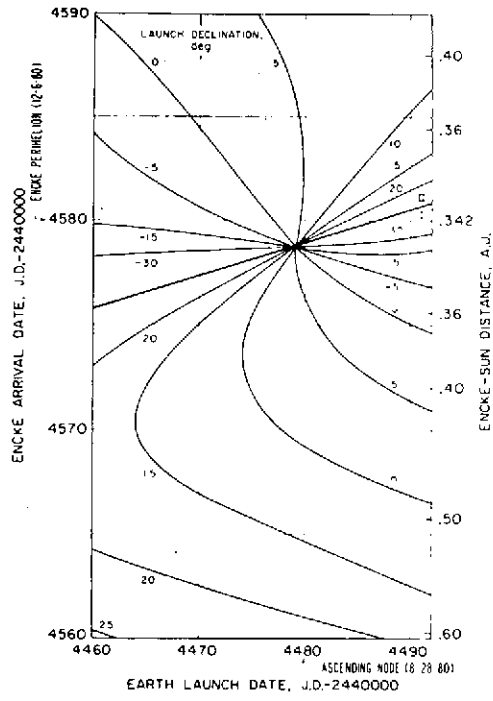
Figure I-4

Figure I-5

I-4
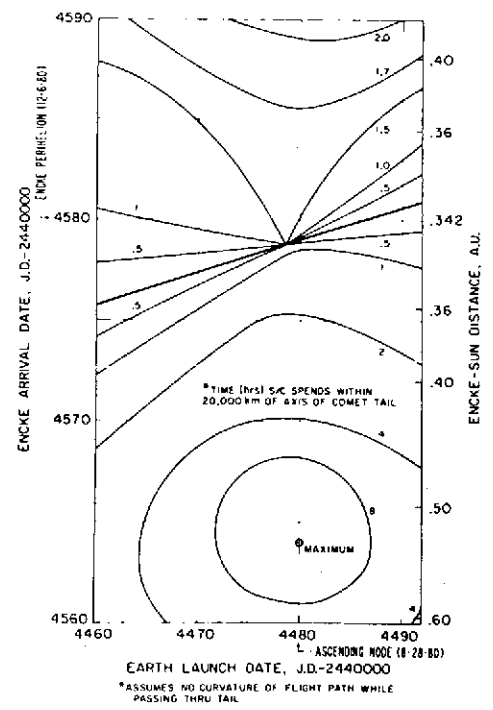
APPENDIX II

THE ALBEDO-AREA PRODUCT FOR THE NUCLEUS

OF COMET ENCKE

M. J. Mumma

Roemer has measured Encke's nuclear magnitude in 1963 and again in 1972 near aphelion. We have derived values of $pR^2\phi(\beta)$ from her nuclear magnitudes using the relationship

$$\log [pR^2\phi(\beta)] = 0.4(M_\odot - M_c) + 2 \log (r\Delta) \qquad \text{(II-1)}$$

where p = geometric albedo, $\phi(\beta)$ = phase law, $M_\odot$ = solar photographic magnitude (-26.41), and M_c = Encke's nuclear magnitude. Roemer's data and our calculated results are shown in Table II-1. By inspection of Figure II-1 one sees that $pR^2\phi(o)$ (i.e., the nuclear brightness) was greater by about three at aphelion in 1972 vs. 1963. Yet we know that the total brightness (at $r < 1.2$ AU) shows a slow secular decrease at about 0.05 - 0.1 mag/Rev, i.e., the 1974 total brightness was less than the 1964 brightness ($0.87 \rightarrow 0.75$, $r < 1.2$ AU). Dossin observed that Encke was unusually faint $\sim$30 days after perihelion passage in 1964. Thus the observational evidence show that the nucleus was unusually faint before perihelion (at large r), but the total gas production rate was normal until sometime after perihelion when it fell off more rapidly than usual.

The phase law can be derived from the data in Table II-1 by the following method. We want to cast the nuclear magnitude law in the form

$$M_c = M_0 + 5 \log r\Delta + a_1\beta \qquad \text{(II-2)}$$

From Equation II-1,

$$M_\odot = M_0 + 2.5 \log [pR^2], r = \Delta = 1, \beta = 0, \phi(o) = 1$$

$$\log [pR^2\phi(\beta)] = 0.4(M_0 + 2.5 \log (pR^2) - M_c) + 2 \log r\Delta$$

so

$$M_c = M_0 + 5 \log r\Delta - 2.5 \log \phi(\beta)$$

$$M_c = M_0 + 5 \log r\Delta + a_1\beta$$

or

$$a_1 = -2.5 \frac{\log [\phi(\beta)]}{\beta} \qquad \text{(II-3)}$$

Figure II-1 shows log $[pR^2\phi]$ vs. β. The value of $a_1 = +0.013\beta$ is determined from the 1963 data. Since $\phi(o) = 1$ by definition, the values pR^2 may be determined from the intercepts of the lines. They are $pR^2 = 0.22$ (1963), $pR^2 = 0.70$ (1972) and $pR^2 = 0.12$ (1973). The asteroidal phase law is shown for comparison. This is the law recommended by Marsden (IAUC 2547) and is the law adopted for the purpose of the main study.

Table II-1

Nuclear Brightness (M_2) and pR^2 for Encke's Comet

	r	Δ	β	M_2	log $[pR^2\phi(\beta)$	$pR^2\phi(\beta)$
9/24/63 Ref. 1	3.11	2.11	2.5	20.2	- 0.663	0.216
9/25/63	3.10	2.11	2.6	20.2	- 0.666	0.216
10/12/63	3.00	2.07	8.5	20.2	- 0.715	0.192
12/16/63	2.51	2.46	22.8	20.3	- 0.756	0.175
perihelion ~5/64						
8/30/64	1.65	1.08	36.4	19.0	- 1.316	0.048
8/15/72 Ref. 2	4.09	3.14	5.5	20.5	- 0.194	0.64
Aphelion ~9/3/64	4.10	3.09	0.8	N.B.R.*		
9/13/72	4.10	3.11	3.1	N.B.R.*		
9/21/73 (2586)	2.89	1.90	3.8	~20.5	~- 0.932	0.116

1. E. Roemer and R. E. Lloyd, Astronom. J. 71, 443 (1966).
2. E. Roemer, IAUC 2435
3. R. E. McCrosky and C. W. Shao, IAUC 2446
4. E. Roemer, IAUC 2446
5. E. Roemer, IAUC 2586
* Now being reduced
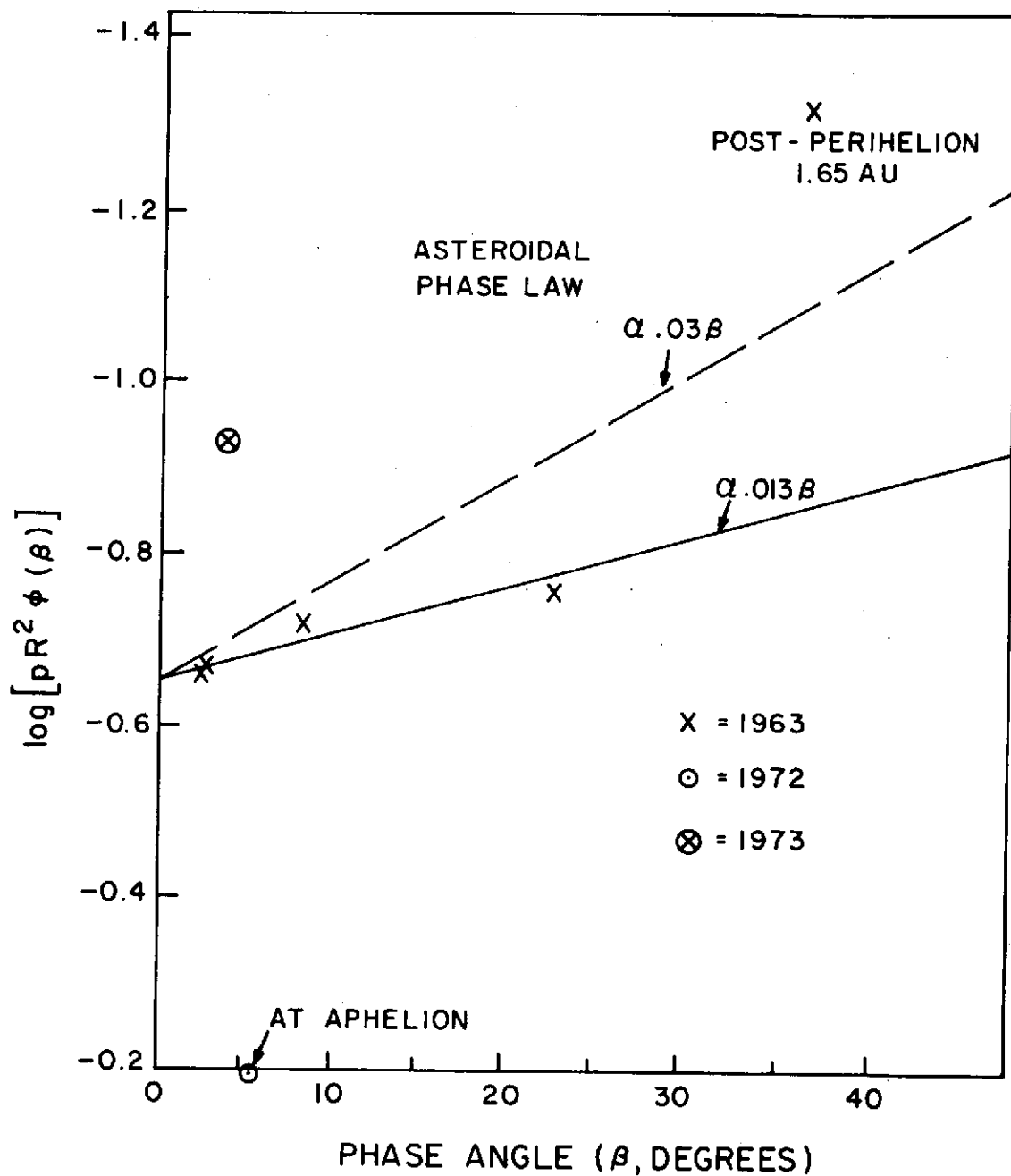
Figure II-1. Comet Encke: Nuclear Brightness vs. Phase Angle

APPENDIX III

OPTICAL IMAGE OF A COMETARY NUCLEUS:

1980 FLYBY OF COMET ENCKE

W. C. Wells
R. S. Benson
A. D. Anderson
G. Gal

August 1974

Contract NAS5-20566

Radiation Physics Laboratory
Palo Alto Research Laboratory
Lockheed Missiles and Space Company
Subsidiary of Lockheed Aircraft Corporation
Palo Alto, California 94304

APPENDIX III

OPTICAL IMAGE OF A COMETARY NUCLEUS:
1980 FLYBY OF COMET ENCKE

I   INTRODUCTION

This is a study of the feasibility of obtaining optical images of a cometary nucleus via a flyby of Comet Encke. This study is based on a physical model of the dust cloud surrounding the nucleus. Development of the model is based on available physical data and theoretical knowledge of cometary physics. Using this model, calculations are made of the absolute surface brightness of the dust in the line of sight of the on-board camera and the relative surface brightness of the dust compared to the nucleus. The brightness is calculated as a function of heliocentric distance and for different phase angles (sun–comet–spacecraft angle).

The study of the feasibility of obtaining optical images of the nucleus of Comet Encke via a flyby was divided into two parts. First a physical model of the dust cloud surrounding the nucleus was derived and then our Mie scattering code was employed to calculate the absolute brightness of the dust in the line of sight of the on-board camera. The surface brightness of the comet was compared to this background brightness along with contributions from debris and ice particles. Conclusions were then drawn in light of these results regarding the optimum imaging system for a flyby mission.

II   BACKGROUND OF FLYBY MISSIONS

At a symposium on the exploration of space held in Washington, D.C. in April 1959, Whipple (1959) pointed to the possibility of sending a space probe through the neighborhood of a comet. Two years later, Swings (1962) gave an extended survey on the scientific objectives and feasibility of such a mission at a symposium held in Pasadena, California in August 1961. He summarized the existing knowledge about comets and pointed to those problems in the physics of the comets for which investigations by means of space probes would be of special value.

There are quite a few problems which would be handled best with instruments installed in a cometary probe (Lust, 1969):

   a.   The structure and composition of the nucleus, its surface temperature and its color.

b. Chemical processes related to the formation of the observed radicals which take place in the vicinity of the nucleus where the density is high, and the ejection velocity of the different particles.

c. The composition of the cometary atmosphere, the mechanisms of dissociation and ionization, the size and nature of the dust grains.

d. The density gradient and partial densities of the different constituents in the coma and in the tail.

e. The interaction with the solar wind and with interplanetary magnetic fields, the structure of shock fronts and related problems of plasma physics and magneto-hydrodynamics.

Among the questions which have to be solved in the preparation of a cometary probe is which comet should be selected for a first space mission. Much work has been put into this problem by different groups in the U.S.A. and in Europe, and all these groups came to realize that the difficulties of such a mission are far greater than had first been anticipated. It is evident that a periodic comet which has been observed for many apparitions and whose orbit has been calculated with some accuracy is an easier target than a new comet which suddenly appears without being predicted and whose path has to be calculated from a few observations taken in small time intervals. But there are other reasons why a periodic comet can be reached more easily by a space vehicle than a new one. The orbits of almost all periodic comets have relatively small inclination to the ecliptic plane, and a motion in the same sense as Jupiter and all other planets (direct orbit). The inclinations of the orbital planes of the new comets are, on the other hand, randomly distributed between 0 and 180°, so that on the average these comets spend only a small fraction of their time close to the ecliptic plane while they are passing through the nodes. This causes a severe restriction for the launch window, while retrograde motions (inclination between 90° and 180°) cause very large approach velocities of the spacecraft with respect to the comet. Expensive terminal guidance would therefore be necessary to force the trajectory of the spacecraft into or near to the orbital plane of the new comet and to diminish the relative velocity to a slow flyby or to achieve a rendezvous.

Because of these difficulties, the new comets have been excluded as a first aim for a cometary probe by all groups who have investigated the feasibility of such a mission in spite of their high scientific interest.

Different groups in the U.S.A. as well as in Europe have carried out detailed feasibility studies during the last years. In 1961, a space mission to a comet was considered for the first time in NASA contracted studies of the Scientific and Technical Laboratories Inc. (Corben, 1962).

There exist about 50 periodic comets which have been observed during more than one perihelion passage, and an additional 30 comets with periods less than 20 years observed during one apparition only. About 5-7 of these comets appear on the average per year. A great amount of work and extensive calculations have been carried out by the different study groups to select among these comets the objects being fitted for a first mission. Several selection criteria had to be applied with respect to the following points:

a. The position of the comet at the time of intercept must be known with very high accuracy, and it became more and more clear that this condition is a major constraint for a cometary mission. It seems desirable that the probe should approach within 1000 km. If costly midcourse corrections are to be avoided, the position of the comet must be predictable at the time of launch, that is several months before intercept, with this accuracy.

To secure the necessary accuracy in the calculation of the orbital elements, it is necessary to start with a well-known orbit calculated from previous apparitions and to apply corrections by means of new observations made after recovery. Perturbations by planets, especially by Jupiter, can be the reason for considerable changes of the orbit. Also secular perturbations caused by a mass loss of the comet and non-gravitational forces play a role in this respect. Especially the location of the comet in its orbit, that is the daily motion, is affected by such perturbations. Since small errors in the daily motion will add up and result in large errors in the time of perihelion passage, the accuracy of this parameter is very important (Porter et al., 1965). It seemed, therefore, necessary to exclude all comets which had been observed during one apparition only, and also some of the remaining comets whose predicted orbits were not well enough established.

b. In order to guarantee observations of the comet's position necessary for orbit corrections, the comet should be recovered at least 2 months before launch, and it should be seen against a dark sky for several hours per night. This imposes the condition that the comet must be at least of 20th magnitude—the limit for recovery of an object whose position is known—several months before perihelion passage. The average brightness of periodic comets is so small that not many of them fulfill this condition.

The question of the accuracy of cometary orbits has been investigated by the groups in the U.S.A. as well as the European ESRO group. The conclusion is that if every effort is made to recover a comet very early,

that is about 20th magnitude, it should be possible to correct the predicted orbits to the accuracy necessary for a space mission for a number of comets.

c. The comet should be bright enough at intercept to get photometric data and good quality spectra from ground-based observatories to supplement the spacecraft data. This means that the comet should be of 12th magnitude or brighter at the time of perihelion passage, and it should be seen against a dark sky for some hours. Since a great percentage of the periodic comets never become so bright, and since some of the brighter ones are in unfavorable positions on the sky near perihelion (close to the sun), this is a further restriction of the number of feasible comets.

d. The ideal launch velocity should not exceed ~16 km/sec. This limit is chosen rather arbitrarily, it represents for instance the velocity required for a two year flight to Jupiter. It turned out, however, that this requirement does not impose a severe restriction, because almost every comet that was brighter than 12th magnitude at intercept fulfilled this condition.

e. Of two otherwise equal missions, that which leads to a smaller relative approach velocity between spacecraft and comet and therefore allows for a longer stay of the spacecraft in the vicinity of the comet should have priority.

f. All the points mentioned before refer more or less to the technical side of the mission. When choosing a comet, one should of course ask which mission promises the best scientific results. Comets are of very different activity according to their "age," that means according to the number of perihelion passages they have already made, because with every approach to the sun they lose a considerable amount of volatile material, and slowly get exhausted and inactive.

Summarizing the different points, a feasible comet should fulfill the following conditions:

1. A reliable predicted orbit should be available.

2. The comet should be of at least 20th magnitude 2 months before launch, and at that time be well observable for at least 2 hours per night.

3. It should be of at least 12th magnitude at intercept, and distinctly visible from the earth.

4. The launch velocity should not exceed ~16 km/sec.

5. The relative approach velocity between comet and spacecraft should be low.

6. The comet should be interesting from a scientific point of view.

A mission to Comet Encke in 1980 meets these requirements and should be undertaken.

III PHYSICAL PROPERTIES

With an estimate for the size of the nucleus of Comet Encke, and using the icy-conglomerate model, we estimate the distribution of non-volatile dust particles near the nucleus.

A. Nucleus

Although Whipple's (1950) model for comet nuclei is not universally accepted (e.g., Lyttleton, 1972), it has been used to successfully explain a number of cometary phenomena. Not the least of these is the non-gravitational force required to reproduce the orbital motion of Comet Encke and several other comets (Marsden and Sekanina, 1974 and earlier papers in this series). The non-gravitational acceleration derived by Marsden and Sekanina (1974) for Comet Encke shows a regular decrease which is consistent with the existence of a porous, rocky core, within which "dirty ice" is embedded (Sekanina, 1969b). Since the gravitational acceleration is proportional to the fractional rate of change of mass (as well as the degree of anisotropy of the ejection), it is necessary to estimate the mass of the nucleus in order to obtain the rate of mass loss itself. The mass (or mean density) and radius are also required in order to calculate the terminal velocities of ejected dust particles, since expanding vapor from the nucleus must lift the particles against gravitational attraction (Delsemme and Miller, 1971). Marsden and Sekanina (1971) estimate that Comet Encke loses 0.03 percent of its mass during each orbital revolution. A spherical nucleus of radius $R_n = 1.7$ km and mean density 1 g cm^{-3} has a mass $\sim 2 \times 10^{16}$g, implying $\Delta M \sim 6 \times 10^{12}$g per revolution; this mass loss is comparable to the estimates of Sekanina (1969a), which are $\sim 10^{13}$g. If the geometric albedo of the nucleus is $a_n = 0.1$, then $a_n R_n^2 = 0.3$ km^2 which is to be compared with observed values which range from 0.24 (Roemer, 1966) to $\gtrsim 0.82$ km^2, which we derive from Roemer's (1972) observation of the apparent magnitude of Comet Encke at aphelion ($m \simeq 20.5$). These lower limits result from our assumption that the comet was observed at opposition, thereby giving minimum earth-comet distance and phase angle. These results are consistent with the recent treatment of Delsemme and Rud (1973).

B.   Non-Volatile Particles

1.   Size Distribution

Lacking a determination of particle ejection for Comet Encke itself, we use the results of Finson and Probstein (1968) for Comet Arend-Roland and those of Sekanina and Miller (1973) for Comet Bennet. In particular, we use the distribution of particle sizes deduced by Finson and Probstein (1968), which they state is well-determined over the range $4 \leqslant \rho d \leqslant 40$ μm g cm^{-3}, where ρ is the bulk density of a particle of diameter d. We use the Sekanina and Miller (1973) distribution for the smallest particles (down to $\rho d = 0.9$ μm g cm^{-3}). Specifically, denoting by n(a) da the number of particles with radii in the range a to a+da,

$$n(a) = \begin{cases} K_1(a/a_0)^{-5} (a-1)/a_0 & 1 \leqslant a \leqslant 6.7 \ \mu m \\[2mm] K_2(a/a_0)^{-3} & 6.7 \leqslant a \leqslant 14.4 \ \mu m \\[2mm] K_3(a/a_0)^{-4} & 14.4 \leqslant a \leqslant 44.4 \ \mu m \\[2mm] K_4(a/a_0)^{-5} & a > 44.4 \ \mu m \end{cases}$$

The distribution for larger particles fits smoothly onto the distribution of interplanetary particles as given by Whipple (1968): $n \sim a^{-5}$. These are shown in Figure III-1. The constant $a_0 = 1$ μm, and the K's are determined by the requirement that

$$(4\pi\rho/3) \int_{a_0}^{\infty} a^3 n(a) da = 1 \ g$$

The rate of ejection of particles of radius a is then given by

$$P(a) = n(a) \frac{dM}{dt}$$

where dM/dt is the total mass-loss from the nucleus in the form of dust. We have

$$K_1 = 8.916 \times 10^{14}$$

$$K_2 = 1.137 \times 10^{14}$$

$$K_3 = 1.642 \times 10^{15}$$

$$K_4 = 7.298 \times 10^{16}$$
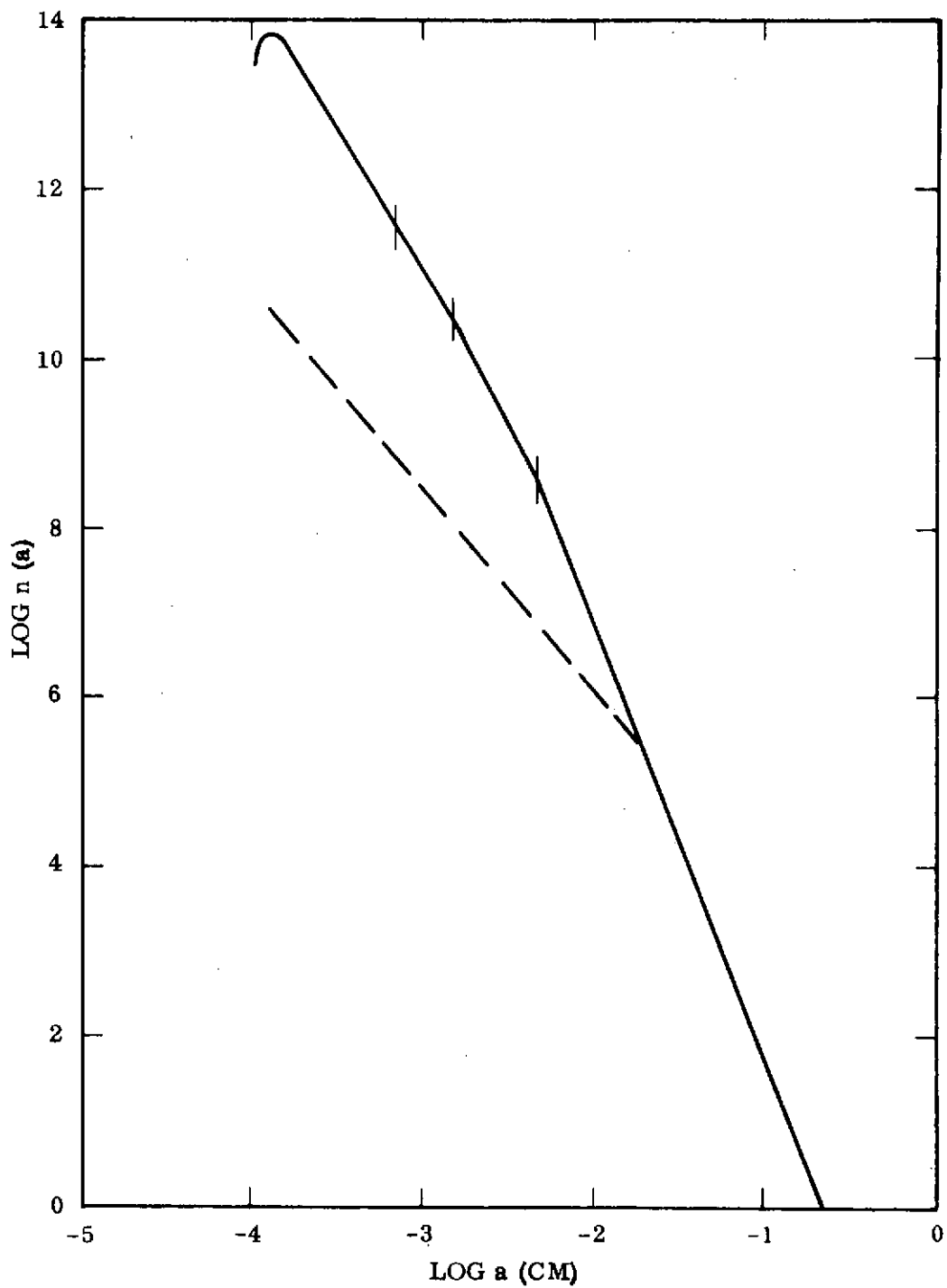
Figure III-1. Particle Size Distribution.

The particle mass density is assumed to be $\rho = 0.45\,\text{g cm}^{-3}$, which is approximately the value adopted by Whipple (1967, 1968) for meteroids of mass $m \gtrsim 10^{-6}$ g. Super-Schmidt data for the Taurid meteor shower give a mean value of about $0.28\,\text{g cm}^{-3}$ (Verniani, 1969). A somewhat higher density may be appropriate for the smaller particles: Whipple (1968) uses $\rho \simeq 1\,\text{g cm}^{-3}$ for $m \lesssim 10^{-6}$ g (a $\lesssim 175\,\mu\text{m}$), and radio data for sporadic and shower meteors give $\rho \simeq 0.8\,\text{g cm}^{-3}$ (Verniani, 1973). The particle distribution would not be greatly changed if we were to use $\rho \simeq 1\,\text{g cm}^{-3}$, except that n(a) would peak at a $\simeq 0.6\,\mu\text{m}$ and extend to about $0.55\,\mu\text{m}$. These small particles would make only a small contribution to the total scattered light.

It is of interest to compare our distribution to one derived by Taylor et al., (1973) in a similar manner. This is done in Figure III-2. The disparities arise from the different densities and size cutoffs used.

2. Production Rate

As discussed above, non-gravitational acceleration of Comet Encke implies a loss of $\sim 10^{13}$ g per orbital revolution. It is not known how much of this is in the form of dust, but Whipple (1967) suggests that the abundance of Taurid meteors is evidence that perhaps an old comet such as Encke releases a larger fraction of material in dust than does a "new" comet (see also Delsemme's 1973 review). Whipple (1967) goes on to estimate that, averaged over one period, Comet Encke contributes as much as 3.5×10^6 g sec^{-1} of meteoritic material to the interplanetary cloud. If true, this would imply a much smaller degree of anisotropy of ejection than has been determined for this comet (Marsden and Sekanina, 1971, p. 1143). The distribution of particle sizes might differ from that for "new" comets, having fewer small particles.

We conservatively assume that the total mass lost per orbit is 10^{13} g, of which 10 percent is dust. This gives a simple average mass-loss rate of $dM/dt \simeq 9.6 \times 10^3$ g sec^{-1} as dust. As an approximation to the evaporation rate of water snow (Delsemme and Miller, 1971; Marsden, Sekanina and Yeomans, 1973), the mass-loss varies as r^{-2} for $r \leqslant r_c$ amd is zero at greater distances. The mass-loss rate at any particular heliocentric distance is then easily calculated; Table III-1 gives the mass-loss at $r = 0.8\,\text{AU}$ for various assumed r_c.

Thus, for this simple approximation, the mass-loss rate is not sensitive to the value of r_c, and $dM/dt \simeq 5 \times 10^4$ g sec^{-1} is a typical value for $r = 0.8\,\text{AU}$.

3. Velocity Distribution

The evaporation of cometary ices (primarily H_2O) produces a flow from the nucleus which accelerates dust particles to their terminal ejection velocities
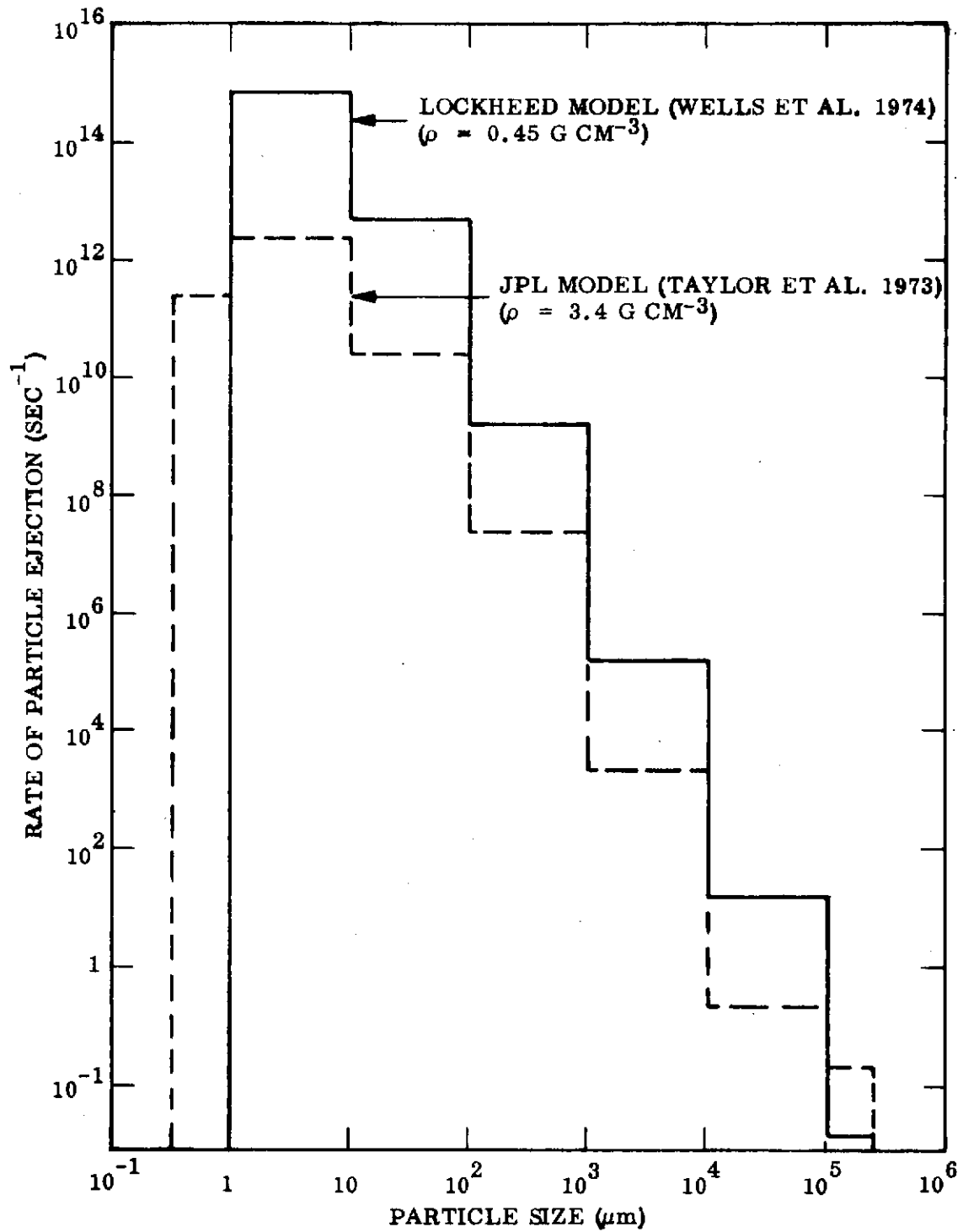
Figure III-2. Comparison of Distribution of Particle Sizes

Table III-1

Dust Mass-Loss at 0.8 AU

r_c (AU)	dM/dt (10^4 g sec^{-1})
1.00	5.93
1.25	5.47
1.50	5.17
2.00	4.78
2.808	4.42

within ~10 nuclear radii (Probstein, 1968; Delsemme and Miller, (1971). Delsemme and Miller (1971) calculate the largest particle which the expanding vapor can lift against gravity; for ρ = 0.45 g cm^{-3}, R_n = 1.7 km and ρ_n = 1 g cm^{-3} we have

$$a_{max} \simeq 3.14 \times 10^{-17} \, Z \text{ cm}$$

where the rate of evaporation, Z (molecule cm^{-2} sec^{-1}), depends on heliocentric distance. In Figure III-3 we show the velocity distribution from Delsemme and Miller (1971) expressed in terms of a/a_{max}. Using the evaporation rate as reported by Marsden, Sekanina and Yeomans (1973), at 0.8 AU Z $\simeq$ 4.9 x 10^{17} and $a_{max} \simeq$ 15.5 cm. Since Z varies roughly as r^{-2}, larger particles can be ejected at r < 0.8 AU. Also, as can be seen in Figure 3, at smaller heliocentric distances all particles tend to have nearly the same terminal velocity, while at larger distances v $\sim a^{-1/2}$ (approximately). If, as is likely, Comet Encke is not covered with ices, then the effective Z(r) should be reduced, thereby also reducing a_{max} and v(a).

For calculating sunlight scattering from dust, we divide the particle size distribution into six ranges and assign appropriate mean radii to each range. The root-mean-square, $(\langle a^2 \rangle)^{1/2}$, is used to calculate the scattering by each size range. While $(\langle a^{1/2} \rangle)^2$ is used for determining the terminal velocity, the result is not sensitive to the particular kind of averaging which is used because the velocity is a slowly-varying function of particle radius. The size ranges and derived properties are given in Table III-2, with dM/dt = 5 x 10^4 g sec^{-1} and a_{max} = 15.5 cm as is appropriate for a heliocentric distance of 0.8 AU.
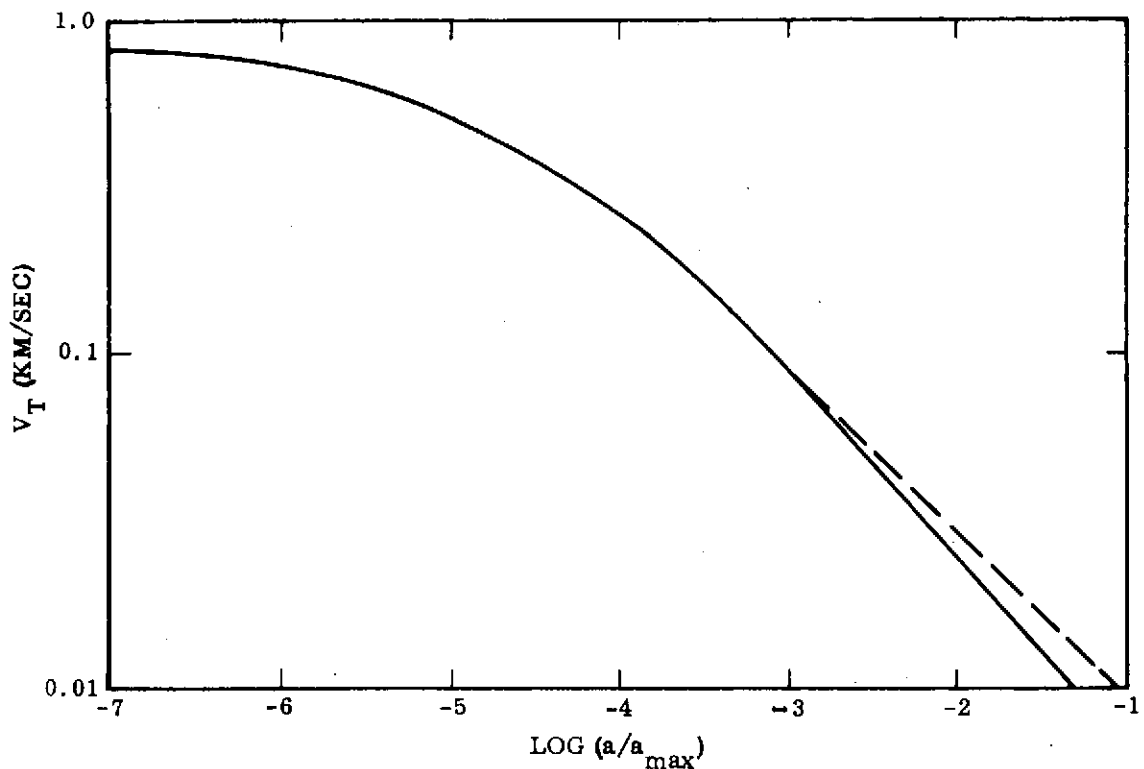
Figure III-3. Terminal Velocities of Non-Volatile Particles

The first five size ranges used in the Mie scattering code are discussed below; the final group contains particles sufficiently large that the geometrical approximation is adequate ("debris"). The scattering contribution (column 4) represents the relative total geometric cross section of each size range.

Because the particles attain their terminal velocities very near the cometary nucleus, throughout the coma (where they will be observed) their spatial distribution is given by

$$n_i(R) = \frac{P_i}{4\pi R^2 v_i} \ cm^{-3}$$

where P_i is the production rate and v_i the terminal velocity for particles in the ith size range; R is the radial distance from the nucleus.

This model shares with all current theoretical models the lack of asymmetry in ejection which must be present in order to produce the observed non-gravitational forces. The size distribution of dust particles has the virtue of being related to

Table III-2

Particle Sizes and Terminal Velocities (0.8 AU)

Range (μ m)	Production Rate (sec^{-1})	$(<a^2>)^{1/2}$ (μm)	Geometric Scattering Contribution (%)	v (km sec^{-1})
1 - 1.5	1.51×10^{14}	1.28	9.8	0.53
1.5 - 3	1.79×10^{14}	2.04	29.4	0.49
3 - 6.7	3.68×10^{13}	4.10	24.5	0.41
6.7 - 14.4	5.03×10^{12}	9.35	17.4	0.33
14.4-44.4	8.77×10^{11}	20.9	15.2	0.25
44.4-a_{max}	2.34×10^{10}	62.9	3.65	0.15

observations of actual comets, although there has been no analysis of an old comet (such as Encke) using the procedures described by Finson and Probstein (1968). Perhaps the lower curve in Figure III-1, giving Whipple's (1968) distribution of interplanetary particles, would be a better representation for Comet Encke or the compilation by Dohnanyi (1972). The distribution used here contains a larger fraction of small particles ($1 < a < 5 \mu$m) which are relatively efficient scatterers, so our results may represent an upper limit to the sunlight scattering for a given dM/dt.

IV. TRAJECTORY

Comet Encke is a periodic comet with a period of 3.3 years. It shows greatly reduced activity after perihelion relative to before, and shows very little continuum radiation at any time, indicating a low dust content (Taylor et al., 1973). Encke never shows a type II (dust) tail and in some apparitions has shown no tail at all. The observations from 1885-1951 indicates that Encke's coma becomes observable at about 1.5 AU at the same time as the first appearance of its tail (Vsekhsvyatskii, 1964). The orbital characteristics of comet Encke are given in Table III-3.

Vsekhsvyatskii (1964) has estimated a nominal value of 10^5 km for the diameter of Encke's coma reduced to a Sun-comet distance of 1 AU. Observational data on tail length are given by Yoemans (1973) and TRW (1972).

Table III-3

Orbital Elements of Comet Encke

Orbital period (year)	3.30
Aphelion distance (AU)	4.09
Perihelion distance (AU)	0.34
Orbital inclination (deg)	12.4
Velocity at 1 AU (km s^{-1})	37.1
Velocity at perihelion (km s^{-1})	69.9
Orbital eccentricity	0.847

Many different kinds of missions to Encke have been proposed including fast and slow flybys. They do have certain elements in common. A nominal miss distance is about 10^2 -10^3 km. One proposed probe trajectory calls for a rendevous at a heliocentric distance of about R_s = 0.8 AU. We have chosen this distance to calculate the absolute and relative luminosities of the dust, debris, and nucleus.

V. MIE SCATTERING

In this section the computer code used to calculate the Mie scattering of sunlight from the cometary dust is described. Results are then presented for scattering of dust particles in the coma of Comet Encke.

A. Mie Theory and Computer Code

Particulate radiation effects in particulate clouds can be calculated provided that the optical constant of the radiating particles are known. Gal and Kirch (1973 and Gal, 1974) reported a new computer code called GMIE to calculate scattering cross sections of interest. Calculations are based on MIE theory for a specified particulate column with a given complex index for refraction, range of wavelength, temperature, and particle sizes.

It should be noted that the GMIE code can be used to obtain scattering cross sections or differential cross section for any given spherical particle or particulate column with a given size distribution and index of refraction.

1. Electromagnetic Radiation Scattered by Absorbing Sphere

The passage of electromagnetic radiation through a particle cloud is generally accompanied by removal of a fraction of the energy from the incident beam. This fraction may be partly absorbed within the particles and partly scattered — i.e., reappear in the same direction as well as in other directions. The characteristics of the scattered radiation are determined by the wavelength λ of the incident radiation, the refractive index ($m = n_1 - in_2$) of the particles and size as well as the shape of the discrete particles in the medium. For the radiation studies, we assume spherical particles with radius r.

The interaction of an electromagnetic wave with an absorbing sphere is described by the MIE theory (Fig. III-4) and is discussed in detail elsewhere (van de Hulst, 1957). Classical MIE theory gives the intensity $I(W/cm^2)$ at a distance R and angle θ of the radiation scattered from a single spherical particle of radius r exposed to parallel monochromatic radiation of intensity I_0:

$$\frac{I}{I_0} = \frac{S(\theta)}{2(2\pi/\lambda)^2 R^2} \qquad \text{(III-1)}$$

where $S(\theta)$ is the scattering function per unit particle.

A computational scheme and computer code were provided by J. Dave of IBM (1968). These are based on the Ricatti-Bessel functions and give the MIE scattering cross section of absorbing spherical particles.

Computations are valid for all values of size parameters that occur in the theory regardless of whether they are large or small. The index of refraction of the particles are given in terms of their real and imaginary parts.
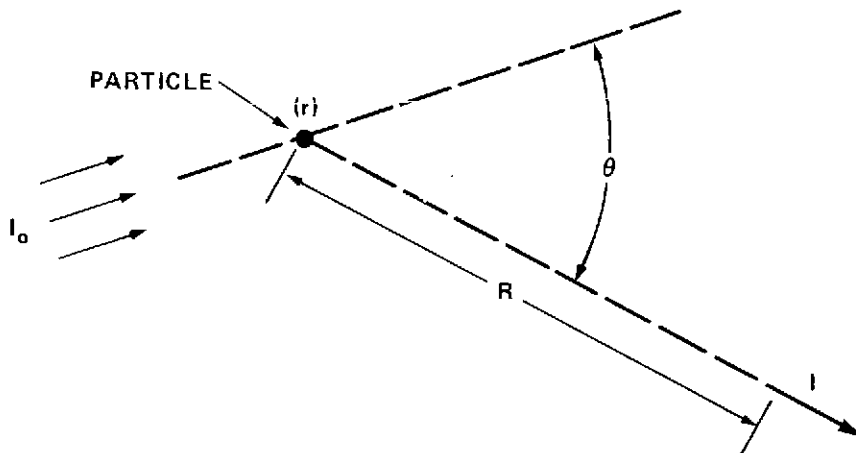
Figure III-4. Definition of Single-Particle Scattering

The extinction and scattering cross section are calculated from various combinations of the sum and products of the coefficients a_n and b_n. The usual expressions for a_n and b_n are:

$$a_n = \frac{\psi_n'(y)\,\psi_n(x) - m\,\psi_n(y)\,\psi_n'(x)}{\psi_n'(y)\,\xi_n(x) - m\,\psi_n(y)\,\xi_n'(x)} \qquad \text{(III-2)}$$

$$b_n = \frac{m\,\psi_n'(y)\,\psi_n(x) - \psi_n(y)\,\psi_n'(x)}{m\,\psi_n'(y)\,\xi_n(x) - \psi_n(y)\,\xi_n'(x)} \qquad \text{(III-3)}$$

where

m = the complex index of refraction

n = a positive integer

ψ and ξ = the Ricatti-Bessel functions defined by

$$\psi_n(z) = \left(\frac{1}{2}\,\pi z\right)^{1/2} J_{n+1/2}(z) \qquad \text{(III-4)}$$

$$\xi(z) = \left(\frac{1}{2}\,\pi z\right) H^{(2)}_{n+1/2}(z) \qquad \text{(III-5)}$$

with $J_{n+1/2}$ and $H^{(2)}_{n+1/2}$ the Bessel functions of first and third types. The prime denotes differentiation with respect to the argument of the function and

$$x = 2\pi r/\lambda \qquad \text{(III-6)}$$

$$y = mx \qquad \text{(III-7)}$$

where r is the particle radius and λ is the wavelength.

Once these scattering coefficients are defined, then extinction and scattering normalized cross section can be calculated with the following equations:

$$Q_{EXT} = \frac{2}{x^2} \sum_{n=1}^{\infty} (2n+1)\,\text{Real}\,(a_n + b_n)$$

$$\text{(III-8)}$$

$$Q_{SCATT} = \frac{2}{x^2} \sum_{n=1}^{\infty} (2n+1)\,(|a_n|^2 + |b_n|^2)$$

Scattering efficiency (i.e., normalized scattering cross section) given by Equation (III-9) can also be written as a function of scattering angle and the intensity in that direction:

$$Q_{SCATT} = \frac{1}{x^2} \int_0^\pi [i_1(\theta) + i_2(\theta)] \sin \theta \, d\theta \qquad \text{(III-10)}$$

where

$$i_1(\theta) = |S_1(\theta)|^2$$

$$i_2(\theta) = |S_2(\theta)|^2$$

and

$$i_1(\theta) + i_2(\theta) = S(\theta) \qquad \text{(III-11)}$$

$i_1(\theta)$ and $i_2(\theta)$ refer respectively, to the intensity of light polarized perpendicularly and parallel to the plane through the direction of propagation of the incident and scattered beam. These intensities are given in terms of the complex amplitude functions $S_1(\theta)$ and $S_2(\theta)$:

$$S_1(\theta) = \sum_{n=1}^{\infty} \frac{2n+1}{n(n+1)} [a_n \pi_n(\cos \theta) + b_n \tau_n(\cos \theta)] \qquad \text{(III-12)}$$

and

$$S_2(\theta) = \sum_{n=1}^{\infty} \frac{2n+1}{n(n+1)} [b_n \pi_n(\cos \theta) + a_n \tau_n(\cos \theta)] \qquad \text{(III-13)}$$

The phase functions π_n and τ_n appearing in Equations (III-12) and (III-13) can be expressed in terms of the Legendre polynomials, P_n, as follows:

$$\pi_n(\cos \theta) = \frac{dP_n(\cos \theta)}{d \cos \theta}$$

$$\tau_n(\cos \theta) = \cos \theta \, \pi_n(\cos \theta) - \sin^2 \theta \, \frac{d\pi_n(\cos \theta)}{d \cos \theta}$$

$$\text{(III-14)}$$

The detailed computational method to obtain these Legendre polynomials with recurrence relationships is discussed elsewhere (Dave, 1968).

If there is no absorption, i.e., $n_2 = 0$, then $Q_{EXT} = Q_{SCATT}$. Otherwise, Q_{ABS}, the efficiency factor for absorption, is given by

$$Q_{ABS} = Q_{EXT} - Q_{SCATT} \qquad \text{(III-15)}$$

Equation (III-9) or (III-10) gives the total scattered intensity. On the other hand, one may need to know the fraction of energy scattered into the forward and backward directions. This is obtained in terms of normalized cross section given in Equations (III-16) and (III-17), respectively

$$Q_{TRANS} = \frac{1}{x^2} \int_0^{\pi/2} [i_1(\theta) + i_2(\theta)] \sin \theta \, d\theta \qquad \text{(III-16)}$$

and

$$Q_{REF} = \frac{1}{x^2} \int_{\pi/2}^{\pi} [i_1(\theta) + i_2(\theta)] \sin \theta \, d\theta \qquad \text{(III-17)}$$

2. Solar Scattering Cross Section for a Spherical Particle

With the help of the basic MIE scattering theory, particular scattering due to sunshine will be treated through an equivalent normalized differential solar-scattering cross section. The sun is approximately half a degree as observed from the earth, and calculations similar to those derived by Gal and Kirch (1973) for earthshine scattering would require evaluation of scattering function $S(\theta)$ for smaller than 1 deg, which is our present minimum step size. Approximate differential cross section will be obtained by averaging the basic MIE scattering function over a small angular increment ($\Delta\theta$) to account for the finite solar disk (Fig. III-5).
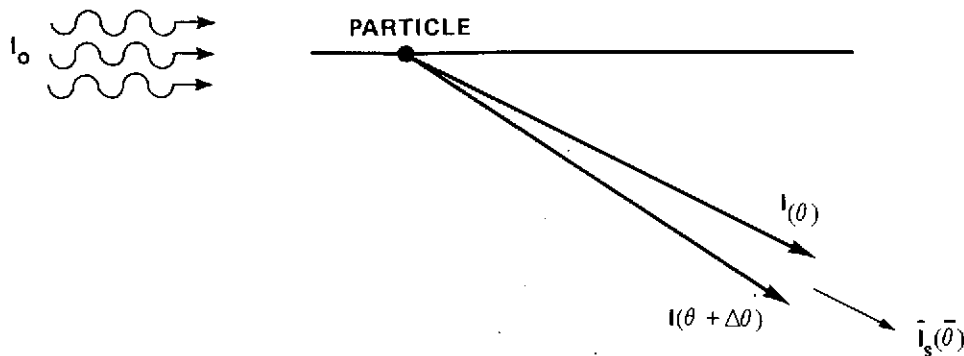
Figure III-5. Solar Scattering Model

From Equation (III-1)

$$\frac{(I_S R^2)}{I_0} = \frac{1}{2\left(\frac{2\pi}{\lambda}\right)^2} \overline{S}(\theta) \qquad \text{(III-18)}$$

The normalized differential cross section can be obtained by dividing Equation (III-18) with the geometrical cross section $G = r^2 \pi$

$$(dQ) = \left(\frac{I_S R^2}{\pi r^2 I_0}\right) = \frac{1}{2\pi\left(\frac{2\pi r}{\lambda}\right)^2} \overline{S}(\theta) \quad (sr^{-1}) \qquad \text{(III-19)}$$

Equation (III-19) yields the normalized scattering cross section for a single spherical particle.

3. Column Average Cross Section and Radiance

a. Column Scattering — The extension to the case of scattering from a column of particles is straight-forward upon adopting restrictive assumptions. First, the distance R must be large compared to the column dimensions so that scattering angle is essentially constant for a given I_0 direction. Also, the column must be optically thin. This requirement means that: (1) each particle is exposed to the incident intensity I_0, regardless of location; and (2) the radiation scattered from one particle does not interact with others as it passes from the column; i.e., there is no multiple scattering.

These assumptions allow the scattered intensities to be added. With the help of Equation (III-19) we can define a cloud averaged differential cross section, $\overline{\sigma}$.

$$\overline{\sigma} = \sum_i (dQ)_i \, r_i^2 \, \pi(N_i/N_t) \, (\mu m^2 \, sr^{-1}) \qquad \text{(III-20)}$$

where

N_t = the total number of particles

N_i = the number i^{th} particles

r_i = the radius of the ith particle

b. Column Radiance — Figure III-6 shows the geometry; the solid angle of the instrument is given by $\Omega = A/L$, and the scattering cloud volume is $V = A\ell$, where A is the column surface area, and ℓ is the depth of the column. The total number of particles in the scattering values is $N_t = nA\ell$, where n is the particle
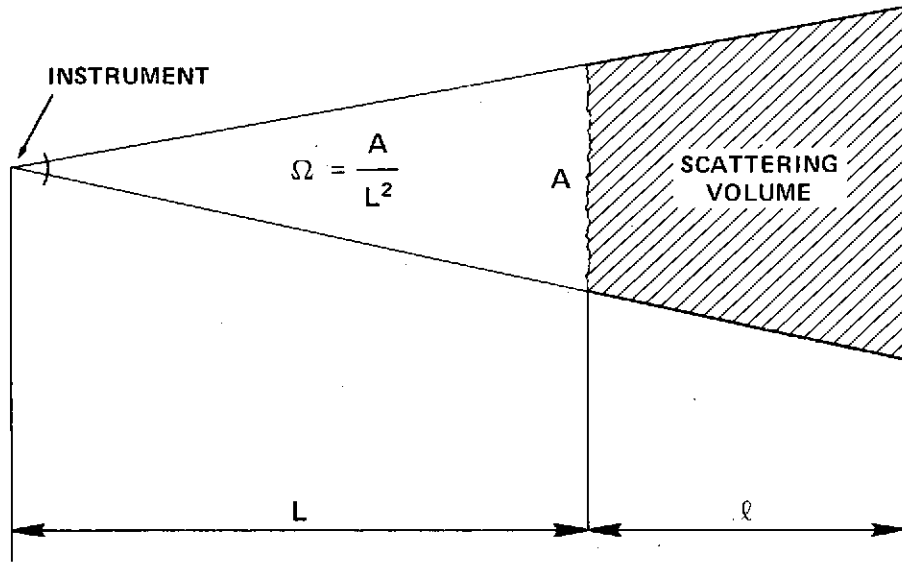
Figure III-6. Definition of Scattering Values

density. The incident intensity $I_{o\lambda}$ (watt/cm^2 · μ) can be calculated assuming the sun as a blackbody at a temperature T_{sun} = 6000 K, and sun is approximately half a degree as observed from the earth

$$I_{o\lambda} = B_\lambda(T = 6000) \; (\Delta\alpha) \; (\text{W cm}^{-2} \, \mu\text{m}^{-1}) \qquad \text{(III-21)}$$

where

$$B_\lambda = \frac{1.19 \; 10^4 (1/\lambda)^5}{\exp\left(\dfrac{1.4384 \times 10^4}{\lambda \, T_s}\right) - 1} \; (\text{W cm}^{-2} \, \text{sr}^{-1} \, \mu\text{m}^{-1}) \qquad \text{(III-22)}$$

where λ is the wavelength in microns, and $(\Delta\alpha)$ is solid angle of the sun viewed from the column (6.8 10^{-5} sr) at 1 AU.

The column radiance is defined as

$$N_\lambda = \frac{J_\lambda}{A} \; (\text{W cm}^{-2} \, \text{sr}^{-1} \, \mu\text{m}^{-1}) \qquad \text{(III-23)}$$

Substituting Equations (III-19) through (III-22) into Equation (III-23), we obtain

$$N_\lambda = B_\lambda n_T \, l(\Delta\alpha) \sum_{i=1}^{5} (dQ)_i \, r_i^2 \pi \; (N_i/N_t) \; (\text{W cm}^{-2} \, \text{sr}^{-1} \, \mu\text{m}^{-1}) \qquad \text{(III-24)}$$

Equation (III-24) has been programmed into our GMIE code; additional inputs required are particle size, its distribution, and the column depth, ℓ.

B. Mie Scattering From Cometary Dust Particles

We have inputed the comet Encke dust distribution into the GMIE code for various indices of refraction. The normalized scattering and absorption cross sections given in Equations (III-10) and (III-15) are plotted in Figure III-7 for an index of refraction of 1.7-0.05i. Figure III-8 shows a plot of the scattering function as a function of scattering angle for a dielectric particle of 0.65 μm radius with an index of refraction n = 1.7-0.05i. More plots of particle scattering functions are found in Appendix I showing the effect of particle sizes and indices of refraction. Also, the angular dependence of the polarization is plotted for a few select cases. To calculate the scattered sunlight from the comet, we chose an index of refraction of 1.7-0.05i to represent cometary dust particles which are probably primarily silicates containing metallic elements (Wickramasinghe and Krishna Swamy, 1968). Column densities are calculated in Appendix II. The results of the Mie scattering calculations are presented in Table III-4 where the wavelength dependence of the scattered radiance N_λ from Equation (III-23) is presented as a function of the Sun-Comet-Probe angle. The functional dependence on wavelength and angle of the average differential cross section $\bar{\sigma}$ from Equation (III-20) is displayed graphically in Figures III-9 and III-10 for a few selected cases. Figure III-9 shows the effect of view angle on $\bar{\sigma}$ at $\lambda = 0.5\mu$m. The minimum scattering at this wavelength can be seen to occur in the 0-90° region. The wavelength dependence of the scattered radiance is displayed in Figure III-10 for several view angles. It would appear that the scattering in the 0-90° range is relatively insensitive to wavelength dependence.

These results, which have been calculated for a heliocentric distance of R_s = 0.8 AU, can be approximately scaled to other distances by the law

$$N_\lambda(R_s) = N_\lambda(0.8) \left(\frac{0.8}{R_s}\right)^{4-\zeta} \tag{III-25}$$

where ζ accounts for the terminal velocity dependence on heliocentric distance and R_s is in AU. Equation (III-25) reflects the inverse square dependencies of the solar irradiance and dust production rates. The heliocentric dependence of the terminal velocities arises primarily in the case of Encke from the fact that the acceleration of the dust particles is dependent on the number of collisions the particles undergo with effusing gas molecules. Hence, the terminal velocities depend on particle sizes and the vaporization rate of gas from the nucleus. In the case of Encke dependence on the temperature of the nucleus is of lesser importance. For the particle sizes of importance here the heliocentric dependence can be approximated by setting ζ - 0.4. This law will hold for R_s out to about 1.5 AU where the dust production ceases due to the threshold effect of ice evaporation.
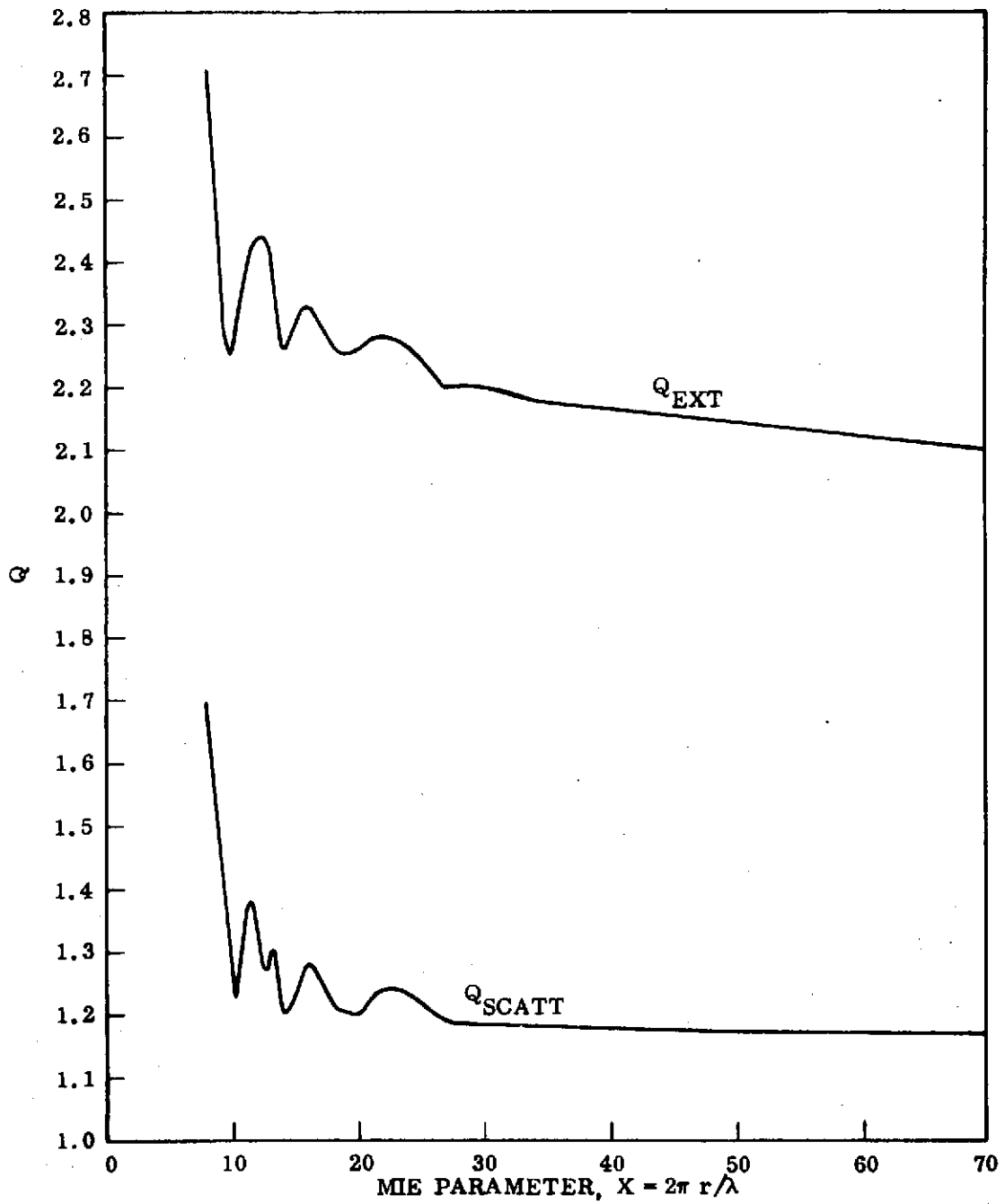
Figure III-7. Scattering Efficiency vs. Mie Parameter for n = 1.7-0.05i
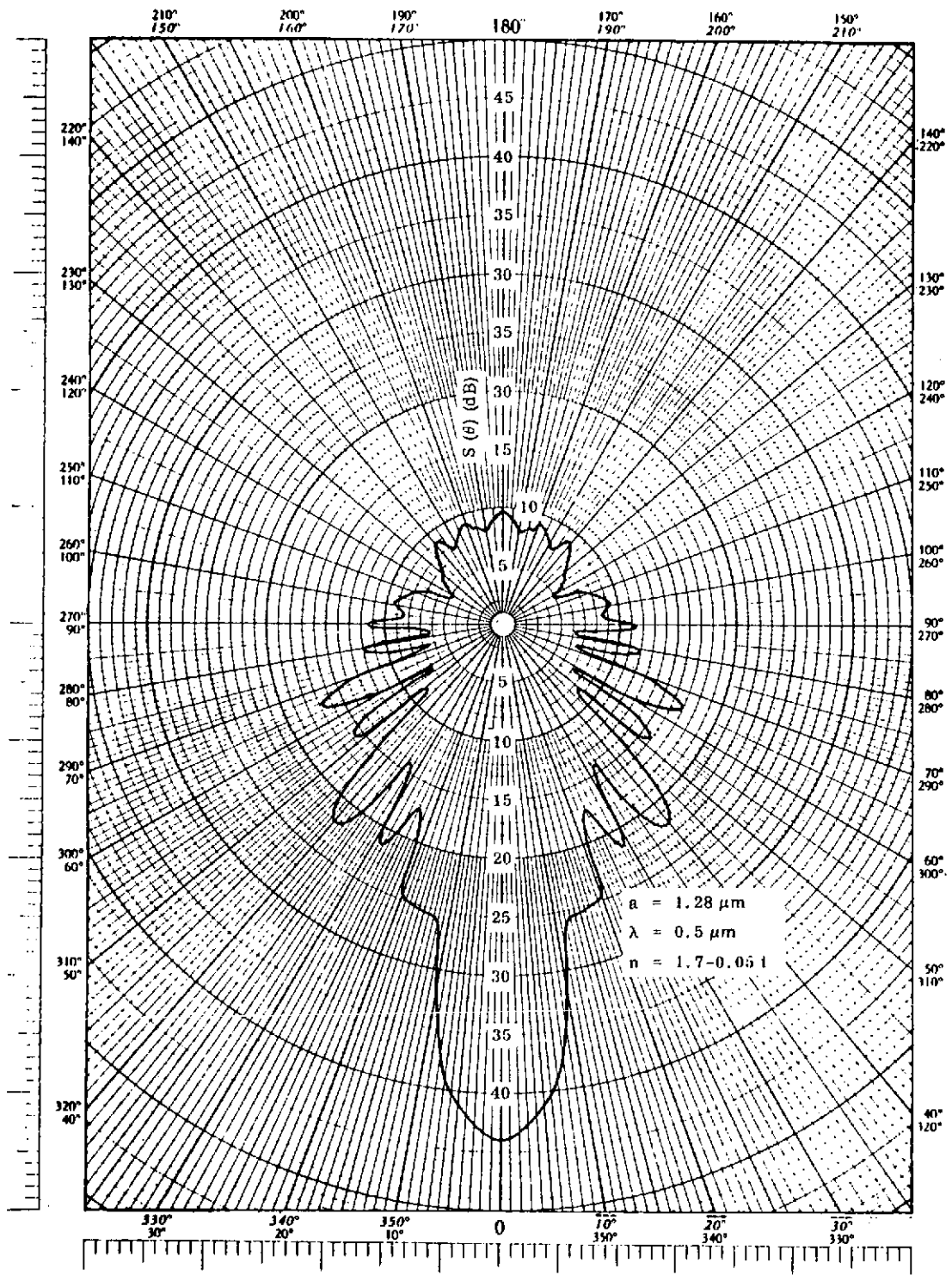
Figure III-8.   Angular Dependence of Scattering Functions, a = 1.28 μm,
n = 1.7-0.05 i
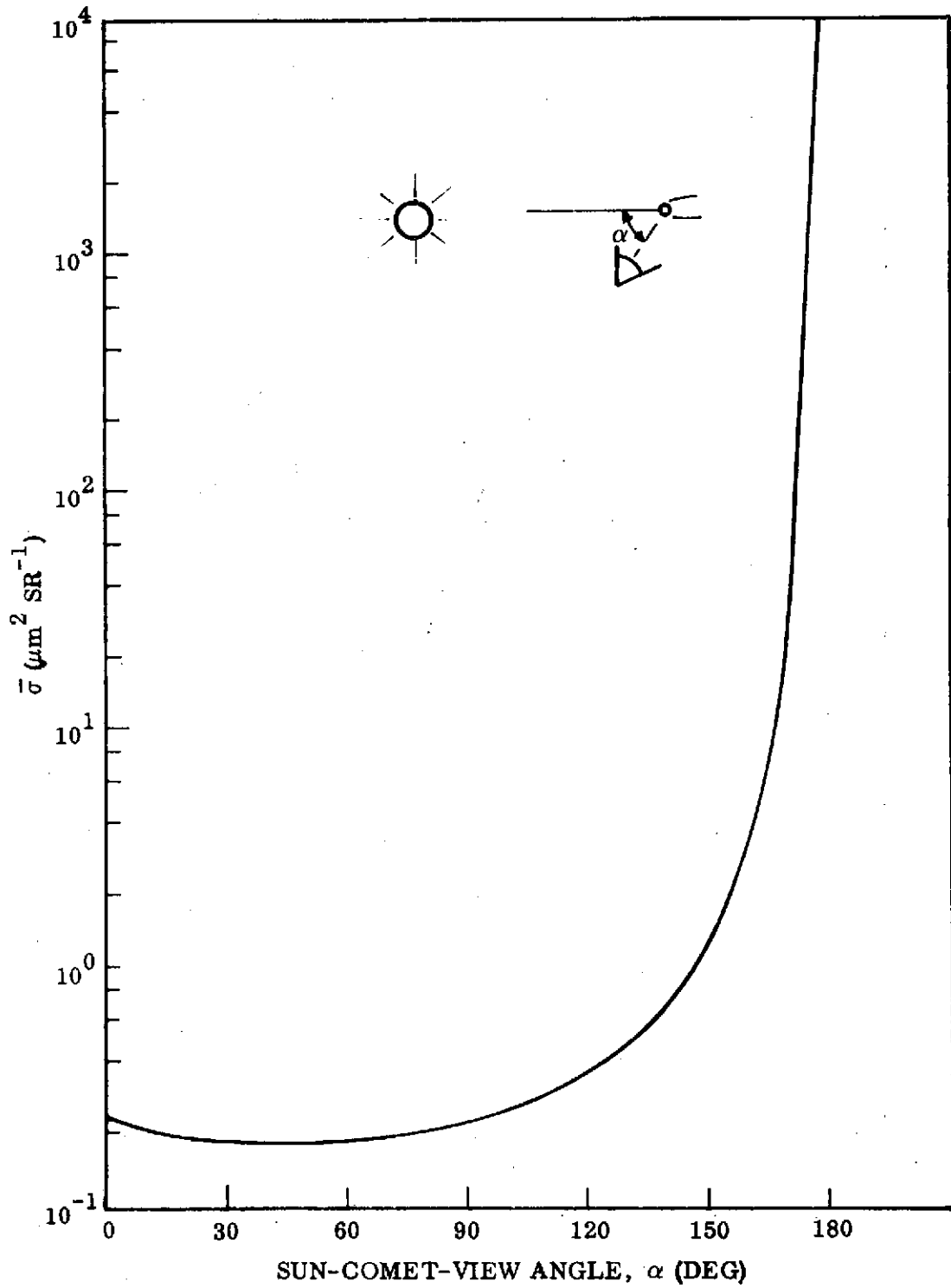
Figure III-9. Angular Dependence of Average Scattering Cross Section,
$\lambda = 0.5 \ \mu m$
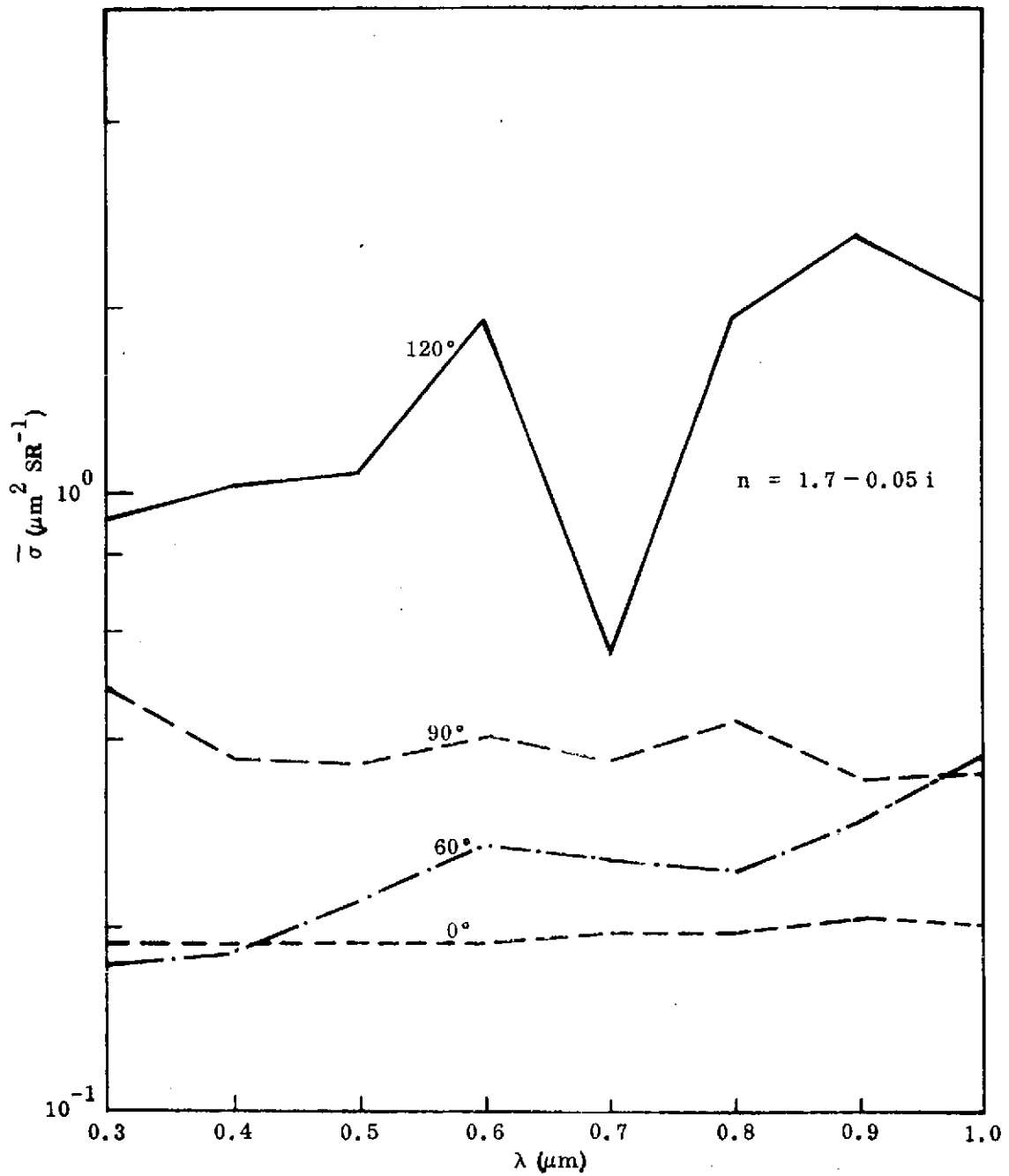
Figure III-10. Wavelength Dependence of Average Scattering Cross Section

Table III-4

Radiance of Comet Dust at $R_s = 0.8$ AU

N_λ(w cm^{-2} sr^{-1} μm^{-1})

	Sun–Comet–Probe Angle						
	0°	30°	60°	90°	120°	150°	180°
0.3	2.7(-6)	2.4(-6)	2.3(-6)	2.2(-6)	6.2(-6)	1.2(-5)	1.4
0.4	4.8(-6)	4.2(-6)	4.1(-6)	4.1(-6)	8.3(-6)	2.3(-5)	1.5
λ 0.5	5.4(-6)	4.6(-6)	4.4(-6)	5.4(-6)	8.9(-6)	2.6(-5)	1.1
(μm) 0.6	5.0(-6)	4.1(-6)	4.1(-6)	6.0(-6)	9.0(-6)	4.2(-5)	6.8(-1)
0.7	4.3(-6)	3.5(-6)	3.3(-6)	4.7(-6)	6.8(-6)	9.9(-6)	4.2(-1)
0.8	3.7(-6)	2.9(-6)	2.5(-6)	3.6(-6)	6.3(-6)	2.8(-5)	2.7(-1)
0.9	2.9(-6)	2.3(-6)	2.2(-6)	3.4(-6)	4.0(-6)	3.0(-5)	1.8(-1)
1.0	2.6(-6)	1.8(-6)	1.8(-6)	3.1(-6)	1.4(-6)	1.8(-5)	1.2(-1)

VI. SCATTERING BY DEBRIS PARTICLES

For particles in the 10^{-2}-10 cm range, scattering can be treated essentially as isotropic with a geometrical cross section. Thus, the differential cross section can be written as

$$\frac{d\sigma}{d\Omega} = \frac{\pi a^2 \, a_n}{4\pi} \qquad \text{(III-26)}$$

where the albedo a_n is taken equal to that of the nucleus, 0.1. Calculating an average differential cross section for $R_s = 0.8$ AU using the distribution in Table III-2 results in

$$\frac{d\sigma}{d\Omega} = \frac{\bar{a}^2 \, a_n}{4} = 9.9 \times 10^1 \; \mu m^2 \, sr^{-1} \qquad \text{(III-27)}$$

where $\bar{a}^2$ is the rms radius of large particles, $a > 44\,\mu m$. The column density for the debris particles is given by Equation (B-3) which results in

$$n_T = \frac{P_i}{v_i}\,\frac{1}{4\pi R_{min}} = 2.5 \times 10^{-1}\ \text{particles cm}^{-2} \qquad \text{(III-28)}$$

Using Equations (III-27), (III-28) with Equation (III-24), we then would get a scattered brightness for large particles at $R_s = 0.8\,\text{AU}$ for $\lambda = 0.5\,\mu m$ of

$$N_\lambda = 8.9 \times 10^{-8}\ \text{W cm}^{-2}\,\text{sr}^{-1}\,\mu m^{-1} \qquad \text{(III-29)}$$

As can be seen from Table III-4, this contribution is less than the small particle Mie scattering by a factor of 50. So it can be concluded, following our model, that the small size dust particles contribute much more to the scattered brightness than the large size debris particles.

VII. SCATTERING BY ICE PARTICLES

It is difficult to precisely assess the ice particle distribution and production rates for Encke. We shall assume here that the ice particles can be represented by particles with a radius of $300\,\mu m$ (Delsemme and Miller, 1971). An upper limit for the ice production rate can be derived from the OGO-5 satellite observations of Lyman-α emission from Encke. The observed emission corresponded to a production rate of $Q(H) = 5 \times 10^{26}$ atoms $\text{sr}^{-1}\,\text{s}^{-1}$ for hydrogen atoms at $R_s = 0.715\,\text{AU}$ (Bertaux et al., 1973). Assuming that all the H atoms came from ice particles results in a production rate for water $Q(H_2O) = 3 \times 10^{27}$ molecules s^{-1} (Delsemme and Rud, 1973). For icy grains of $300\,\mu m$ radius, we then have $Q_{ice} \sim 2 \times 10^9\ \text{s}^{-1}$.

Using these numbers, it is possible to estimate the scattered sunlight assuming an albedo of 0.9. For the differential cross section we have

$$\frac{d\sigma}{d\Omega} = 2.0 \times 10^4\ \mu m^2\,\text{sr}^{-1} \qquad \text{(III-30)}$$

and the column density would be

$$n_T \sim 9 \times 10^{-2}\ \text{particles cm}^{-2} \qquad \text{(III-31)}$$

An estimate of the scattered light would then yield for $\lambda = 0.5\,\mu m$ and $R_s = 0.8\,\text{AU}$

$$N_\lambda = 6 \times 10^{-5}\ \text{W cm}^{-2}\,\text{sr}^{-1}\,\mu m^{-1} \qquad \text{(III-32)}$$

This result is of the same order of magnitude as the results for Mie scattering for cometary dust suggesting that scattering by ice particles surrounding the nucleus could be a major contributer to scattered sunlight. On the otherhand, our ice model is tentative and ice production rates could be revised downward.

VIII. SUNLIGHT REFLECTION FROM THE NUCLEUS

We have assumed an albedo of 0.1 for the nucleus so the brightness of the nucleus following Equation (III-24) is given by

$$N_\lambda^{nuc} = B_\lambda(\Delta\alpha)\,\frac{0.1}{2\pi} \qquad\qquad \text{(III-33)}$$

where $\Delta\alpha$ is the solid angle subtended by the sun at a given heliocentric distance, R_s. It varies as R_s^{-2}. It is assumed here that the scattering is isotropic into 2π sr. For $\lambda = 0.5\,\mu m$ and $R_s = 0.8\,AU$, we have

$$N_\lambda^{nuc} = 5.7 \times 10^{-3}\ W\,cm^{-2}\,sr^{-1}\,\mu m^{-1} \qquad\qquad \text{(III-34)}$$

IX. COMPARISON OF BRIGHTNESS OF NUCLEUS TO BACKGROUND BRIGHTNESS

The contribution to the background brightness from the comet dust is tabulated in Table III-5. Taking one specific case we can compare the brightnesses from the nucleus to the background brightness. For the case with a heliocentric distance of 0.8 AU, $\lambda = 0.5\,\mu m$, and view angle $\alpha = 90°$, the radiance levels are presented in Table III-IV.

The background from particulate scattering is 2 to 3 orders of magnitude below the intensity from the nucleus. The relative particle to nuclear brightness levels in Table III-4 are expected to vary less than an order of magnitude going into perhelion (0.34 AU) or out to "turn on" at about 2 AU.

Table III-5

Radiances at $R_s = 0.8\,AU$ for $\lambda = 0.5\,\mu m$, $\alpha = 90°$

Nucleus	Particulate Scattering		
	Dust	Debris	Ice
Radiances 5.7 x 10⁻³ (W cm⁻² sr⁻¹ μm⁻¹)	5.4 x 10⁻⁶	8.9 x 10⁻⁸	6 x 10⁻⁶

Based on these calculations there should be no difficulty in viewing the nucleus from masking by particulate scattering. The particles are optically thin and the brightness levels are several orders of magnitude down from that of the nucleus.

X. OPTIMIZATION OF IMAGING SYSTEM

In terms of scientific value, resolution as high as possible is desired to examine the nature and composition of the surface. One of the problems with high resolution imagery and perhaps the limiting one is the large relative velocity of the spacecraft and comet which can be of the order of 10 km/sec. This, of course, would depend on the particular mission trajectory selected. Blurring of the image while a pixel cell is being exposed necessitates short exposure times. This requirement would argue for a high sensitivity-low noise system such as an image disector or a spin-scan camera. As an example of some numbers consider the case where the desired resolution element is ten meters squared on the surface of the nucleus and the bandwidth is 0.1μ. Then the photon rate corresponding to a resolution element would be $N = 1 \times 10^{21}$ photons-sec^{-1}-sr^{-1}. The solid angle subtended by a 5" diameter telescope at 1000 km would be about 2.5×10^{-15} ster and would result in photon rate at the detector of 3×10^6 photons/sec per pixel cell. If the transverse velocity of the comet with respect to the spacecraft is of the order of 10 km/sec then exposure times/pixel of no more than 1 msec are required. This corresponds to 6×10^3 photons/pixel which is sufficient to detect intensity variations from the surface of 4%. It should be noted that the intrinsic readout noise of a vidicon system corresponds to about 1000 electrons/pixel.

Other options which should be considered with an imaging system are use of polarizers to gain polarization information about the nuclear surface. Because the illumination of the nucleus will be quasi-lambertian, viewing at different phase angles will afford information regarding surface irregularities. Shadow heights can be used to topographically map the surface. The use of filters to block out line and band emission features in the bandwidth of the imaging system may be deemed wise.

It is concluded that dust and debris scattering will not compromise the nucleus imaging mission and that high relative velocities warrant the use of a low noise imaging system such as a spin-scan camera.

REFERENCES

Bertaux, J. L., Blamont, J. E. and Festou, M.; "Interpretation of Hydrogen Lyman-Alpha Observations of Comets Bennett and Encke," Astron. and Astrophys., 25, 415, 1973.

Corben, H. C.; "Remarks on a Comet Probe," in Space AGE Astronomy, Academic Press, New York, 380-382, 1962.

Dave, J. V.; Subroutines for Computing the Parameters of the Electromagnetic Radiation Scattered by a Sphere, IBM Scientific Center, Palo Alto, Calif.,

Delsemme, A. H. and Miller, D. C.; "Physico-Chemical Phenomena in Comets-III. The Continuum of Comet Burnham (1960 II)," Planet. Space Sci., 19, 1229, 1971.

Delsemme, A. H. and Rud, D. A.; "Albedos and Cross-sections for the Nuclei of Comets 1969 IX, 1970 II, and 1971 I," Astron. and Astrophys., 28, 1, 1973.

Delsemme, A. H.; Space Sci. Rev., 15, 89, 1973.

Dohnanyi, J. S.; Icarus 17, 1, 1972.

Donn, B., Powerll, R., and Remy-Battiau, L.; "Interpretation of the Continuous Spectra of Comets," Nature 213, 379, 1967.

Finson, M. J. and Probstein, R. R.; "A Theory of Dust Comets. II. Results for Comet Arend-Roland," Astrophys. J., 154, No. 1, Part 1, 353, 1968.

Friedlander, A. L.; On the Problem of Comet Orbit Determination for Spacecraft Intercept Missions, IIT Research Institute Rep. T-19, 1967 (N67-28832).

Gal, G.; Electromagnetic Scattering From Particulate Clouds, Technical Report, LMSC D401089, Contract N00030-74-C-01-00, April, 1974.

Gal, G. and Kirch, H.; Particulate Optical Properties in Rocket Plumes, Final Report, Contract F04611-72-C-0034, DARPA O/N 1857, AFRL-TR-73-99, LMSC D354502, November 1973.

Lust, R.; "Cometary Probes," Space Science Rev. 10, 217-229, 1969.

Lyttleton, R. A.; Astrophy. Space Sci., 15, 175, 1972.

Maines, P., Grudinska, S. and Stawiskowski, A.; "Observations Physiques de la Comete Periodique Giacobini-Zinner (1959b)," Annales d'Astrophysique, 23, 788-796, 1960.

Marsden, B. G. and Sekanina, Z.; Astron. J. 79, 413, 1974.

Marsden, B. G., Sekanina, Z. and Yeomans, D. K.; Astron. J. 78, 211, 1973.

Marsden, B. G. and Sekanina, Z.; Astron. J. 76, 1135, 1971.

Opik, E. J.; "The Stray Bodies in the Solar System, Part II," Adv. Astron. Astrophys. 4, 302, 1966.

Porter, J., Herrick, S., Rabe, E. and Roemer, E.; "Report on Comet Fly-by," European Space Res. Org. Rep. ESRO No. CFSG/10, 28.6, 1965.

Probstein, R. F.; Problems in Hydrodynamics and Continuum Mechanics, Soc. Indust. Applied Mech., Philadelphia, Pa., 568, 1958.

Roemer, E.; Mercury 1, No. 6, 18, 1972.

Roemer, E.; "Comet Notes," Mercury 1, 18-19, 1972.

Roemer, E., "The Dimensions of Cometary Nuclei," Mem. Soc. Roy. des Sci. de Liege, 12, 23, 1966.

Sekanina, Z.; private communication, 1974.

Sekanina, Z. and Miller, P. D.; "Comet Bennett 1970 II," Science 179, 565-567, 1973.

Sekanina, Z.; "Dynamical and Evolutionary Aspects of Gradual Deactivation of Short-Period Comets," Astron. J. 74, No. 10, 1223, 1970.

Sekanina, Z.; "Total Gas Concentration in Atmospheres of the Short Period Comets and Impulsive Forces Upon Their Nuclei," Astron. J. 74, 944-950, 1969.

Sekanina, Z.; Astron. J. 74, 1223, 1969b.

Sekanina, Z.; Astron. J. 74, 944, 1969a.

Swings, P.; "Objectives of Space Investigations of Comets," in Space Age Astronomy, Academic Press, New York, 370-379, 1962.

Taylor, F. W., Michaux, C. M. and Newburn, R. L., Jr.; A Model of the Physical Properties of Comet Encke, JPL Technical Report 32-1590, NASA-CR-135707, Oct. 1973.

TRW, Study of a Comet Rendevous Mission, TRW Tech. Rep. 72-87, 1972.

van de Hulst, H. C.; Light Scattering by Small Particles, New York, Wiley, 1957.

Verniani, F.; Space Sci. Rev. 10, 230, 1969.

Verniani, F.; J. Geophys. Res. 78, 8429, 1973.

Vsekhsvyatskii, S.; Physical Characteristics of Comets, NASA TT F-80, 1964.

Whipple, F. L.; Smithsonian Astrophysical Observatory Special Report 239, 1967.

Whipple, F. L.; in IAU Symposium No. 33, p. 481, 1968.

Whipple, F. L. and Douglas-Hamilton, D. H.; "Brightness Changes in Periodic Comets," Mem. Soc. Roy. des. Sci. de Liege 12, 469-480, 1965.

Whipple, F. L.; "Solid Particles in the Solar System," J. Geophys. Res. 64, 1653-1664, 1959.

Whipple, F. L.; "A Comet Model. 1. The Acceleration of Comet Encke," Astrophys. J. 111, 375-394, 1950.

Wickramasinghe, N. C. and Krishna Swamy, K. S.; Astrophys. J. 154, 397, 1968.

Yoemans, D.; Physical Description and Recovery Data for P/Encke, Computer Sciences Corp., Silver Springs, Md., 1973.

ANGULAR DISTRIBUTIONS FOR SINGLE
PARTICLE MIE SCATTERING
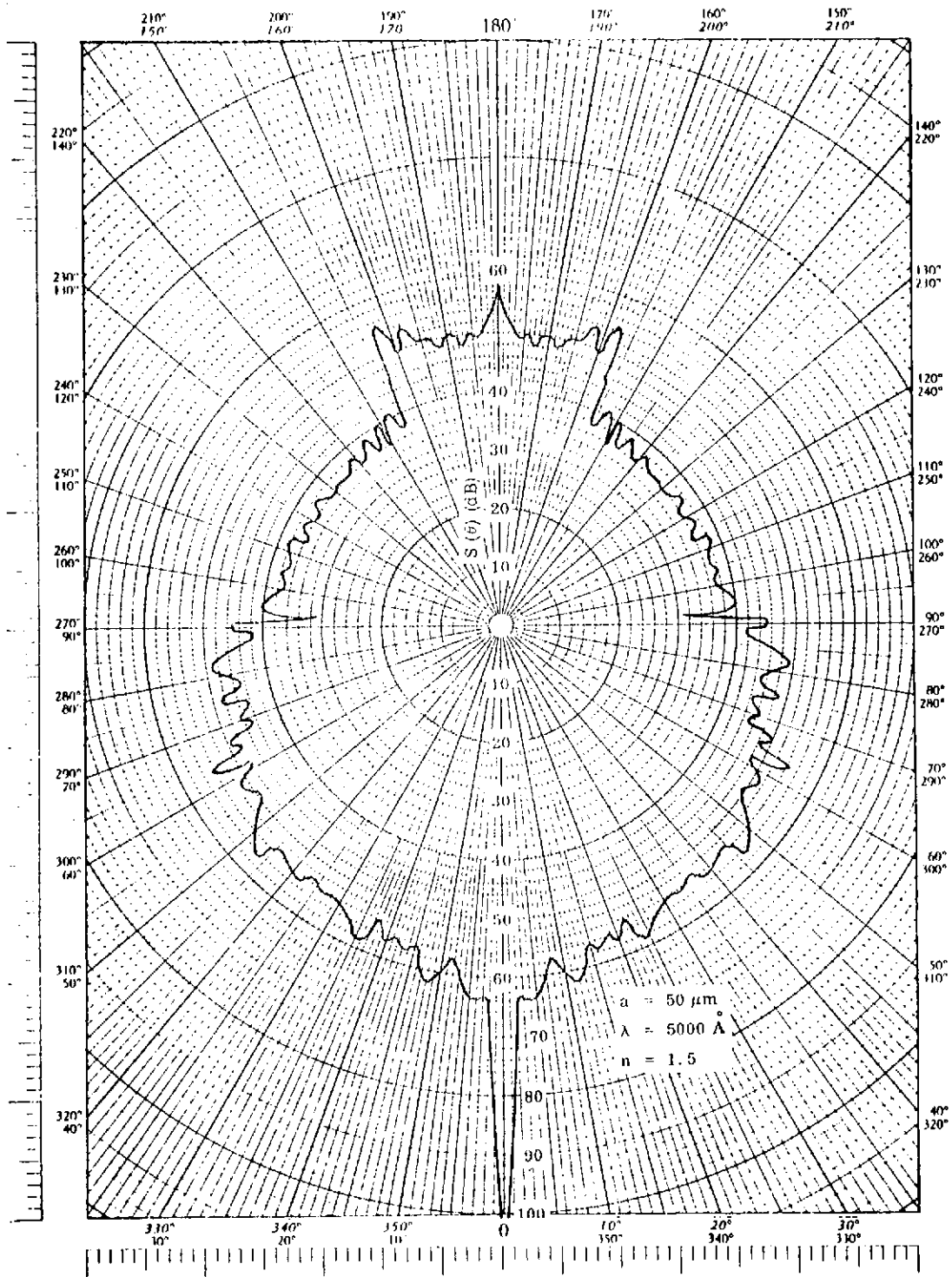
Figure A1. Angular Dependence of Scattering Function, a = 50 μm, n = 1.5

III-35
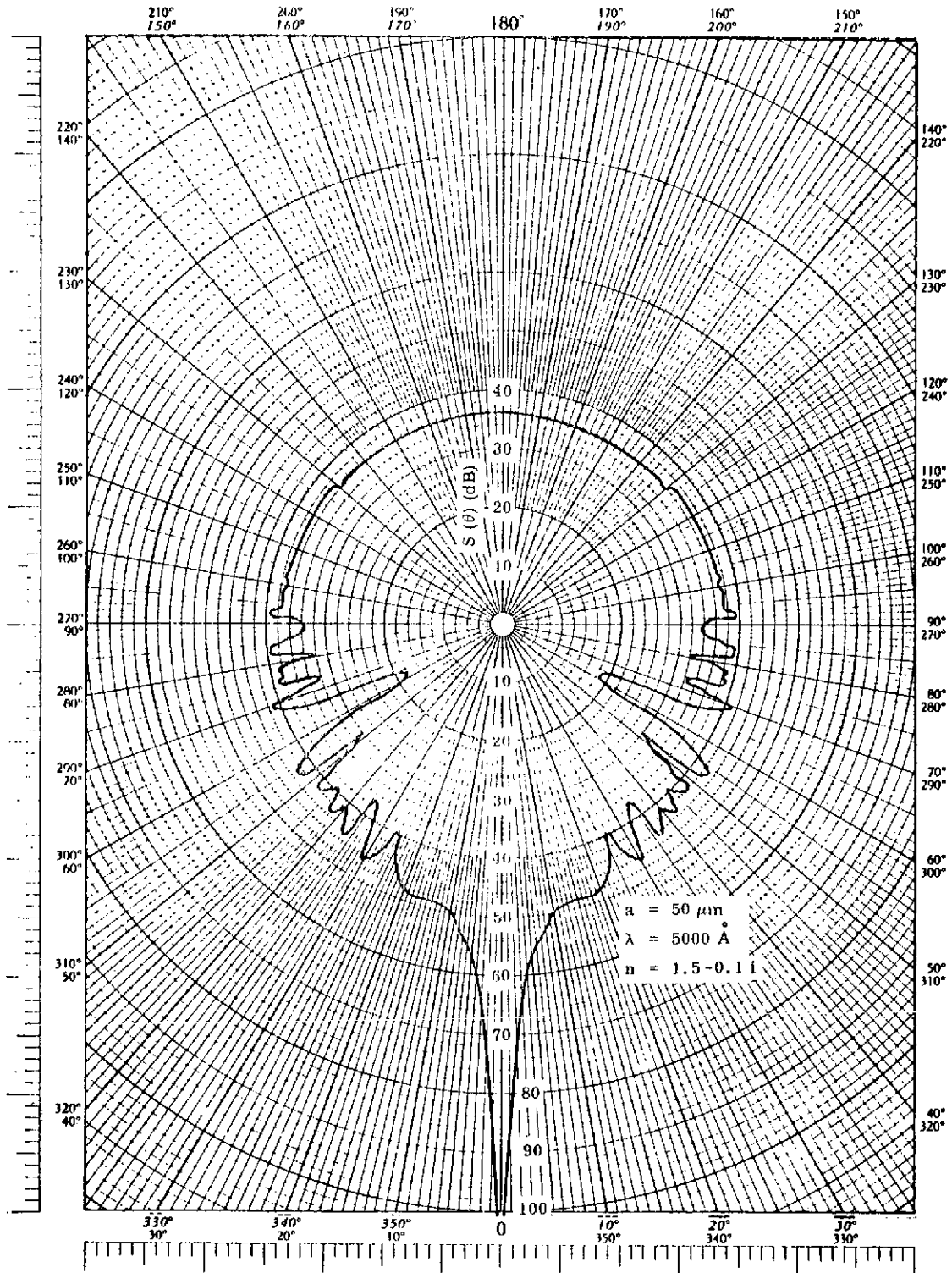
Figure A2. Angular Dependence of Scattering Function,
a = 50 μm, n = 1.5–0.1 i
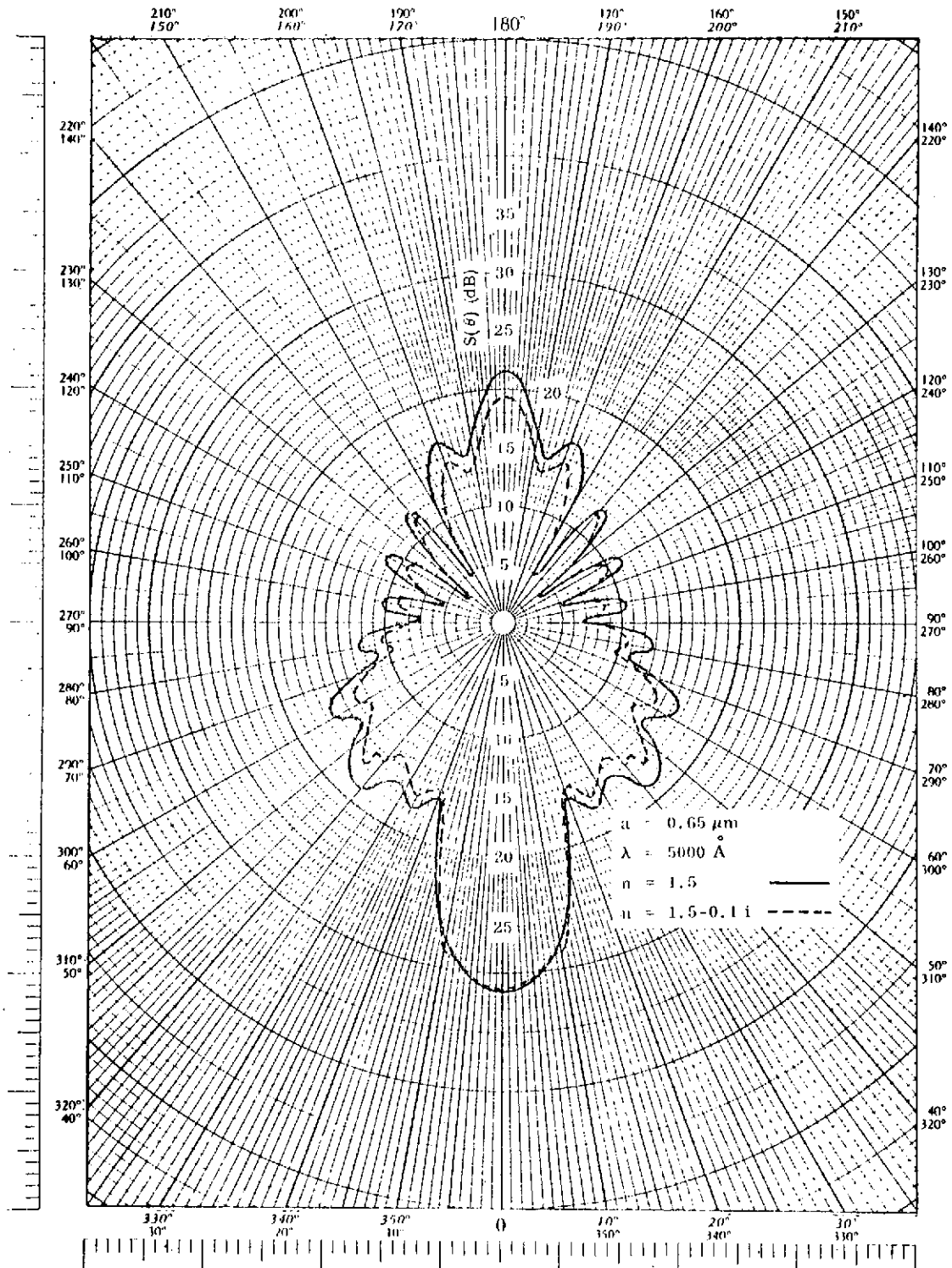
Figure A3. Angular Dependence of Scattering Function,
a = 0.65 μm, n = 1.5, 1.5-0.1 i
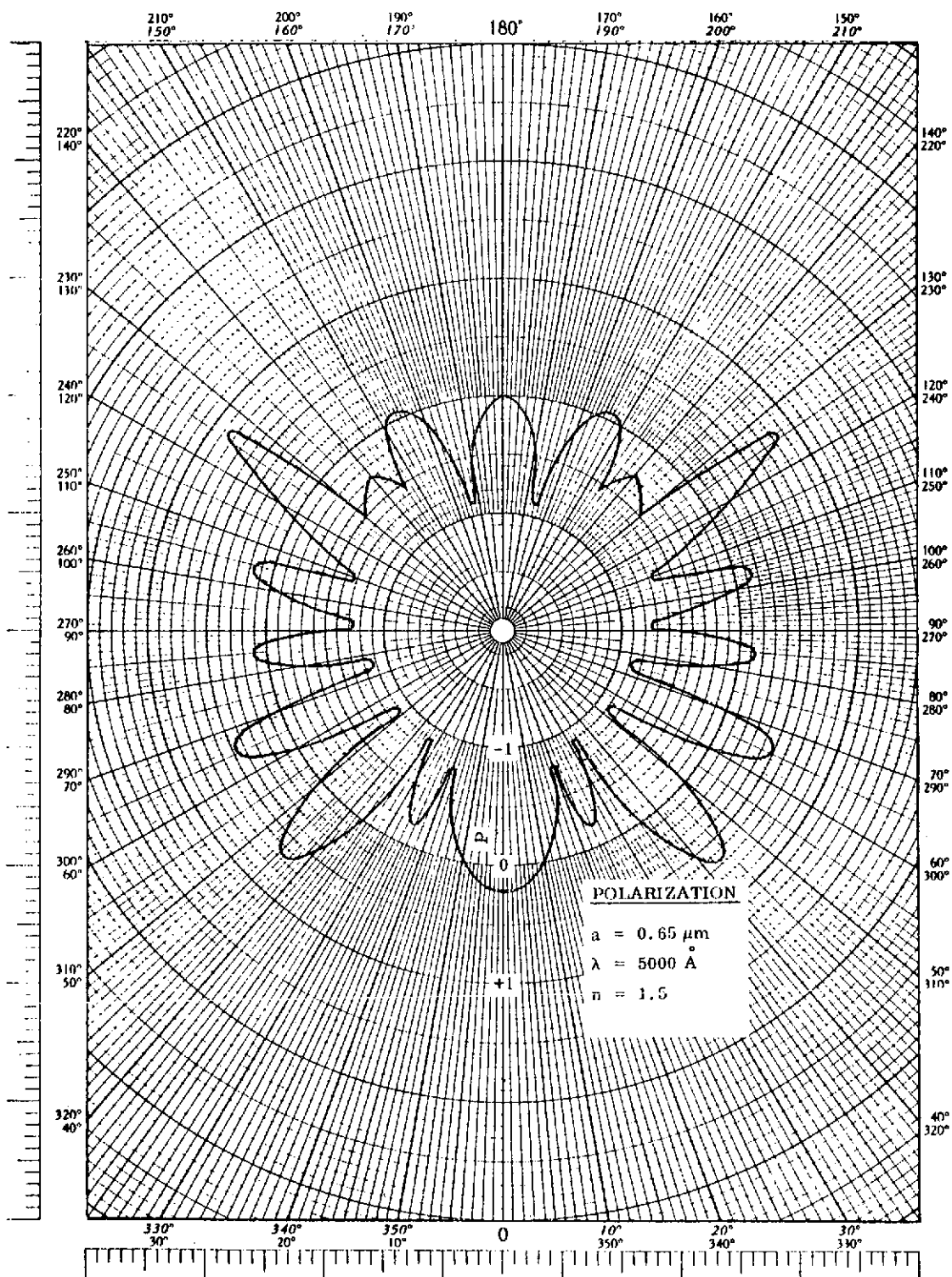
Figure A4. Angular Dependence of Polarization, a - 0.65 μm, n = 1.5
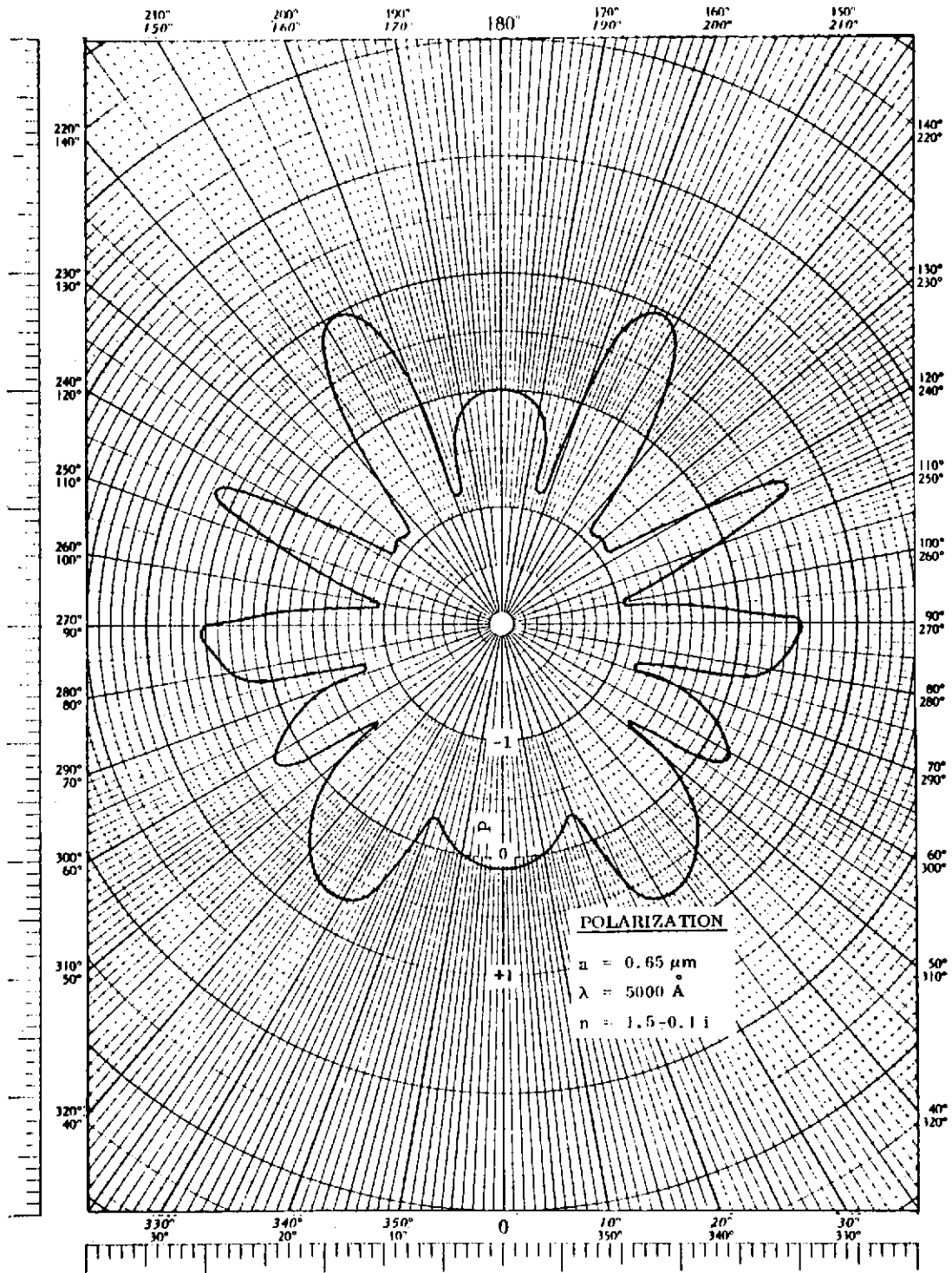
Figure A5.   Angular Dependence of Polarization, a = 0.65 μm, n = 1.5-0.1i
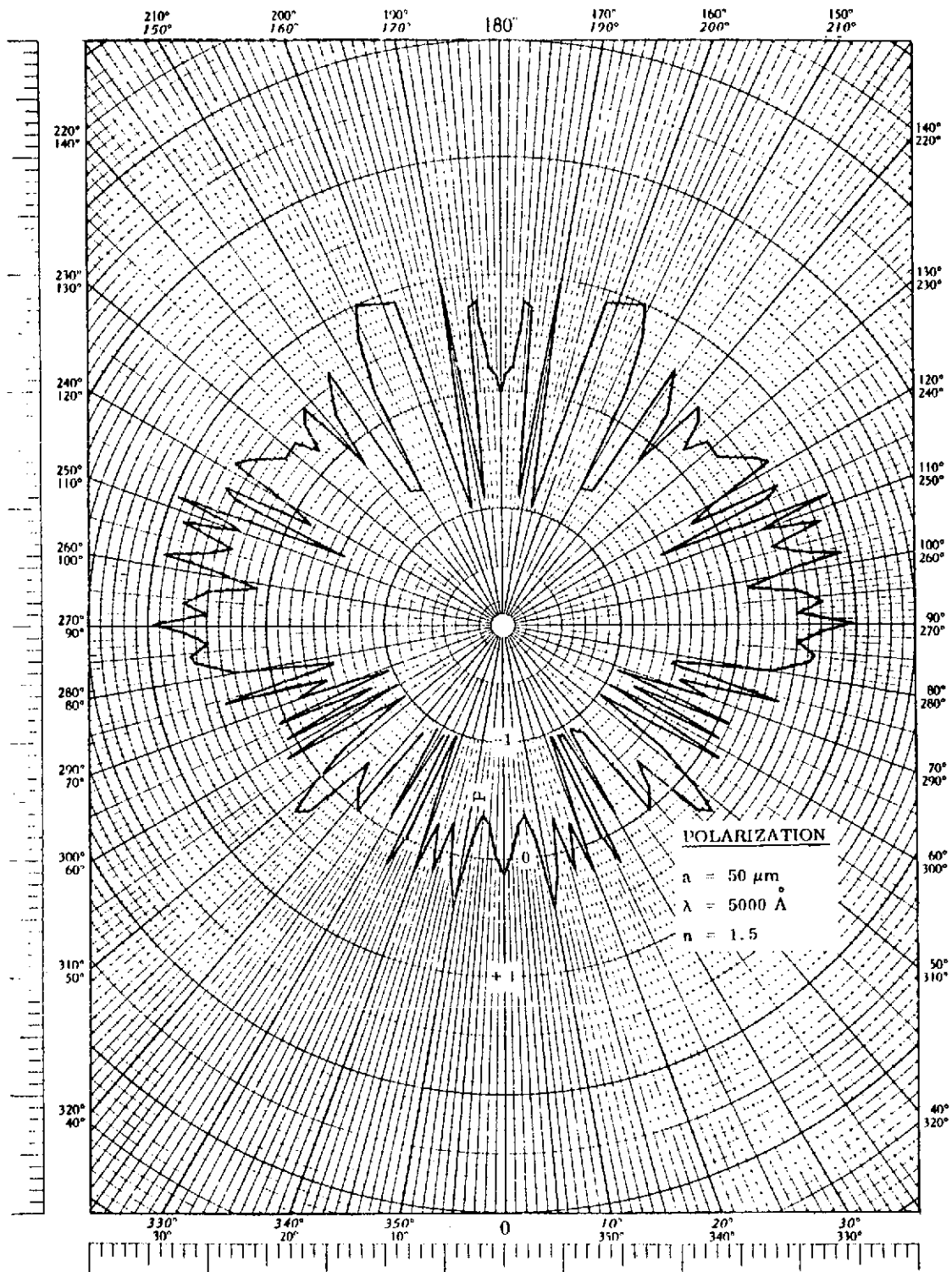
Figure A6. Angular Dependence of Polarization, a = 0.50 μm, n = 1.5
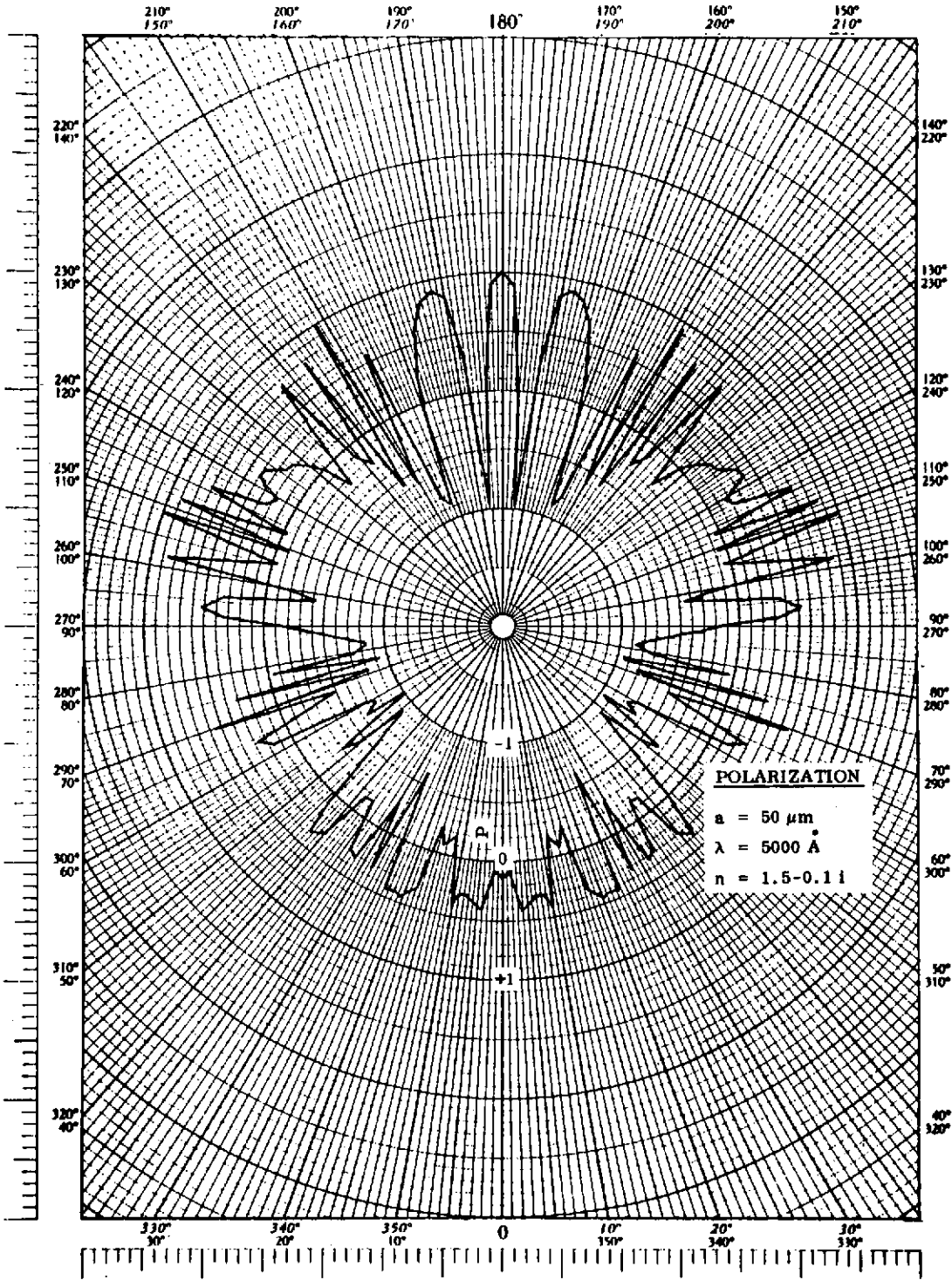
Figure A7. Angular Dependence of Polarization, a = 50 μm, n = 1.5-0.1i

CALCULATION OF COLUMN DENSITIES

CALCULATION OF COLUMN DENSITIES

The number of particles N passing through a spherical surface at a distance R from the center of the nucleus during a time Δt is given by

$$N = \sum_i P_i \, \Delta t = \sum_i n_i(R) \, v_i \, \Delta t \, 4\pi R^2 \qquad \text{(B-1)}$$

where P_i, n_i and v_i are the production rate, the number density and the terminal velocity, respectively, of the particles in the ith size range.

The number density as a function of R is then given by

$$n_i(R) = \frac{P_i}{v_i \, 4\pi R^2} \qquad \text{(B-2)}$$

The column density of particles n_{col} is obtained by integrating Equation (B-2) from R_{min} to R_{max}:

$$n_{col} = \sum_i \int_{R_{min}}^{R_{max}} \frac{P_i dR}{4\pi \, v_i R^2} \qquad \text{(B-3)}$$

R_{min} is the radius of the nucleus (R_n), and since v_i is constant for $R > 10 \, R_n$, the value of n_{col} is insensitive to the value of R_{max}. Equation (B-3) is actually the lower limit to n_{col}, since for $R < 10 \, R_n$ the particle velocities are less than V_i. The calculations of Delsemme and Miller (1971), shown in their Figure 2, suggest that the particles are subject to approximately constant acceleration until they move at nearly terminal velocity. The integral in Equation (B-3) is most sensitive to the particle velocities at small R. As an <u>upper limit</u> to n_{col}, suppose the actual particle velocities are given by

$$v(R) = \begin{cases} v_o & R_n \leqslant R < 10 \, R_n \\[2mm] v_i & R \geqslant 10 \, R_n \end{cases} \qquad \text{(B-4)}$$

Here v_o is the initial velocity at which particles are ejected from the nucleus. The column density for species i is then

$$n_{col} = \frac{P_i}{4\pi \, R_n v_i} \, [0.1 + 0.9(v_i/v_o)] \qquad \text{(B-5)}$$

Taking $v_o = 0.1 \, v_i$ gives a column density 9.1 times the value obtained from Equation (B-3) assuming $v = v_i$ everywhere. We could, of course, go on to

evaluate Equation (B-3) using the assumption of constant acceleration to obtain somewhat better estimates for n_{col}, but the results depend on the unknown ejection velocity v_0. For the present, we simply point out this refinement which should be included in more comprehensive models.

For calculating impacts suffered by a spacecraft passing near the comet, we have evaluated the column density for a linear path passing within R_0 km of the nucleus (we will call this the impact parameter). The complications discussed above are not encountered because $R_0 \gg R_n$. The spatial density is given by Equation (B-2), and the column density is

$$n_{col}(a, R_0) = \frac{P(a)}{4v(a)R_0} \qquad (B\text{-}6)$$

Since $v(a) \to 0$ as $a \to a_{max}$, the production rate $P(a)$ must also go to zero in order to avoid a singularity. Since the terminal velocity for $a > 10^{-4} \, a_{max}$ is given by

$$v(a) \simeq 2.88 \times 10^{-3} \, (a/a_{max})^{-1/2} \, [1 - (a/a_{max})^{1/2}] \text{ km/sec} \qquad (B\text{-}7)$$

(from Delsemme and Miller, 1971), we cut off the production rate by a factor $[1 - (a/a_{max})^{1/2}]$. This does not affect the results presented in Section III. The production rate for $a > 4.44 \times 10^{-3}$ cm is given by

$$P(a) = 7.298 \times 10^{-4} \, \dot{M}_{dust} \, a^{-5} \, [1 - (a/a_{max})^{1/2}] \text{ sec}^{-1} \qquad (B\text{-}8)$$

where $\dot{M}_{dust} \simeq 5 \times 10^4$ g sec^{-1} and $a_{max} = 15.5$ cm at heliocentric distance 0.8 AU, while $\dot{M}_{dust} \simeq 2.77 \times 10^5$ g sec^{-1} and $a_{max} = 98.2$ cm at 0.34 AU (perihelion).

Using Equations (B-7) and (B-8) in Equation (B-6), then integrating over particle sizes from a to a_{max}, we obtain the cummulative column density:

$$n(a, R_0) \equiv \int_a^{a_{max}} n_{col} \, da \qquad (B\text{-}9)$$

$$= 1.813 \times 10^{-7} \, \frac{\dot{M}_{dust}}{a_{max}^{1/2} R_0} \, [a^{-3.5} - a_{max}^{-3.5}] \qquad (B\text{-}10)$$

this represents the number of particles which have radii a or larger. Table B-1 gives representative values.
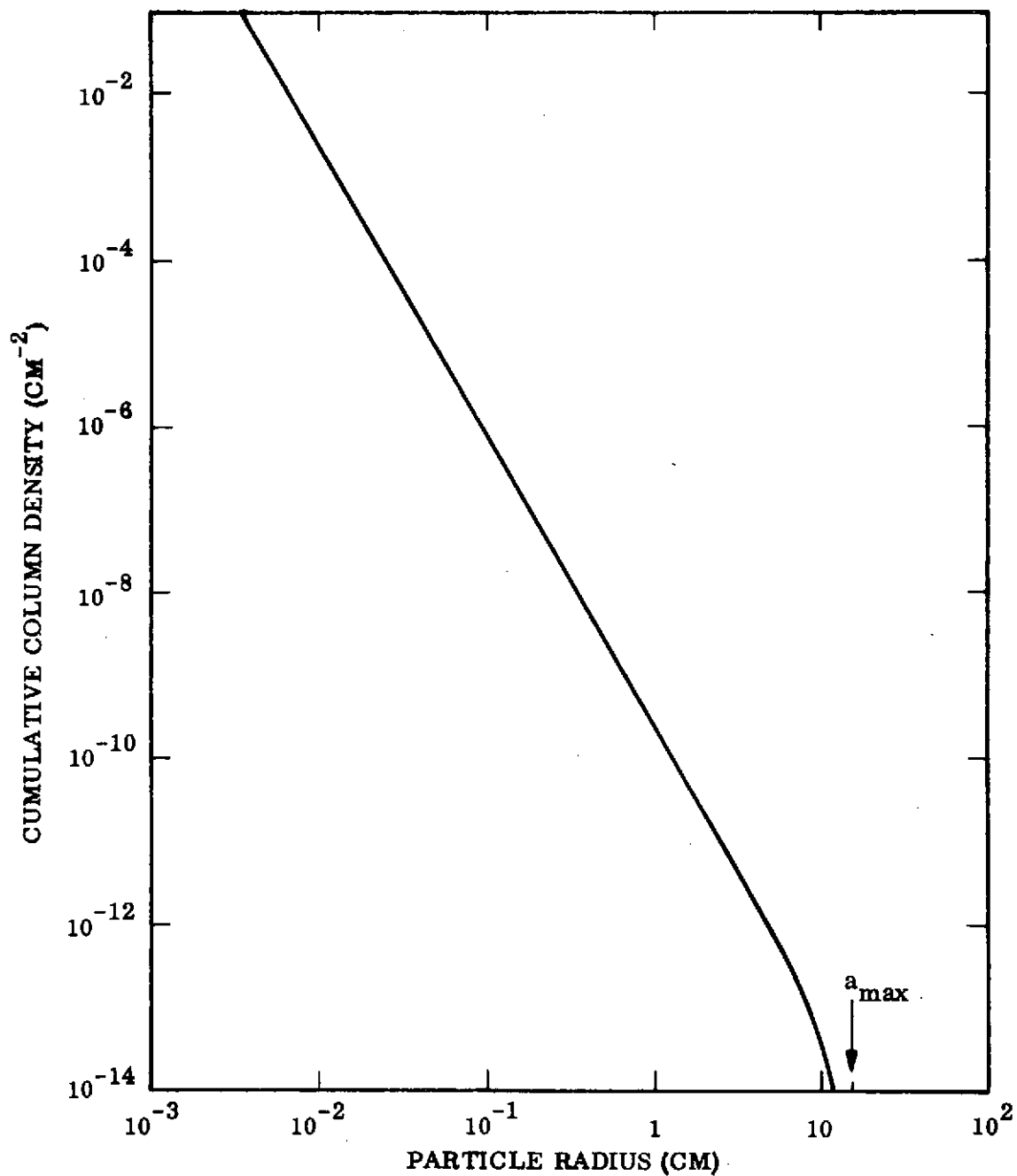
Figure B-1. Cumulative Column Density vs. Particle Radius

Table B-1

Column Densities For an Impact Parameter of 100 km

Heliocentric Distance (AU)	$n(a, 100\,\text{km})\ (\text{cm}^{-2})$		
	$a = 10^{-2}$ cm	$a = 10^{-1}$ cm	$a = 1$ cm
0.34	5.1×10^{-3}	1.6×10^{-6}	5.1×10^{-10}
0.8	2.3×10^{-3}	7.3×10^{-7}	2.3×10^{-10}

For given values of a and R_o, n varies approximately inversely as the heliocentric distance because $\dot{M}_{dust}$ and a_{max} both vary approximately as r^{-2}.

APPENDIX IV

MODEL OF IMAGING EXPERIMENT FOR 1980 ENCKE MISSIONS

T. E. Thorpe
Jet Propulsion Laboratory

APPENDIX IV

MODEL OF IMAGING EXPERIMENT FOR 1980 ENCKE MISSIONS

A complete description of the photometric characteristics of comet Encke includes three targets: coma, halo, and nucleus.

A. Coma

The model representing Encke's coma appearance at 1 AU comet-sun distance has been given by F. Taylor (Ref. 2). A relative brightness directly proportional to angular distance from the coma center has been combined with visual observations of the central brightness (B_0) to yield a function applicable to within 10^5 km radius of the nucleus. At comet-sun distances (Δ) other than 1 AU, the relative brightness is scaled according to the empirical observation

$$B_0 = Bo \times 10^{-0.4(15 \log \Delta)} \qquad \Delta \geqslant 0.7 \, AU$$

The signal recorded by a camera of given focal length is a function of both pointing within the coma and area of the projected pixel field-of-view. For this reason, it si convenient to compute the exposure obtained at each element of the camera's sensing device (Ref. 3):

$$Exp. = E_0/dw \; \frac{t\pi}{4T^2} \int_0^{d/2} \frac{r_0}{r + r_0} \, 2\pi r \, dr$$

where

E_0/dw = illuminance/str at the coma center

$t/4T^2$ = camera field-of-view with optics transmission and shutter speed

d = FOV_{pixel} x (Range to comet)

$\int dr$ = area of projected pixel convolved with brightness function

Because the intensity of coma emission is not radially symmetric over a given pixel, the following approximation is used:

$$Exp = E(x) t \; \frac{2\pi(\Delta x + r_0)(\Delta \log (x + r_0))}{\pi \bar{x}^2}$$

where

$$E(x) = \frac{E_o/dw}{4T^2} \cdot \pi$$

$\quad\quad\quad\quad$ = illuminance at pixel n, distance from coma center (x_n = nd $\pm$d/4)

$$\Delta x = x_2 - x_1$$

Finally, the light from the coma consists of discrete spectral emission bands. The total integrated brightness within the sensitivity of the camera is given by:

$$E_o = \sum_n E_n S_\lambda T_\lambda$$

where

$\quad$ n $\quad$ = spectral line

$\quad$ S_λ $\quad$ = camera sensor spectral sensitivity

$\quad$ T_λ $\quad$ = telescope spectral transmission

For example, according to the Taylor model, the coma illuminance per steradian at 1.2 km from the nucleus is 0.36 fc/str due to the C_2 line at λ = 5165 Å. Integration of all spectral lines produces an effective energy for GEC vidicons of 1.4 fc/str. The corresponding exposure at pixel n obtained by an approaching spacecraft depends only on the optics-sensor configuration ($4T^2$, FOV pixel), the spacecraft-comet range, and the comet-sun distance.

$$Exp_n = \frac{10^{(5 - 6 \log \Delta)}}{4T^2} \pi t \frac{(\Delta x + 1.1)(\Delta \log (x + 1.1))}{\bar{x}^2}$$

where

$\quad$ d $\quad$ = FOV pixel x Range (km)

$\quad$ Δ $\quad$ = comet-sun distance (AU) >0.7 AU

$\quad$ t $\quad$ = shutter speed (sec) <1 pixel S

$\quad$ x $\quad$ = nd-d/4

$$\bar{x} = (x_1 + x_2)/2$$

$$t = 1.3\, t/2 \quad \text{2 pixels smear}$$

$$t = 1.9\, t/5 \quad \text{5 pixels smear}$$

e.g., $S\mu r/sec$ 1 pixel smear = 6 sec

B. Halo

As discussed in the Taylor report, a continuous background spectrum is also observed in the spectra of Encke. At 1/5 the E_o/dw strength of the C_2 ($\lambda5165\text{Å}$) emission light, this reflected sunlight suggests the presence of a halo to a radius of approximately 1000 km. Regardless of whether this cloud is composed of icy grains or dust, an aerosol-scattering model (conservative) may be fitted to those observations. At comet-sun distances other than 1 AU, both the reflected light and the halo optical depth should be scaled proportional to the square of the solar distance:

$$E_{oh}/dw = (E_{oh}/dw)_{1\,AU} \times \left(\frac{1 - e^{-tM}}{1 - e - toM} \right) \times \frac{1}{\Delta^2} \times \widetilde{w}o$$

where

t = optical depth $(t_o\Delta^{-2})$

to = depth at 1 AU ~ 0.1 $(E_o/dw = 1/5\ C_2$ at 1 AU)

$\widetilde{w}o$ = scattering indicating ~ 1.0

M = air mass

$= 2$ at $i = e = g = 0$

Again, fitting an r^{-1} brightness function to $r = 10^3$ km (compromise between icy grains and dust particle scattering) the exposure is calculated as follows:

$$Exp = \frac{\pi 15t(x + r_o)}{4T^2} \frac{(\log(x + r_o)}{x^2} \left(\frac{1 - e^{-tM}}{1 - e^{-toM}} \right) \frac{1}{\Delta^2} \qquad r < 10^3\ km$$

C. Nucleus

A variety of possible nucleus sizes and albedos are predicted by differing brightness observations (which gives the product of albedo x area of surface disk).

Roemer's (Ref. 2) photography of Encke at aphelion (minimal coma activity) suggests $pr^2 = 0.8$; e.g., $r = 2\,km$, $p = 0.2$. Other observations over a large fraction of the orbital path indicate $pr^2 \geqslant 0.24$ ($r = 2\,km$, $p = 0.06$) or an apparent magnitude:

$$M_2 = 16.0 + 5 \log \Delta + 5 \log R + 0.03\,g$$

where

R = range to comet (AU)

$0.03\,g$ = lunar phase function

g = phase angle (deg)

Calculations in this memo use only M_2. The difference in intrinsic brightness, for example, at $R = 2.3 \times 10^6\,km$, $\Delta = 0.8\,AU$, $g = 13°$ is:

$$M_1 = -26.4 - 2.5 \log \frac{pr^2\,\phi}{\Delta^2 R^2} = 26.15 - 5 \log \frac{\phi^{1/2}}{\Delta R} = 5.6;\, pR^2 = 0.8$$

$$M_2 = 6.8,\, pR^2 = 0.24$$

where

$pr^2 = 0.8$

R = range (km)

Δ = (AU)

The camera response to a point source is predictable from television readout theory or by reference to flight experience:

$$Exp = 10^{-(6.71 + 0.4\,M)}\, t\, \frac{A}{a}\, TFf$$

where

$10^{-6.71}$ = illuminance (fcs) from a 0th mag star

$\dfrac{A}{a}$ = ratio of aperture to image area

T = optics transmission

$$F = \text{filter transmission}$$

$$f = \text{television read beam efficiency factor. } f \text{ may be determined by Mariner 9 star photography}$$

For example, the Mariner 9 B-camera with clear filter and MVM optics IR coatings (T = 0.525) receives an exposure of:

$$\text{Exp} = 10.8 \times 10^{-0.4M}\, t$$

As an extended source, the sensor exposure is given by:

$$\text{Exp} = \frac{Sp\,\phi}{\Delta^2}\, e^{-tM}\, \frac{tF}{4T^2}$$

where

$$S = \text{solar constant} \sim 13,000\ \text{fc}$$

The above camera would yield a signal-to-noise response (S/N = 10 at 0.01 fcs) to the nucleus of Encke (p = 0.2, g = 0°, Δ = 0.54 AU):

$$\text{S/N} = 10 \times \frac{\dfrac{9000}{4T^2}\, t\, F\, e^{-tM}}{0.01\ \text{fcs}} = 10^3 \times 110\ tF$$

The ways on which the expected imaging results are affected by the intercept mode are shown in Tables IV-1 and IV-2 and in Figures IV-1 thru IV-8.

REFERENCES

1. JPL Document No. 760-90; Rev. A, "A Study of the Solar Electric Slow Flyby of Comet Encke in 1980," dated 25 January 1974.

2. Taylor, F., et al., "A Model of the Physical Properties of Comet Encke," NASA TR No. 32-1590, dated 1 October 1973.

3. Thorpe, T., "1980-84 Comet Encke Encounter Science Imaging Experiment Instrument Definition Study," JPL IOM dated 10 May 1973.

Table IV-1

Comet–Sun Encounter Range Effects on Imaging Experiment*

Parameter	Encounter – Sun Distance		
	0.34 AU	0.53 AU	0.80 AU
1. Flyby velocity at encounter (km/sec)	8.6	18	26.8
2. Comet Observation Potentials			
Coma maximum signal to noise ratio at $E -10^d$ (clear filter, 6 second exposure)	45	18	6
Earliest halo detection (Range – km)	$E -14^d\ (10^{7.1})$	$E -3^d\ (10^{6.7})$	$E -1^d\ (10^{6.4})$
Earliest nucleus resolution (Range – km)			
$M = 16 + 5\log R + 5\log + 0.03\,g$:	$E -3^d\ (10^6)$	$E -1.6^d\ (10^{6.4})$	$E -0.8^d\ (10^{6.3})$
Without coma (10% filter):	$E -7^d\ (10^{6.8})$	$E -2.5^d\ (10^{6.6})$	$E -1.6^d\ (10^{6.5})$
Smear rate at encounter (pixels/sec)	287	600	895
Image smear for S/N = 50 with ρ = 0.2(0.05) (pixels) Enc. = 1500	0.1 (038)	0.4 (1.6)	1 (3.8)
1000	0.14 (0.57	0.6 (2.4)	1.4 (5.6)
500	0.28 (1.14)	1.2 (4.8)	2.8 (11.2)
3. Number of possible pictures			
Encounter duration with 2 km > 5 pixels (Seconds):	3000	1480	545
Number of pictures without a tape recorder			
Large frames** (84 sec/fr):	33 (50 Kbs) 4 (4 Kbs)	18 (120 Kbs)	7 (120 Kbs)

Table IV-1 (Continued)

Parameter	Encounter – Sun Distance		
	0.34 AU	0.53 AU	0.80 AU
3. Number of possible pictures (Cont.)			
Large frames (10 sec/fr):	33 (50 Kbs) 4 (4 Kbs)	39 (120 Kbs)	14 (120 Kbs)
Small frames*** (15 sec/fr):	94 (50 Kbs) 8 (4 Kbs)	39 (120 Kbs)	36 (120 Kbs)
Number of pictures with tape recorder (10^9 bit capacity)			
Large frames (84 sec/fr):	36	18	7
Large frames (10 sec/fr):	240	148	55
Small frames (15 sec/fr):	200	148	55
Linear rate per 84 sec (km/picture)	720	1510	2250
4. Spacecraft/Mission Concerns	0.34 AU	0.54 AU	0.78 AU
Hardware essentials:	FEPS, Tape recorder X band transmission	FEPS	—
Round trip light time at Encounter	16 min	9 min	5.5 min
Significant attributes (S/C) at Encounter	Fly by velocity	Compromise	Earth-S/C distance
Significant comet advantages:	Nucleus luminosity, Coma activity		

Table IV-1 (Continued)

Parameter	Encounter – Sun Distance		
	0.34 AU	0.54 AU	0.78 AU
4. Spacecraft/Mission Concerns (Cont.) Significant mission problems:	Automatic sequencing (No RT data with nucleus as an extended source)	Same	Same + number of nucleus pictures

*10^3 Km Encounter; 50 cm fl, f/2.35 Vidicon Camera; Despun Platform
**Large Frame: 700 x 800 elements x 8-bit/element = 4.5 x 10^6 bits
***Small Frame: 250 x 800 elements x 8-bit/element = 1.6 x 10^6 bits

Table IV-2

Comet-Spacecraft Encounter Range Effects on Imaging Experiment*

Parameter		Closest Encounter**			
		A(r = 0)	B(r = 0)	A(r = 400)	B(r = 400)
1. Encounter duration (Image ≥ 24 pixels): (seconds)	0.34 AU	606 sec	592 sec	593 sec	568 sec
	0.53 AU	289	284	282	266
	0.80 AU	194	193	190	179
2. Number of pictures possible at 20 sec/frame (Image ≥ 25 pixels)	0.34	30	29	29	28
	0.53	14	14	14	13
	0.80	10	10	10	9
3. Encounter Image Resolution at 0° phase (0.1 modulation) (midscale exposure, 10% albedo)	0.34	6 m	29 m	27 m	49 m
	0.53	10	23	32	58
	0.80	46	31	37	58
4. Encounter Image Resolution at 90° phase (0.1 modulation) (midscale exposure, 10% albedo)	0.34	32 m	33 m	30 m	50 m
	0.53	79	54	55	66
	0.30	260	240	230	153
5. Angular Encounter Rate (deg./sec)	0.34	5°/sec	0.9°/sec	1.0°/sec	0.6°/sec
	0.53	10.2	2.5	1.8	1.0
	0.80	23.9	4.9	2.9	1.5

Table IV-2 (Continued)

Parameter		Closest Encounter**			
		A(r = 0)	B(r = 0)	A(r = 400)	B(r = 400)
6. Data rate per image segment at encounter required for 10 second frame time (Kb/sec): (Image diameter x 800 samples x 7 bits/ sample)	0.34 0.53 0.80	390 KBS 380 605	73 KBS 93 124	79 KBS 66 73	43 KBS 37 38
7. Image size at Encounter (2 km nucleus):	0.34 0.53 0.80	700 pixels 680 1080	131 pixels 166 221	141 pixels 118 130	77 pixels 66 67

*50 cm fl, f/2.35 vidicon camera, despun platform

**0.34 AU: A(r = 0) = 95 km (optical navigation)   B(r = 0) = 510 km (w/o optical navigation)
          A(r = 400) = 471 km (optical navigation) B(r = 400) = 865 km (w/o optical navigation)

0.53 AU: A(r = 0) = 98 km (optical navigation)   B(r = 0) = 403 km (w/o optical navigation)
          A(r = 400) = 566 km (optical navigation) B(r = 400) = 1017 km (w/o optical navigation)

0.80 AU: A(r = 0) = 62 km (optical navigation)   B(r = 0) = 302 km (w/o optical navigation)
          A(r = 400) = 515 (optical navigation)   B(r = 400) = 996 km (w/o optical navigation)
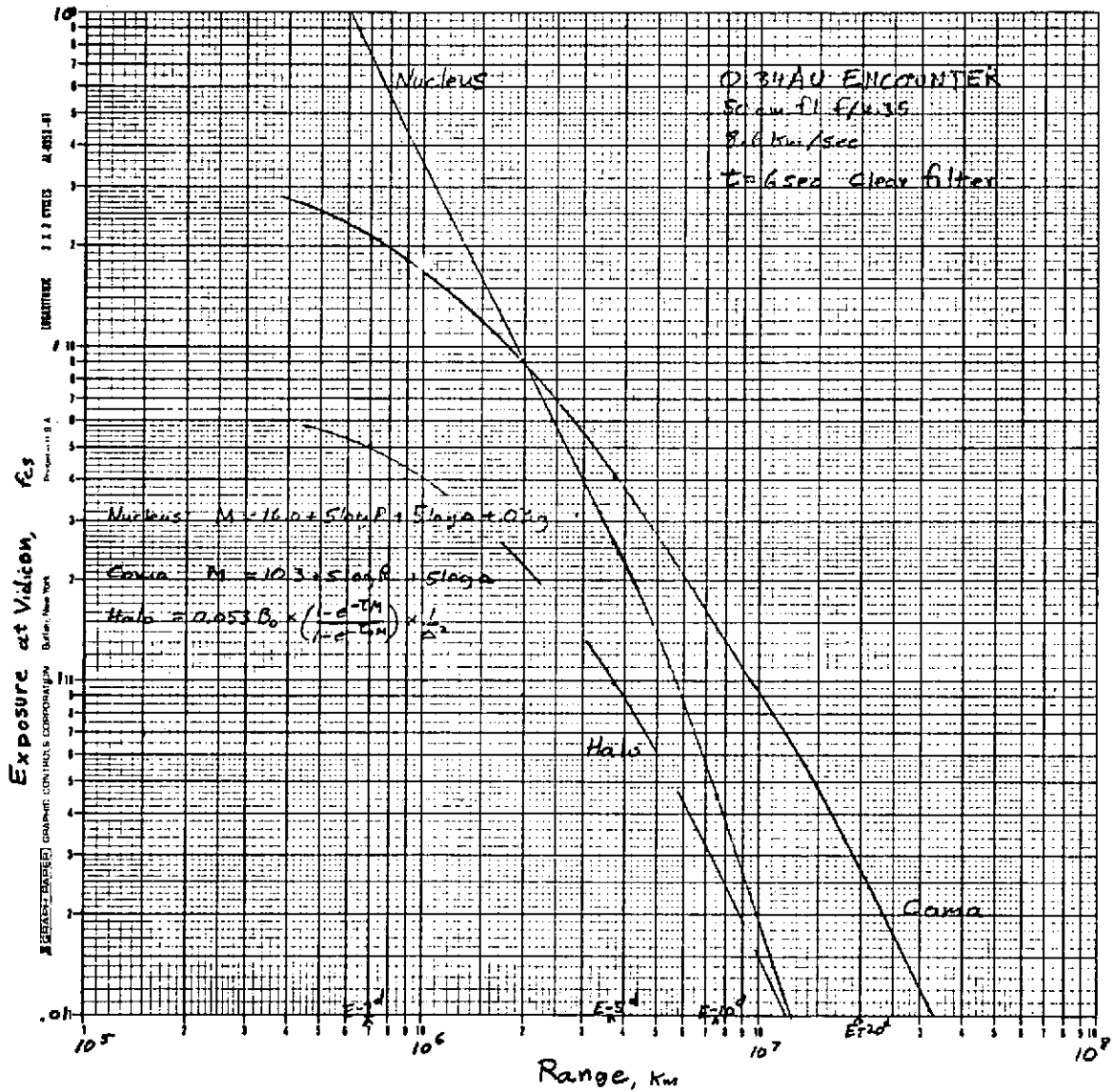
Figure IV-1. This figure compares the relative brightness of Encke's coma, halo and nucleus image center as a function of spacecraft distance for a 0.34 AU comet-sun distance. With a camera threshold of 10^{-2} fcs (S/N = 10), the broad bandpass coma image is detected more than 20 days before encounter; however, the nucleus does not exceed background coma emission until E - 3 days.
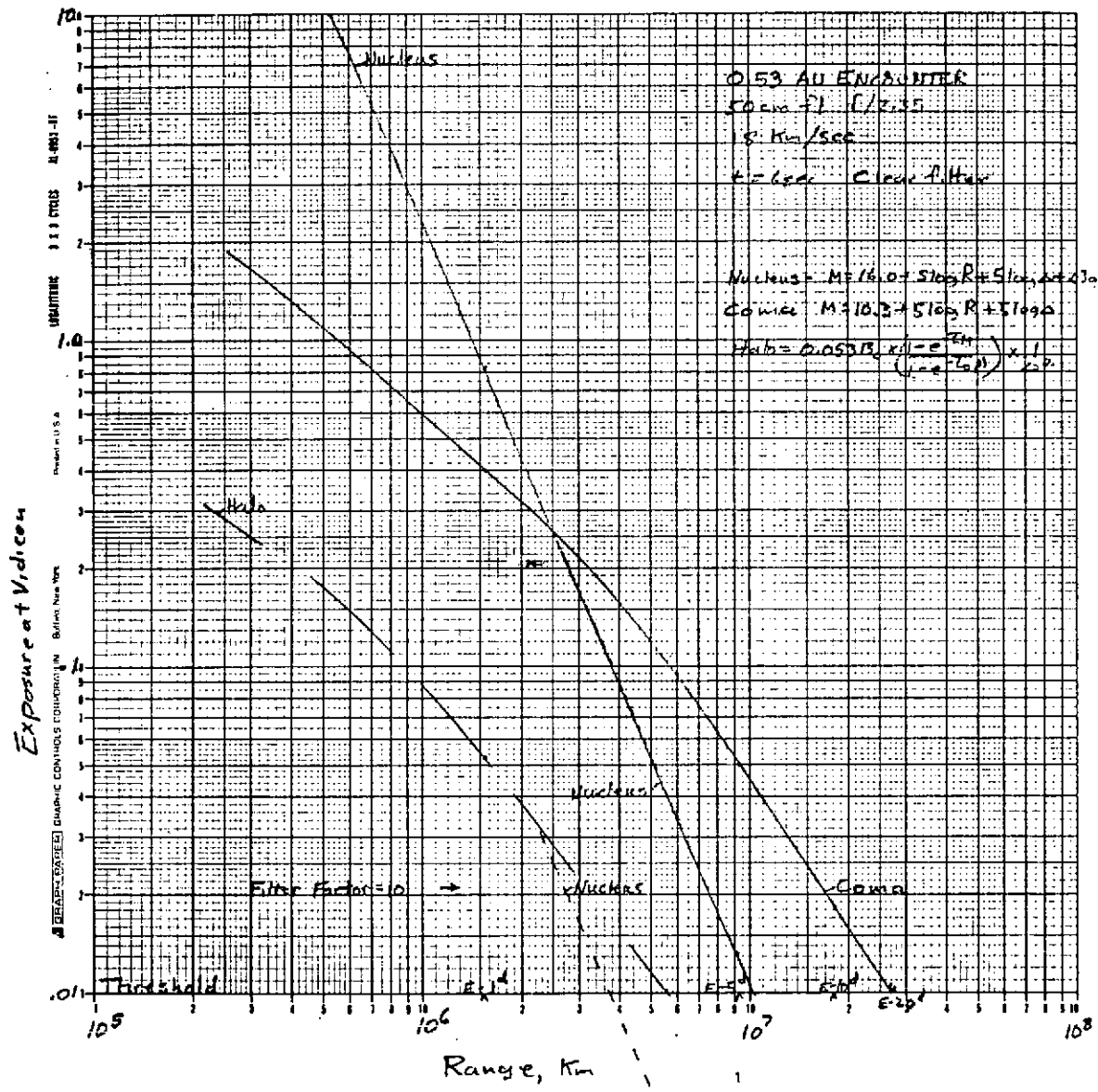
Figure IV-2. This figure compares the relative brightness of Encke's coma, halo and nucleus image center as a function of spacecraft distance for a 0.53 AU comet-sun distance. With a camera threshold of 10^{-2} fcs (S/N = 10), the broad bandpass coma image is detected more than 15 days before encounter; however, the nucleus does not exceed background coma emission until E - 2 days.

Figure IV-3. This figure compares the relative brightness of Encke's coma, halo and nucleus image center as a function of spacecraft distance for a 0.80 AU comet-sun distance. With a camera threshold of 10^{-2} fcs (S/N = 10), the broad bandpass coma image is detected more than 5 days before encounter; however, the nucleus does not exceed background coma emission until E - 1 day.
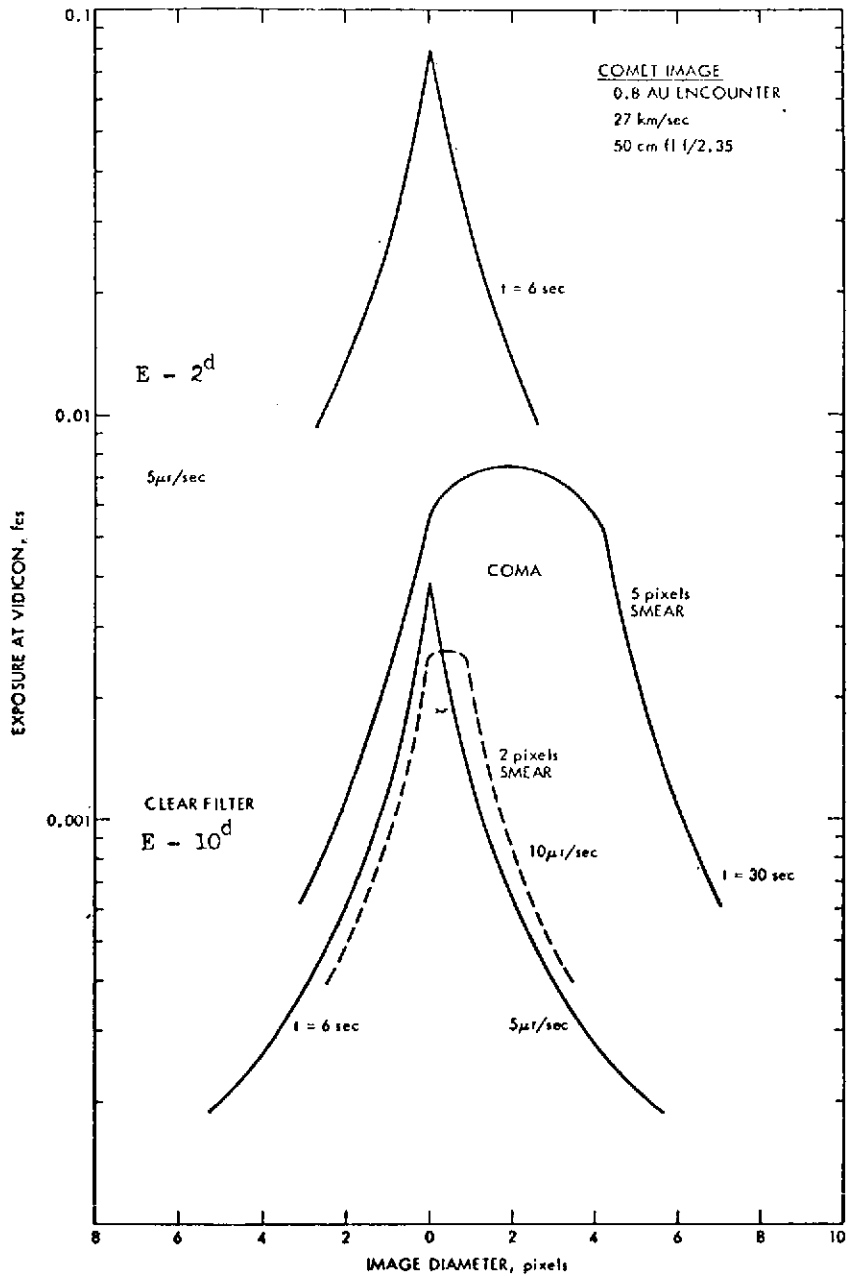
Figure IV-4. The apparent coma image size (abcissa) and
signal-to-noise ratio (ordinate) are shown in this graph to be a
function of shutter speed and spacecraft range. At 0.8 AU, as-
suming a spacecraft attitude drift rate of 5ur/sec, a 30-second
shutter speed would yield an image nearly twice as bright as a
6-second exposure but would exhibit 5 picture elements of
smear. The camera threshold of 10^{-2} fcs, however, is not
quite attained at E - 10 days using a clear filter.

EXPOSURE AT VIDICON, fcs

1

0.1

0.01

0.001

0.0001

t = 12 sec
(5 μr/sec)

t = 3 sec
(10 μr/sec)

t = 6 sec
(5 μr/sec)

COMET IMAGE
0.53 AU ENCOUNTER
50 cm f/2.35 TELESCOPE
18 km/sec
E – 15^h

CLEAR FILTER

t = 30 sec
(10 μr/sec)

THRESHOLD

t = 60 sec
(5 μr/sec)

t = 30 sec
(5 μr/sec)

t = 3 sec
(10 μr/sec)

t = 12 sec
(5 μr/sec)

COMET IMAGE

E – 20^d

CLEAR FILTER

t = 6 sec
(10 μr/sec)

t = 6 sec
(5 μr/sec)

1 pixel = 30 μr

IMAGE DIAMETER, pixels
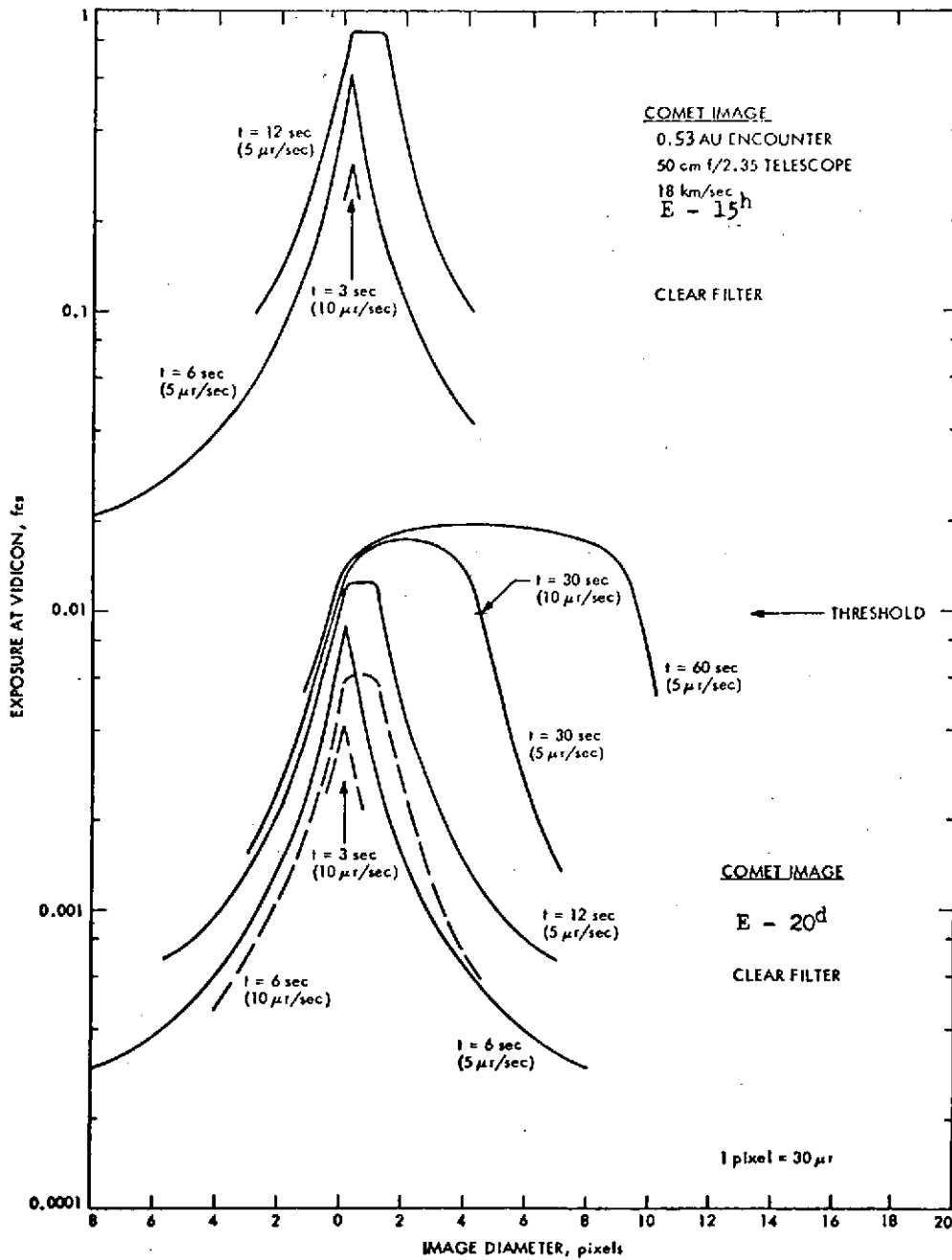
Figure IV-5. The apparent coma image size (abcissa) and signal-to-noise ratio (ordinate) are shown in this graph to be a function of shutter speed and spacecraft range. At 0.53 AU, assuming a spacecraft attitude drift rate of 5 ur/sec, a 30-second shutter speed would yield an image nearly twice as bright as a 6-second exposure but would exhibit 5 picture elements of smear. The camera threshold of 10^{-2} fcs, however, is barely attained at E – 20 days using a clear filter.

IV-15
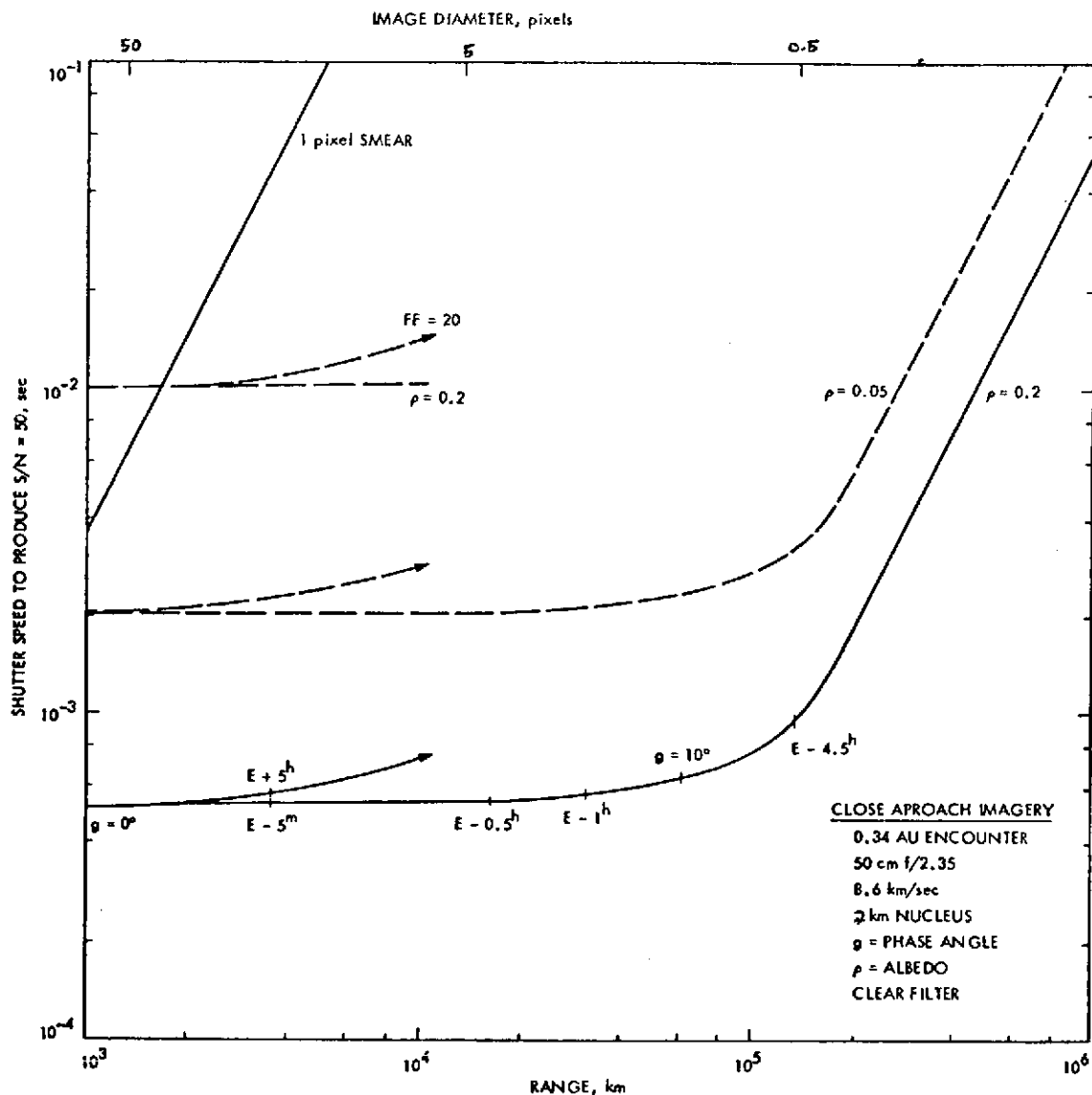
Figure IV-6. This figure illustrates the required shutter speed to obtain an image of the Encke nucleus at S/N=50. The image S/N is dependent on the nucleus brightness which is a function of albedo (0.05 vs. 0.2), phase geometry, and distance if the image is a point source ($>10^5$ km range). Following the approaching nucleus from right to left, it is apparent that the required shutter speeds yield less than one pixel of image smear (clear filter) unless narrow bandpass filters are used (Filter Factor = 20).
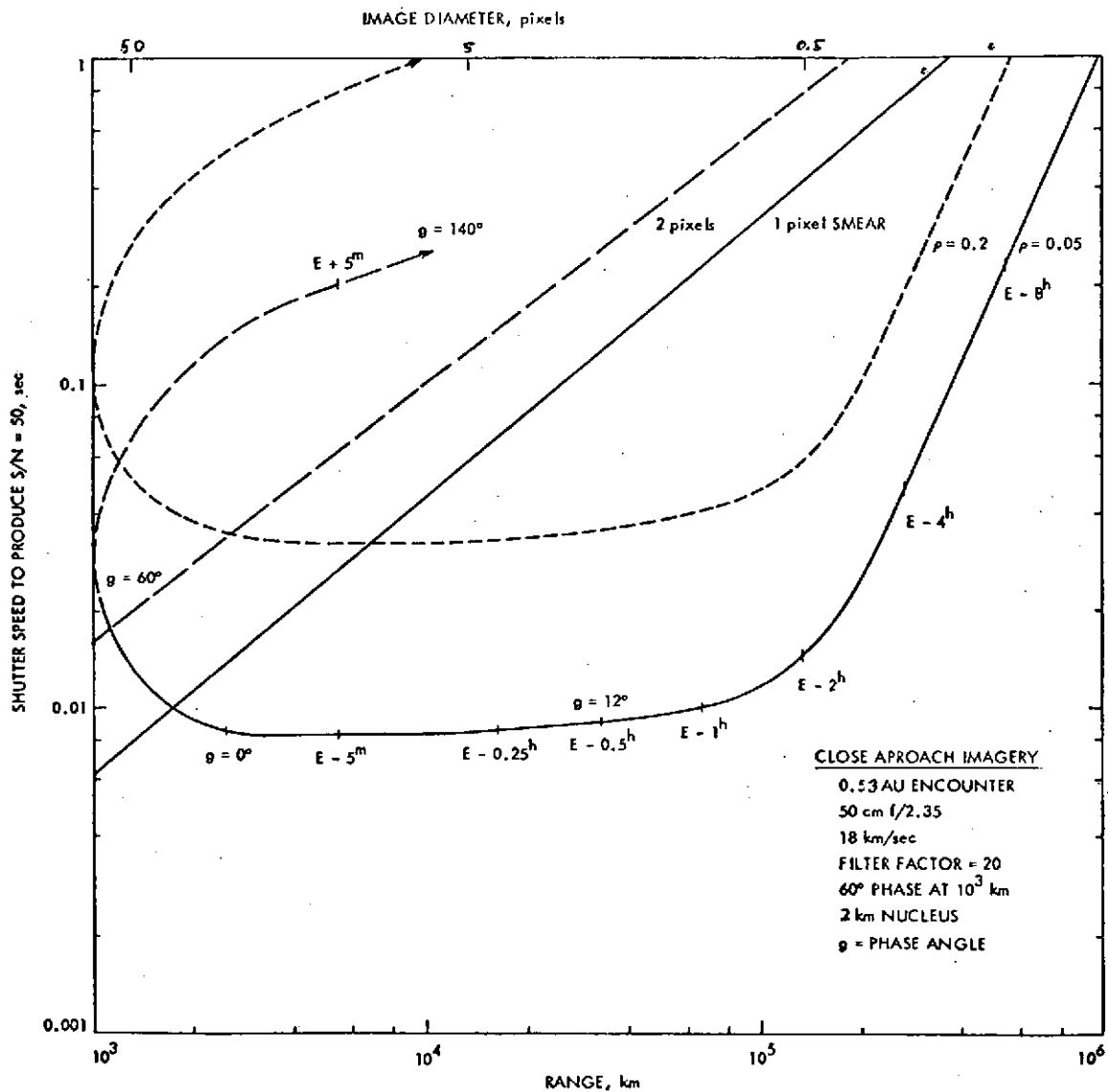
Figure IV-7. This figure illustrates the required shutter speed to obtain an image of the Encke nucleus at S/N = 50. The image S/N dependent on the nucleus brightness which is a function of albedo (0.05 vs. 0.2), phase geometry, and distance if the image is a point source ($>10^5$ km range). Following the approaching nucleus from right to left, it is apparent that the required shutter speeds yield less than one pixel of image smear (clear filter) unless narrow bandpass filters are used (Filter Factor = 20).
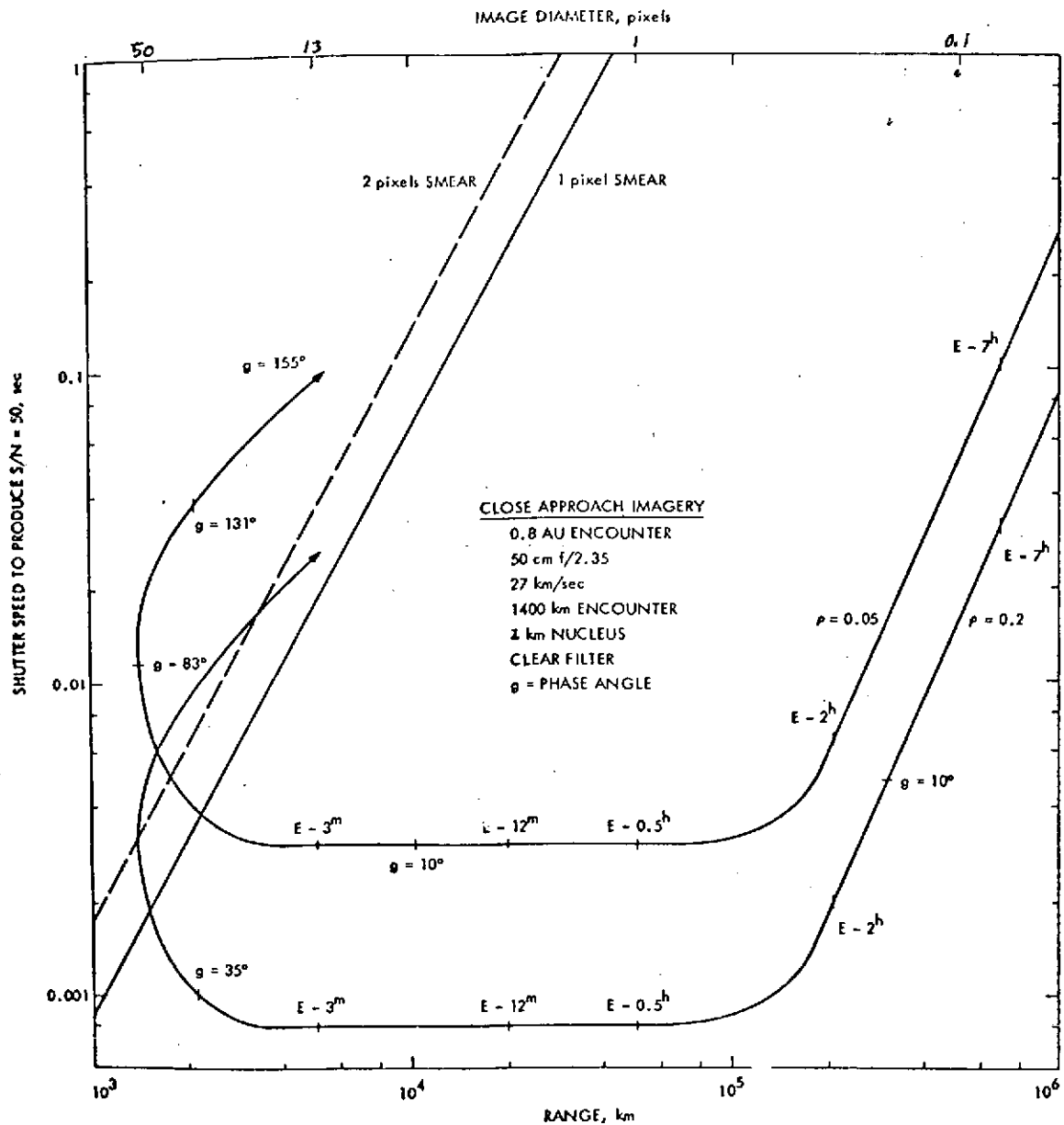
Figure IV-8. This figure illustrates the required shutter speed to obtain an image of the Encke nucleus at S/N = 50. The image S/N is dependent on the nucleus brightness which is a function of albedo (0.05 vs. 0.2), phase geometry, and distance if the image is a point source ($>10^5$ km range). Following the approaching nucleus from right to left, it is apparent that the required shutter speeds yield less than one pixel of image smear (clear filter) unless narrow bandpass filters are used (Filter Factor = 20).